UNIVERSITY OF ANTWERP
FACULTY OF SCIENCE
DEPARTMENT OF PHYSICS
2024-2025

University of Antwerp
Particle Physics Group

# BACKGROUND SENSITIVITY STUDIES OF REVERSED LVDT'S AND THEIR POTENTIAL SHIELDING OPTIONS

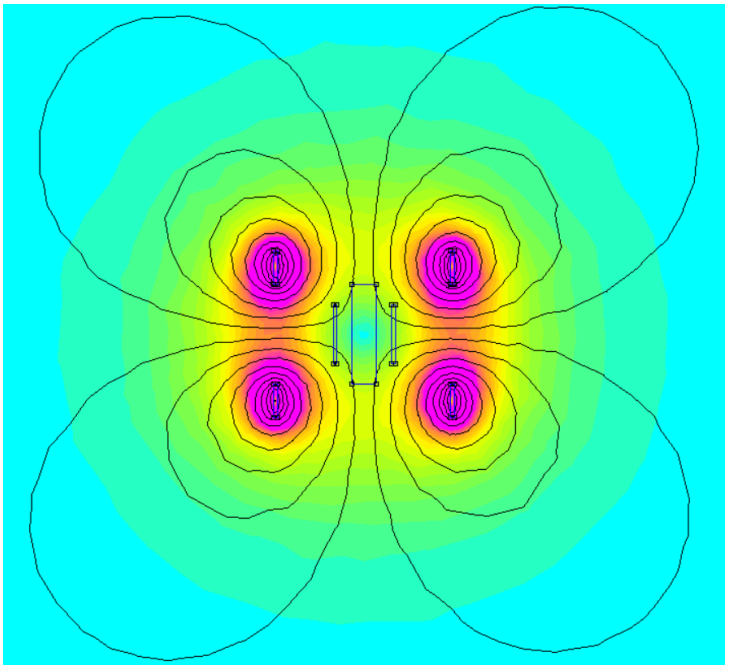

**JONAS JACOBS**

MASTER'S THESIS
**MASTER OF SCIENCE IN PHYSICS**

SUPERVISOR:
**PROF. DR. HANS VAN HAEVERMAET**

COSUPERVISORS:
**KUMAR AKHIL KUKKADAPU**
**PENGBO LI**

*A thesis submitted in fulfillment of the requirements for the degree Master of Physics*

# Contents

# English Abstract

## Background Sensitivity Studies of Reversed LVDT's and their Potential Shielding Options

Jonas Jacobs

Gravitational wave detection has revolutionized physics allowing us to observe cosmic phenomena previously hidden from electromagnetic observation. Unfortunately, current detectors are only capable of detecting the most intense gravitational waves, and will therefore only give information about a limited number of sources. Consequently, there was a need for a new, more sensitive detector, able to detect faint signals over a broad spectrum. Such a detector would give a possibility of discovering things such as dark matter or sensing gravitational waves from the early universe, moments after the Big Bang. The new detector is called the Einstein Telescope and its construction is expected to start in 2028.
An important part to increase the sensitivity of these measurements is displacement sensors such as a Linear Variable Differential Transducer (LVDT). LVDT's are used to monitor and control the position of the mirrors in interferometric gravitational wave detectors. However, since the Einstein Telescope will push the limits of sensitivity, the influence of electromagnetic interference might become a limiting factor in the performance of suspensions.
This thesis investigates the use of a reversed LVDT (RLVDT), a new idea that has not yet been used in reality, with primary focus on electromagnetic shielding strategies to reduce noise and interference. Using both finite element method simulations and an experimental setup, the performance of various shielding materials and geometries is studied in both AC and DC magnetic environments. An analysis of shielding effects on sensitivity and linearity is performed, identifying trade-offs between field suppression and sensor performance.
Additionally, this work briefly explores the influence of excitation frequency on the sensitivity, and evaluates the dynamic behavior of the RLVDT configuration.
The insights gained in this thesis can be used in prototypes such as ETpathfinder, and more broadly contribute to the refinement of displacement-sensor usage in future gravitational wave observatories. Additionally, it can be used in designing more compact and smaller suspensions that can be used on optical benches. Here, the sensors will be very close to each other.

# Dutch Abstract

## Background Sensitivity Studies of Reversed LVDT's and their Potential Shielding Options

Jonas Jacobs

De detectie van zwaartekrachtsgolven heeft de fysica gerevolutionaliseerd. Het stelt ons in staat om kosmische verschijnselen waar te nemen die onzichtbaar zijn voor elektromagnetische sensoren. De huidige detectoren meten enkel de meest intense golven, waardoor we slechts een beperkt aantal bronnen kunnen bestuderen. Daarom is er een nieuwe, gevoeligere detector nodig: de Einstein Telescope. Die moet zwakke signalen kunnen registreren over een breed spectrum. Er wordt verwacht dat deze mogelijks donkere materie zou kunnen identificeren of golven waar te nemen uit het vroege universum, vlak na de oerknal.
Om dit te bereiken, zijn verplaatsingssensoren zoals LVDT's (Linear Variable Differential Transducers) onmisbaar. Deze meten en controleren de positie van, onder andere, de spiegels in de detectoren met hoge precisie. Omdat de Einstein Telescope extreem gevoelig wordt, kan zelfs de kleinste elektromagnetische storing de metingen beïnvloeden en zijn er dus manieren nodig om dit te onderdrukken.

In dit onderzoek staat het gebruik van een *reversed LVDT* (RLVDT) centraal, hoofdzakelijk elektromagnetische afscherming, die de RLVDT moet beschermen tegen ruis en interferentie. De RLVDT is een nieuw idee en is in de realiteit nog niet gebruikt. Via computersimulaties (*finite element methods*) en experimenten worden verschillende afschermmaterialen en vormen getest, zowel in AC als DC magnetische velden. Hierbij wordt niet alleen bestudeerd naar hoe goed de ruis onderdrukt wordt, maar ook of dit ten koste gaat van de meetnauwkeurigheid of lineariteit van de sensor.
Ook onderzochten we kort hoe de gevoeligheid van de RLVDT verandert bij verschillende excitatiefrequenties, en of er een dynamische respons is.
De verkregen inzichten zijn direct bruikbaar voor projecten zoals ETpathfinder (een testopstelling voor de Einstein Telescope) en kunnen helpen om verplaatsingssensoren in toekomstige zwaartekrachtsgolfdetectoren nog verder te optimaliseren. De RLVDT zou ook gebruikt kunnen worden in het ontwerpen van kleinere ophangsystemen die gebruikt kunnen worden op optische tafels, waar de sensoren heel dicht bij elkaar staan.

# Acknowledgements

I'd first like to mention how grateful I am to have had Professor Hans Van Haevermaet as my supervisor. With his continuous support and availability throughout this whole project he really showed how valuable it is to have a good supervisor. Solving problems and thinking about implications of data together have helped me to bring my understanding of the subject to a whole new level. In extention of this I'd like to thank Pengbo Li and Kumar Akhil Kukkadapu for, not only, the guidance and help with the software and experimental setup, but also with the insights, discussions and availability they have blessed me with.
Another note of thanks to the whole Particle Physics Group of the university of Antwerp for the welcoming feeling they have given me during lunch breaks. It makes me feel sad to say goodbye to all of them.
To finish the acknowledgements, I'd like to thank my friend Wannes De Vleeschouwer for lending me his LEGO®, without his contribution, the experimental set-up could not have been realised.

# 1 Introduction

> **"If I were wrong, one would have been enough."**
> ***Albert Einstein***

In 1915, Albert Einstein, a name known by all, published General Relativity. A theory that came unexpected and shocked the entire scientific community, a theory the world was not ready for, a theory that got a tsunami of criticism. Hundreds of experiments were designed to disprove the theory, but every time, instead of disproving, they gave evidence that said theory was correct, strengthening it over and over again. Nevertheless more experiments were designed and more criticism was given. This all lead to his expression "If I were wrong, one would have been enough." [62]

## 1.1 Classical Gravity vs General Relativity

In 1687, Isaac Newton published a book called *Philosophiæ Naturalis Principia Mathematica*, which is Latin for *Mathematical Principles of Natural Philosophy*. In this book, he described the law of universal gravitation. This law states that there is an attractive force between massive objects, proportional to the product of their masses and inversely proportional to the distance between them squared:

$$F \propto \frac{m_1 m_2}{r^2} \tag{1.1}$$

Here $F$ stands for the gravitational force, $m_1$ and $m_2$ for the masses of the objects and $r$ for the distance [58]. The proportionality constant, within 1%, was found in 1798 to be $G = 6.6743 \times 10^{-11} \frac{m^3}{kg \cdot s^2}$ by Henry Cavendish [47]. Newton's law of universal gravitation treats gravity as an instantaneous force. This formulation was a good approximation that explained many phenomena: planetary movements, falling apples and the tides of the sea. However, some phenomena could not be explained using Newtonian gravity [58]. The precession of Mercury's orbit is one example. Mercury's precession refers to the rotation of its elliptical orbit over time, which precesses slightly more than Newtonian physics predicts. This is because of the intense gravitational field near the Sun [46].
General relativity (GR) does not define gravity as a force but as a manifestation of curvature of spacetime caused by mass and energy. It assumes that the universe is a spacetime continuum. Thus, what in our daily life is perceived as a three-dimensional space and a one-dimensional time, are not two distinct spaces but rather one four-dimensional concept called spacetime. The Einstein field equation links curvature of spacetime to the energy-momentum tensor $T_{\mu\nu}$.

$$R_{\mu\nu} - \frac{1}{2} R g_{\mu\nu} = 8\pi G T_{\mu\nu}. \tag{1.2}$$

Here, $R_{\mu\nu}$ is the Ricci curvature tensor, $R$ is the Ricci scalar and $g_{\mu\nu}$ is the metric tensor, which will be discussed later.
It is important to know that the curvature of spacetime, which humans see as a gravitational force, is a consequence of energy and momentum, and thus also the mass of an object. A heavy body will curve the spacetime continuum more than a light body. This is visualized in Figure 1.1 [10].

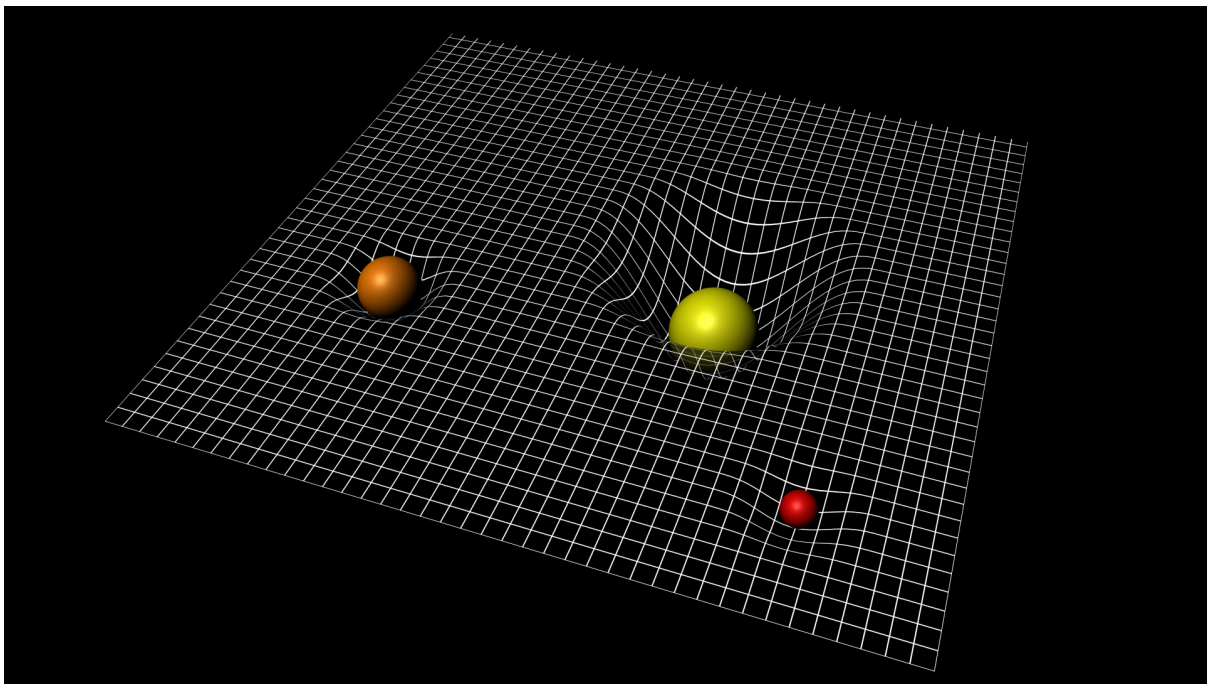

Figure 1.1: Artistic representation of massive bodies and their respective curvature of spacetime [33]

This new theory describes Mercury's orbit precession with higher accuracy [46]. It also brings forth some interesting phenomena like the bending of light, black holes and gravitational waves. Since photons are massless, there is no attractive force between light and a massive body, according to Newtonian gravity. In GR, photons follow the curvature of spacetime. A straight lightbeam will therefore be deflected in the presence of massive objects. The formula for deflection angle is given by

$$\theta = \frac{4GM}{c^2 r} \tag{1.3}$$

Where $G$ is the gravitational constant, $M$ the mass of the massive body, $c$ the speed of light and $r$ the normal distance from the light to the massive object. As one can see, the closer the lightbeam to the body, the more deflection it has. This is opposite to an optical lens, that has the maximum deflection far away from the center. This effect was first observed on the $29^{\text{th}}$ of May 1919 during a total solar eclipse. A change in the position of stars was seen as their light passed near the Sun, giving the first experimental confirmation of the prediction of light bending [51, 10]. Figure 1.2 shows a schematic representation of bended light due to the Sun's large mass.

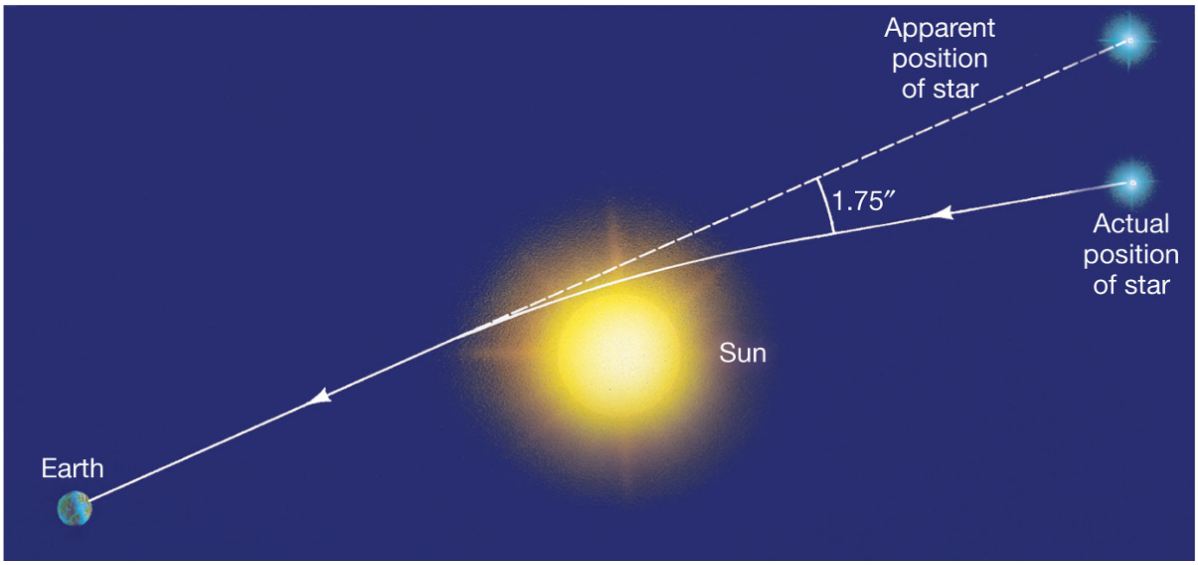


Figure 1.2: Schematic representation of gravitational light deflection [36]

There are objects that are so heavy that it results in a singularity, a hole of infinite deepness, in the spacetime continuum, visualized in Figure 1.3. These objects are called black holes. They are so heavy that even light can not escape the singularity they create [10]. Important is to note that the illustrations make it seem that spacetime is twodimensional while in fact it is fourdimensional, something the human mind can not visualize.

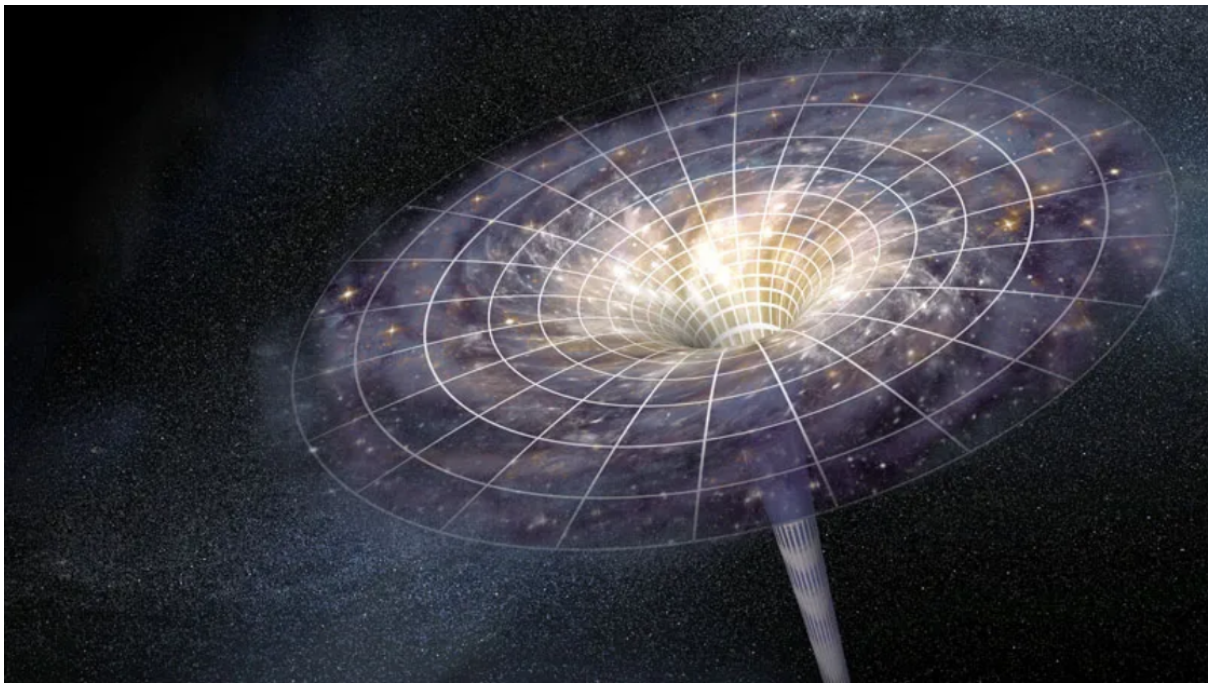

Figure 1.3: Artistic representation of a black hole [11]

In 1916 Einstein showed that gravitational waves are also a direct consequence of GR. They are ripples in the spacetime continuum, propagating at the speed of light. Any accelerating mass that is not spherically symmetric generates these waves, comparable with a moving electric charge that produces electromagnetic radiation. However, due to the weak nature of gravity, (currently) detectable gravita-

tional waves only arise from the most extreme cosmic events, where massive objects undergo violent acceleration, like colliding black holes, neutron stars or supernova's [50, 53].

## 1.2 Gravitational Waves

### 1.2.1 The Wave Equation

In this section we will use the field equation to mathematically "find" the gravitational waves [10, 41]. As written above, the Einstein field equation is given by:

$$R_{\mu\nu} - \frac{1}{2}Rg_{\mu\nu} = 8\pi G T_{\mu\nu}. \tag{1.4}$$

Where $R_{\mu\nu}$ is the Ricci Tensor, a tensor that describes curvature, $R = R^{\mu}{}_{\mu}$ the Ricci Scalar, $g_{\mu\nu}$ is the metric tensor, $G = 6.673 \times 10^{-11} m^3 kg^{-1} s^{-2}$ is Newton's gravitational constant and $T_{\mu\nu}$ is the energy-momentum tensor. The metric tensor is probably the most important part of general relativity. It quantifies the geometry of spacetime. For flat spacetime, where the spacetime geometry doesn't matter, we use the Minkowski metric $\eta_{\mu\nu} = \text{diag}(-1,1,1,1)$. If we describe gravity as weak, we typically choose the metric to be a perturbed Minkowski metric $g_{\mu\nu} = \eta_{\mu\nu} + h_{\mu\nu}$. This gives a linearized version of GR. It describes a small symmetric tensor field $h$ that propagates on the flat 'background' spacetime. The assumption that $h_{\mu\nu}$ is small allows us to ignore higher order terms of this quantity. We will now try to find the equations of motion obeyed by the perturbations $h_{\mu\nu}$, these come from examining the Einstein equation. We start with the Christoffel symbols:

$$\Gamma^{\rho}_{\mu\nu} = \frac{1}{2}g^{\rho\lambda}(\partial_\mu g_{\nu\lambda} + \partial_\nu g_{\lambda\mu} - \partial_\lambda g_{\mu\nu}) \tag{1.5}$$

$$= \frac{1}{2}\eta^{\rho\lambda}(\partial_\mu h_{\nu\lambda} + \partial_\nu h_{\lambda\mu} - \partial_\lambda h_{\mu\nu}) \tag{1.6}$$

Because $h_{\mu\nu}$ is small we can, when constructing the Riemann tensor, ignore the $\Gamma^2$ terms.

$$R_{\mu\nu\rho\sigma} = \eta_{\mu\lambda}\partial_\rho\Gamma^{\lambda}_{\nu\sigma} - \eta_{\mu\lambda}\partial_\sigma\Gamma^{\lambda}_{\nu\rho} + \mathcal{O}(\Gamma^2) \tag{1.7}$$

$$= \frac{1}{2}(\partial_\rho\partial_\nu h_{\mu\sigma} + \partial_\sigma\partial_\mu h_{\nu\rho} - \partial_\sigma\partial_\nu h_{\mu\rho} - \partial_\rho\partial_\mu h_{\nu\sigma}) \tag{1.8}$$

From which we get the Ricci tensor by contracting over $\mu$ and $\rho$

$$R_{\mu\nu} = \frac{1}{2}(\partial_\sigma\partial_\nu h^{\sigma}{}_{\mu} + \partial_\sigma\partial_\mu h^{\sigma}{}_{\nu} - \partial_\mu\partial_\nu h - \Box h_{\mu\nu}) \tag{1.9}$$

Where $\Box = -\partial_t^2 + \partial_x^2 + \partial_y^2 + \partial_z^2$ is the d'Alembertian in flat spacetime. Taking the trace of the Ricci Tensor gives us the Ricci Scalar

$$R = \eta^{\mu\nu}R_{\mu\nu} = \partial_\mu\partial_\nu h^{\mu\nu} - \Box h. \tag{1.10}$$

The Einstein Tensor $G_{\mu\nu} = R_{\mu\nu} - \frac{1}{2}R\eta_{\mu\nu}$ then becomes:

$$G_{\mu\nu} = \frac{1}{2}(\partial_\sigma\partial_\nu h^{\sigma}{}_{\mu} + \partial_\sigma\partial_\mu h^{\sigma}{}_{\nu} - \partial_\mu\partial_\nu h - \Box h_{\mu\nu} - \eta_{\mu\nu}\partial_\rho\partial_\lambda h^{\rho\lambda} + \eta_{\mu\nu}\Box h) \tag{1.11}$$

Now we have the linearized Einstein Equation $G_{\mu\nu} = 8\pi G T^{(0)}_{\mu\nu}$. Here, $T^{(0)}_{\mu\nu}$, is the energy-momentum tensor calculated in first order. However, the decomposition of the metric into the Minkowski metric

and a perturbation is not uniquely defined. This requires that a gauge needs to be fixed. The gauge transformation of the perturbation metric after infinitesimal coordinate transformation $\xi_\mu$ is given by:

$$h'_{\mu\nu} = h_{\mu\nu} + 2\partial_{(\mu}\xi_{\nu)} \tag{1.12}$$

Where the subscript $(\mu\ \nu)$ means symmetric under change of indices. We define a trace-reversed perturbation $\bar{h}_{\mu\nu} = h_{\mu\nu} - \frac{1}{2}\eta_{\mu\nu}h$. Not shockingly, if we take the trace we get $\bar{h} = -h$, the trace is reversed. If we choose a Lorenz gauge ($\partial_\mu \bar{h}^{\mu\nu} = 0$), the Einstein Tensor for the trace-reversed perturbation has the following form

$$G_{\mu\nu} = -\frac{\Box\bar{h}_{\mu\nu}}{2} \tag{1.13}$$

And thus the Einstein equation:

$$\Box\bar{h}_{\mu\nu} = -16\pi G T_{\mu\nu} \tag{1.14}$$

This equation is the base equation to study the gravitational waves. Consider a vacuum (so $T_{\mu\nu} = 0$) the equation becomes

$$\Box\bar{h}_{\mu\nu} = 0 \tag{1.15}$$

This is a wave equation! It describes the interaction of the gravitational waves with test-particles. Outside of the vacuum, the right hand side does not vanish. We can choose another gauge to further simplify the problem. In the Transverse Traceless gauge we get:

$$\bar{h}^{0\mu} = 0, \qquad \bar{h}^i_{\ i} = 0, \qquad \partial_i \bar{h}^{ij} = 0 \tag{1.16}$$

Then we can solve Equation 1.15 to get a plane wave solution:

$$h^{TT}_{\mu\nu} = C_{\mu\nu} e^{ik_\sigma x^\sigma} \tag{1.17}$$

Where $k_\sigma$ is the wave vector and $C_{\mu\nu}$ a constant symmetric $(0,2)$-tensor with $C_{\nu 0} = C^\nu_{\ \nu} = 0$. This is a correct solution if $k_\sigma$ has the right normalization:

$$\Box h^{TT}_{\mu\nu} = \eta^{\rho\sigma}\partial_\rho\partial_\sigma h^{TT}_{\mu\nu} = -\eta^{\rho\sigma}k_\rho k_\sigma h^{TT}_{\mu\nu} = -k^\sigma k_\sigma h^{TT}_{\mu\nu} \tag{1.18}$$

Since this has to be equal to 0 we get the normalization condition $k^\sigma k_\sigma = 0$. This is the property of a lightlike wave and therefore we conclude that gravitational waves travel at lightspeed! Using the Lorenz gauge:

$$\partial_\mu h^{\mu\nu}_{TT} = 0 = iC^{\mu\nu}k_\mu e^{ik_\sigma x^\sigma} \Rightarrow C^{\mu\nu}k_\mu = 0 \tag{1.19}$$

and that tells us that $C^{\mu\nu}$ and $k_\mu$ are perpendicular so that a wave traveling in, let's say, the $x^3$ direction has a $C^{\mu\nu}$ tensor with components $C^{11}, C^{12}, C^{21}$ and $C^{22}$ and because of the tracelessness and symmetry, it only gives two independent components that we name $h_+$ and $h_\times$.

$$C_{\mu\nu} = \begin{pmatrix} 0 & 0 & 0 & 0 \\ 0 & h_+ & h_\times & 0 \\ 0 & h_\times & -h_+ & 0 \\ 0 & 0 & 0 & 0 \end{pmatrix} \tag{1.20}$$

To understand this tensor we will look what happens to the geodesics of test particles in the presence of a gravitational wave. The geodesic deviation equation is given by [10, 41]

$$A^\mu = \frac{D^2}{dt^2}S^\mu = R^\mu_{\ \nu\rho\sigma}T^\nu T^\rho S^\sigma \tag{1.21}$$

Where $A^\mu$ is the acceleration vector of a geodesic, $R^\mu_{\ \nu\rho\sigma}$ the Riemann curvature tensor, $T^\mu = \partial x^\mu/\partial t$ the tangent vector of the geodesic and $S^\mu = \partial x^\mu/\partial s$ the deviation vector of the geodesic (see Figure 1.4).

This equation is in the coordinate system that is locally inertial (freely falling) at the point of interest and $t$ is the coordinate's time. We clearly see that curvature influences the geodesics.

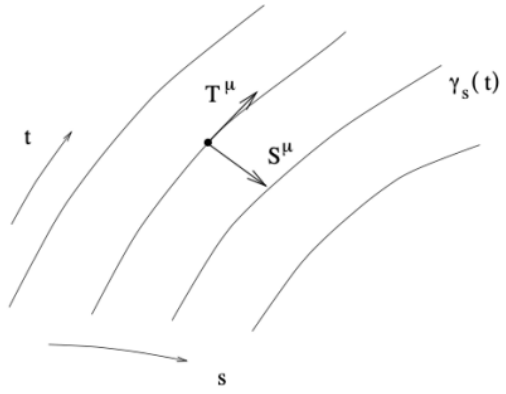


Figure 1.4: geodesics $\gamma$ with their tangent vector and deviation vector in a $(t,s)$-coordinate system [41]

In our case, this geodesic deviation equation becomes

$$\frac{\partial^2}{\partial t^2}S^\mu = \frac{1}{2}S^\sigma \frac{\partial^2}{\partial t^2}h^{TT\mu}{}_\sigma \tag{1.22}$$

Now we can look at the effects of $h_+$ and $h_\times$, but let's do this separately. When $h_\times = 0$ we get

$$\frac{\partial^2}{\partial t^2}S^1 = \frac{1}{2}S^1 \frac{\partial^2}{\partial t^2}h_+ e^{ik_\sigma x^\sigma} \Longrightarrow S^1 = (1+\frac{1}{2}h_+ e^{ik_\sigma x^\sigma})S^1(0) \tag{1.23}$$

$$-\frac{\partial^2}{\partial t^2}S^2 = \frac{1}{2}S^2 \frac{\partial^2}{\partial t^2}h_+ e^{ik_\sigma x^\sigma} \Longrightarrow S^2 = (1-\frac{1}{2}h_+ e^{ik_\sigma x^\sigma})S^2(0) \tag{1.24}$$

These equations show that the $x^1$-component will oscillate in the $x^1$-direction and the $x^2$-component will oscillate in the $x^2$-direction. The sign difference shows that when one coordinate has a positive deviation, the other one has a negative deviation. This results in a plus-like oscillation, hence the name $h_+$. A visual representation can be seen in Figure 1.5.
Following the same method, if $h_+ = 0$ we can see the effect of $h_\times$.

$$S^1 = S^1(0) + \frac{1}{2}h_+ e^{ik_\sigma x^\sigma} S^2(0) \tag{1.25}$$

$$S^2 = S^2(0) + \frac{1}{2}h_+ e^{ik_\sigma x^\sigma} S^1(0) \tag{1.26}$$

So, $x^1$-component oscillates in the $x^2$-direction and at the same time, the $x^2$-component oscillates in the $x^1$-direction. This results in a cross-like oscillation, hence the name $h_\times$. A visual representation is shown in Figure 1.5. Keep in mind that the wavevector in both situations is still in $x^3$-direction, so perpendicular to the geodesic deviation.

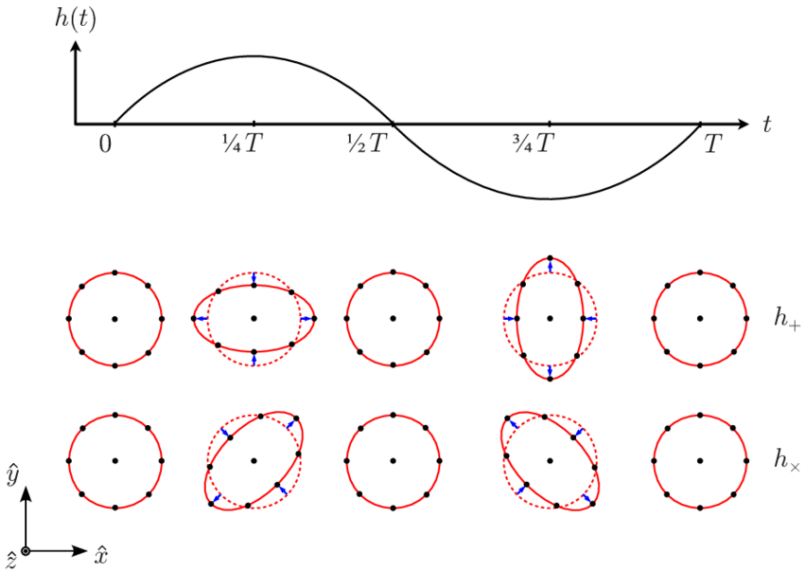


Figure 1.5: Visual representation of the plus- and cross-polarization of a gravitational wave traveling in the $z$-direction [37]

We thus see that a ring of free falling particles will become oscillating ellipses with a specific polarisation [10, 41].

### 1.2.2 Production of gravitational waves

What produces these waves? To answer this question, we need to take in account the energy-momentum tensor (Equation 1.15), but now $\Box\bar{h}_{\mu\nu} \neq 0$, so the choice of the Transverse Traceless gauge is not allowed and we need a more general formulation for $\bar{h}_{\mu\nu}$, acquired by using the Green function of the d'Alembertian $\Box_x \mathscr{G}(x^\sigma - y^\sigma = \delta^{(4)}(x^\sigma - y^\sigma)$, yielding the general solution to be: [10, 42]

$$\bar{h}_{\mu\nu}(x^\sigma) = -16\pi G \int \mathscr{G}(x^\sigma - y^\sigma) T_{\mu\nu}(y^\sigma) d^4y \tag{1.27}$$

Where the Green function for the forward propagated waves is given by the retarded solution

$$\mathscr{G}(x^\sigma - y^\sigma) = -\frac{1}{4\pi|\mathbf{x}-\mathbf{y}|}\delta(|\mathbf{x}-\mathbf{y}| - (x^0 - y^0))\Theta(x^0 - y^0) \tag{1.28}$$

With $\Theta(x)$ the Heaviside function and $|\mathbf{x}-\mathbf{y}|$ the norm of the spacial components of the fourvectors. Plugging this into Equation 1.27:

$$\bar{h}_{\mu\nu}(x^\sigma) = 4G \int d^4y - \frac{\delta(|\mathbf{x}-\mathbf{y}| - (x^0 - y^0))}{|\mathbf{x}-\mathbf{y}|}\Theta(x^0 - y^0) T_{\mu\nu}(y^\sigma) \tag{1.29}$$

$$= 4G \int \frac{d^3y}{|\mathbf{x}-\mathbf{y}|} \int d^0y \delta(y^0 - x^0 + |\mathbf{x}-\mathbf{y}|) T_{\mu\nu}(y^0, \mathbf{y}) \tag{1.30}$$

$$= 4G \int \frac{d^3y}{|\mathbf{x}-\mathbf{y}|} T_{\mu\nu}(x^0 - |\mathbf{x}-\mathbf{y}|, \mathbf{y}) \tag{1.31}$$

$$= 4G \int \frac{d^3y}{|\mathbf{x}-\mathbf{y}|} T_{\mu\nu}(t_r, \mathbf{y}) \tag{1.32}$$

Where $t_r = t - |\mathbf{x}-\mathbf{y}|$ is the retarded time.
We can now use a Fourier transformation (Equation 1.33)

$$f(t,\mathbf{x}) \to \tilde{f}(\omega,\mathbf{x}) = \frac{1}{\sqrt{2\pi}} \int dt e^{i\omega t} f(t,\mathbf{x}) \tag{1.33}$$

$$\tilde{f}(\omega,\mathbf{x}) \to f(t,\mathbf{x}) = \frac{1}{\sqrt{2\pi}} \int dt e^{-i\omega t} \tilde{f}(\omega,\mathbf{x}). \tag{1.34}$$

$$\tag{1.35}$$

to go to frequency space

$$\tilde{\bar{h}}_{\mu\nu}(\omega,\mathbf{x}) = 4G \int d^3 \frac{e^{i\omega|\mathbf{x}-\mathbf{y}|}}{|\mathbf{x}-\mathbf{y}|} \tilde{T}_{\mu\nu}(\omega,\mathbf{y}). \tag{1.36}$$

Consider a far isolated compact source, existing of non-relativistic matter, that is emitting gravitational waves. The approximation $|\mathbf{x}-\mathbf{y}| \approx r$ can be made such that

$$\tilde{\bar{h}}_{\mu\nu}(\omega,\mathbf{x}) = 4G \frac{e^{i\omega r}}{r} \int d^3 \tilde{T}_{\mu\nu}(\omega,\mathbf{y}) \tag{1.37}$$

Since we are in Fourier space, not all components have to be calculated.
Lorenz gauge implies $\partial_\mu \bar{h}^{\mu\nu}(t,\mathbf{x}) = 0 \to \tilde{\bar{h}}^{0\nu} = \frac{i}{\omega}\partial_i \tilde{\bar{h}}^{i\nu}$ so that only the spatial components have to be determined. Using partial integration and the fact that the source is isolated we have

$$\int d^3y \tilde{T}^{ij}(\omega,\mathbf{y}) = -\frac{\omega^2}{2} \int y^i y^j \tilde{T}^{00}(\omega,\mathbf{y}) d^3y = -\frac{\omega^2}{2} \tilde{I}_{ij}(\omega) \tag{1.38}$$

Where $I_{ij}$ is the quadrupole moment tensor of the energy density. Using the inverse Fourier transformation (Equation 1.34) we can go back to the time coordinate

$$\tilde{\bar{h}}_{ij}(\omega,\mathbf{x}) = -2G\omega^2 \frac{e^{i\omega r}}{r} \tilde{I}_{ij}(\omega) \to \bar{h}_{ij}(t,\mathbf{x}) = \frac{2G}{r} \frac{d^2}{dt^2} I_{ij}(t_r) \tag{1.39}$$

This is the quadrupole formula, describing the production of gravitational waves. The equation shows that gravitational waves produced by an isolated, non-relativistic, far object are proportional to the second derivative of the quadrupole moment of the energy density.
The current detectable gravitational waves are coming from the collision of black holes. This collision is the result of an inspiral movement. To understand better how this system emits gravitational waves we will look at the binary star system, represented in Figure 1.6.

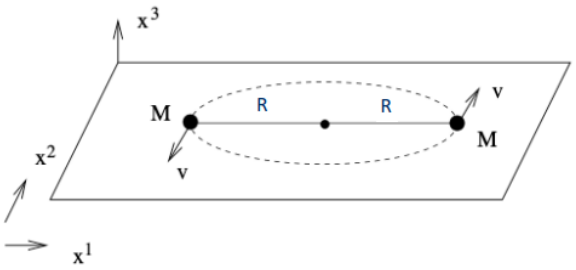


Figure 1.6: Schematic representation of a binary star system [9]

Consider two stars of mass $M$ in a circular orbit in the $x^1,x^2$-plane, at distance $R$ from the center of mass. We treat the motion of the stars in the Newtonian approximation to describe the circular track like Kepler. The circular orbit is most easily described by equating the attractive gravitational force (Newton's approximation) and the fictitious centrifugal force.

$$\frac{GM^2}{(2R)^2} = \frac{Mv^2}{R} \iff v = \left(\frac{GM}{4R}\right)^{1/2} \tag{1.40}$$

From this we can get the time it takes to complete one orbit (period $T$) and the angular frequency $\Omega$.

$$T = \frac{2\pi R}{v} \tag{1.41}$$

$$\Omega = \frac{2\pi}{T} = \left(\frac{GM}{4R^3}\right)^{1/2} \tag{1.42}$$

The explicit path for stars $a$ and $b$ is then given by

$$x^1_{a,b} = \pm R\cos\Omega t, \qquad x^2_{a,b} = \pm R\sin\Omega t \tag{1.43}$$

Where star $a$ gets the $+$ sign and star $b$ gets the $-$ sign.
The energy-momentum tensor can be approximated for a non-relativistic, compact, isolated system to be $T_{00} = T^{00} = \rho$ and the stars can be described as point particles such that

$$\rho(t,\mathbf{x}) = M\sum_{n=1}^{2}\delta(\mathbf{x}-\mathbf{x}_n(t)) \tag{1.44}$$

The energy-momentum tensor then becomes

$$T^{00}(t,\mathbf{x}) = M\delta(x^3)\left[\delta(x^1 - R\cos\Omega t)\delta(x^2 - R\sin\Omega t) + \delta(x^1 + R\cos\Omega t)\delta(x^2 + R\sin\Omega t)\right] \tag{1.45}$$

The delta functions allow us to easily integrate the energy-momentum tensor in order to get the quadrupole moment. The metric perturbation is then given by

$$\bar{h}_{ij}(t,\mathbf{x}) = \frac{8GM}{r}\Omega^2R^2\begin{pmatrix} -\cos 2\Omega t_r & -\sin 2\Omega t_r & 0 \\ -\sin 2\Omega t_r & \cos 2\Omega t_r & 0 \\ 0 & 0 & 0 \end{pmatrix} \tag{1.46}$$

Determining energy loss brings forth a lot of technical problems. One of them is that there is no universal way to define the energy of gravity in GR, where gravity is not seen as a force. In the weak field limit, where gravity is approximated by the symmetric tensor that propagates on a flat metric ($g_{\mu\nu} \approx \eta_{\mu\nu} + h_{\mu\nu}$) to take the derivative of the energy-momentum tensor for the metric perturbations $h_{\mu\nu}$. But to do this, we need to evaluate the Einstein equations to second order in $h$. After some calculations and assumptions, outside the scope of this thesis, we find the power $P$, related to the energy loss, for a binary star system to be

$$P = -\frac{2}{5}\frac{G^4M^5}{R^5} \tag{1.47}$$

When the stars start at a distance $R$ from the center of mass, they lose energy in the forms of gravitational waves. Due to conservation of energy, the radius $R$ decreases. Since angular frequency is inversely proportional to the radius, the amplitude and frequency of the gravitational waves increase, causing more energy loss. Because of this energy loss, the radius decreases further (Figure 1.7), and so on until they collide into each other [10, 42]. Figure 1.8 show an schematic representation of a binary star system emitting gravitational waves.

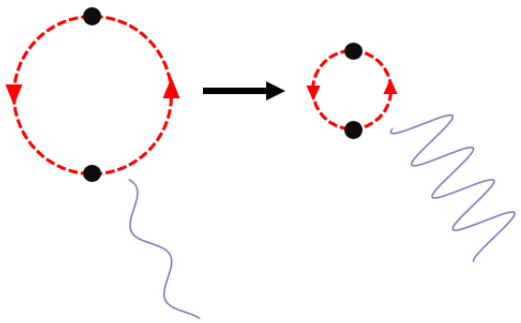

Figure 1.7: Schematic representation of decreasing distance due to energy loss by emitting gravitational waves of increasing amplitude and frequency [22].

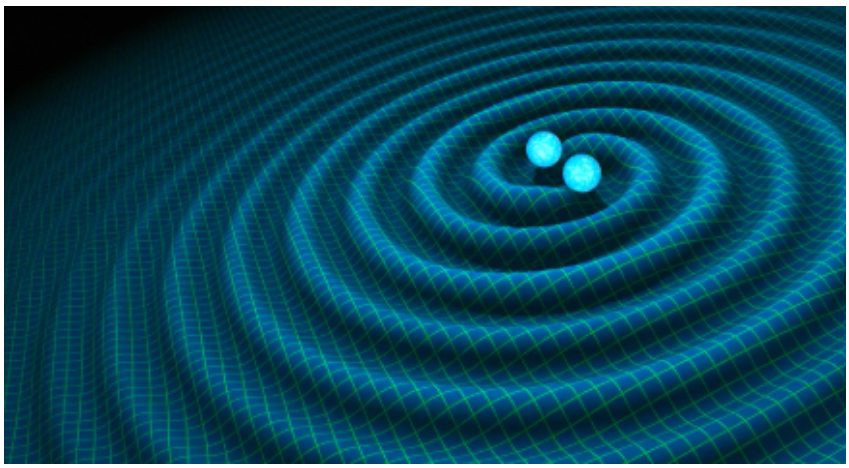

Figure 1.8: Artistic representation of two orbiting bodies emitting gravitational waves [63].

## 1.3 Detecting Gravitational Waves

Why are we interested in detecting gravitational waves?
Up until the first gravitational wave detector, the only way to study the universe was by using telescopes or other kind of detectors based on electromagnetic radiation or neutrino's. Gravitational waves have two unique properties. First, they are not based on electromagnetic radiation, making it possible to study "invisible" objects like black holes or dark matter. Second, gravitational waves can pass through any intervening matter without being scattered significantly. This means that they have astronomically large lifetimes. It also allows them to travel through planets, interstellar dust, etc. Light from distant stars may be blocked out by interstellar dust, for example, but gravitational waves will pass through it essentially unaffected.
These two features allow gravitational waves to carry information about astronomical phenomena that was never before observed by humans. The first direct detection of gravitational waves in 2015 by LIGO (a US-based gravitational wave detector), from a black hole merger 1.3 billion light-years away, confirmed Einstein's prediction and opened a new window to study the universe. Since then, dozens of mergers involving black holes and neutron stars have been observed, revealing extreme cosmic events invisible to traditional telescopes [53, 50, 52].
The Einstein Telescope, a next-generation gravitational wave detector, aims to detect lower-frequency waves and lower-amplitude waves from supermassive black holes, dark matter and possibly the earliest moments after the Big Bang. But there are many more sources that will be studied with this new detector.[63, 13]

But how to measure them? As shown in the theoretical derivation, gravitational waves deform spacetime by deviating the geodesics, these deformed geodesics are detectable because they are altering the position and distance between free-falling particles (Figure 1.5). An illustration of this deformation, induced by a plus-polarized gravitational wave, is shown in Figure 1.9.

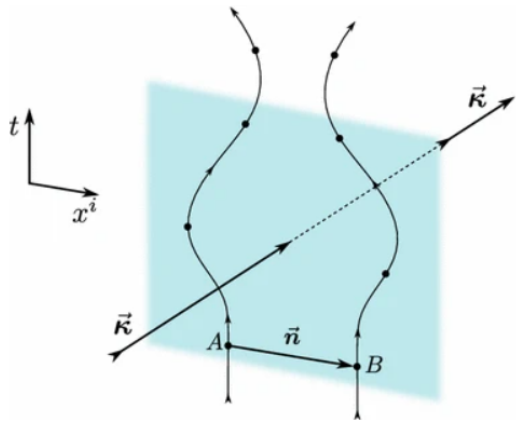


Figure 1.9: Schematic representation of geodesic deformation by a plus-polarized gravitational wave with wavevector $\vec{\kappa}$ [8]

Detecting gravitational waves is a difficult task due to their extremely small amplitudes, of the order of strain $h = \frac{\delta L}{L} \sim 10^{-21}$ (dimensionless units), meaning that they distort spacetime by one part in $10^{21}$. This is equivalent of changing the distance from the earth to the sun ($\approx 149.6 \cdot 10^{12}$ m) with less than the size of a carbon atom ($r_C \approx 3.4 \cdot 10^{-10}$ m). The gravitational wave that was detected in 2015 had a displacement of $\delta L \approx 10^{-18}$ m in the LIGO detector, this is more than a thousand times smaller than the diameter of a proton ($d_p \approx 1.7 \cdot 10^{-15}$ m) [4]. To detect such signals, highly sensitive instruments are an absolute requirement.

The design of a gravitational wave detector is based on the Michelson interferometer, represented in Figure 1.10(a). A laser beam is split into two perpendicular arms by a beam splitter, reflected off mirrors, and recombined to produce an interference pattern. Changes in the relative arm lengths, caused by spacetime distortions, lead to phase differences in the beams. When the beams are recombined the interference pattern will change according to the path length difference, based on the principle of constructive and destructive interference [23].
In the gravitational wave detectors, the arms are modified to be Fabry-Perot cavities. A Fabry-Perot cavity is an optical resonator formed by two parallel mirrors that trap and amplify light of specific wavelengths [13]. Figure 1.10(b) shows a schematic representation of a gravitational wave detector with the Fabry-Perot cavities.

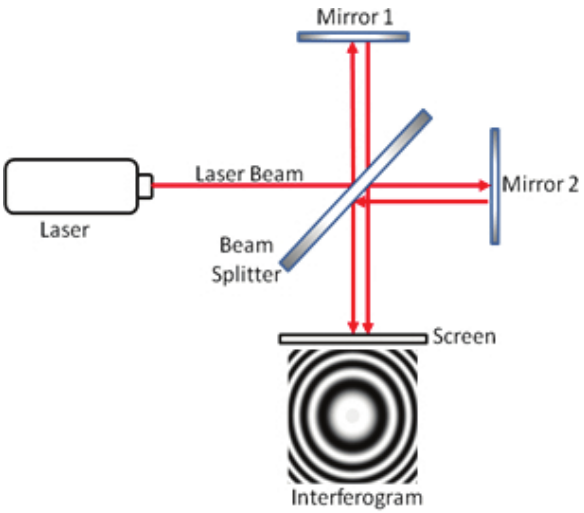


((a)) Schematic representation of a Michelson interferometer [23]

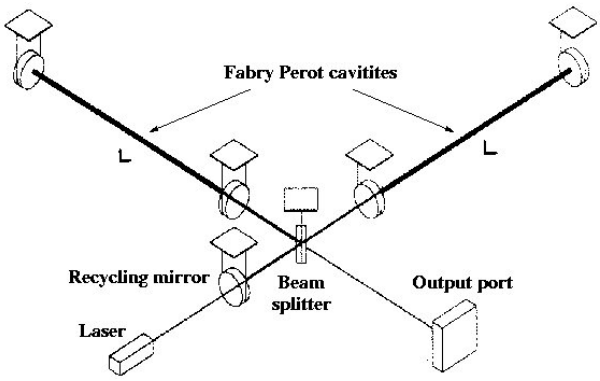


((b)) Schematic representation for a gravitational wave detector based on a Michelson interferometer with Fabry-Perot cavities in the arms [3]

If the mirrors are suspended as freely falling test masses, they follow the perturbed geodesics in the presence of a gravitational wave. Consequently, a passing wave induces a variation in the interference signal. Despite the high sensitivity of these detectors, current second generation gravitational wave detectors like LIGO (USA), Virgo (Italy) and KAGRA (Japan), can detect only the most intense gravitational waves, from the late inspiral and merger of colliding black holes and neutron stars [53, 54, 55, 60]. The amplitude and frequency right before the merger increase significantly, making the final moments the most detectable [10, 42].

Figure 1.11(a) presents simulated data of such a merger event, showing the evolution over time. Figure 1.11(b) highlights the dramatic increase in amplitude right before the merger. Figure 1.12 shows the real data of the first detected gravitational wave registered by the two LIGO detectors compared to the theoretically predicted values [4].

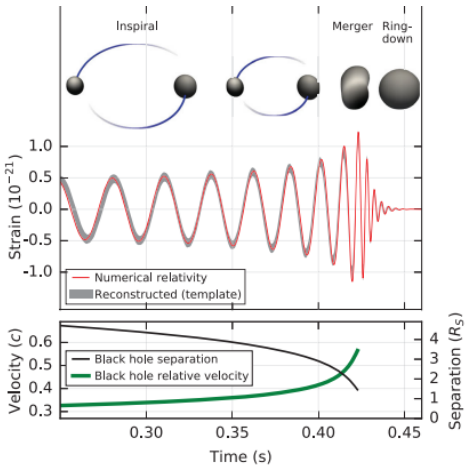


((a)) Top to bottom: representation of merging black holes, simulated gravitational wave signal, corresponding distance/velocity evolution [4]

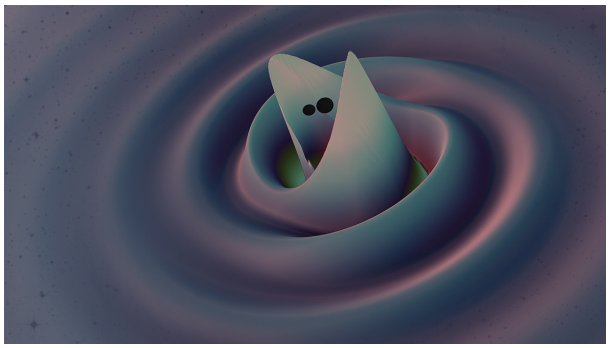

((b)) Amplitude increase of the gravitational wave signal approaching the moment of merger [30].

Figure 1.11: Simulation results illustrating gravitational wave signatures from a compact binary merger.

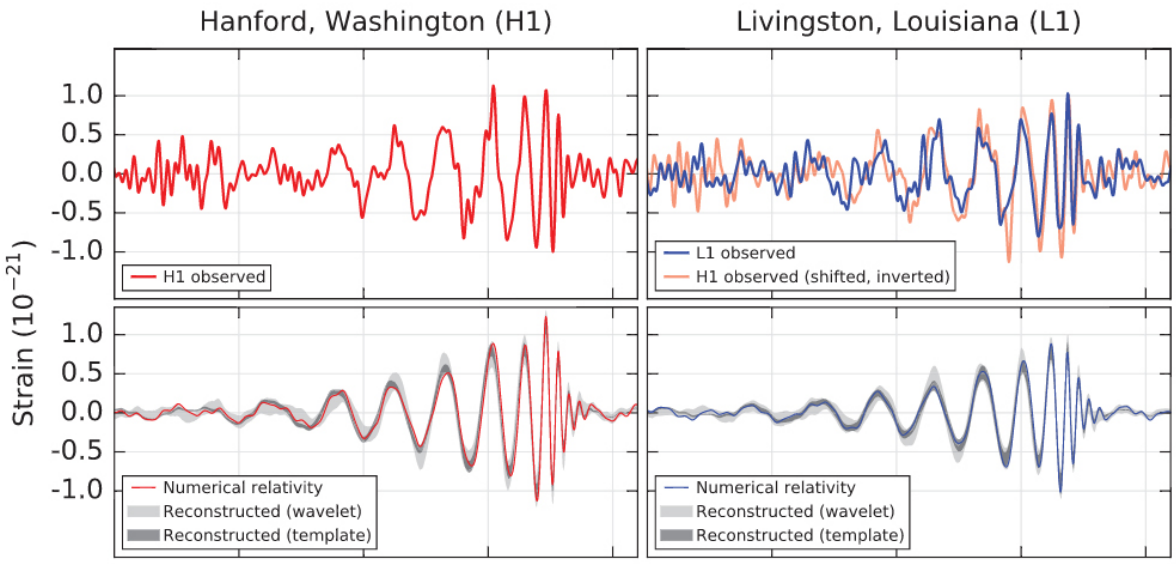


Figure 1.12: LIGO measurement of the first detected gravitational waves at the Livingston (right) and Hanford (left) detectors, compared with the theoretical predicted values [7]

## 1.4 Einstein Telescope and ETpathfinder

### 1.4.1 Einstein Telescope

The Einstein Telescope (ET) represents a third generation of gravitational wave detectors, designed to increase the sensitivity. The motivation for building ET lies in the limitations of current detectors. While LIGO revolutionized physics by making the first direct detections of gravitational waves, its sensitivity is constrained by noise such as thermal, seismic, and quantum noise. These limit the observations greatly, especially at lower frequencies (below $\sim$ 10 Hz). ET will extend the observable frequency band (down to 1 Hz) and improve the sensitivity by an order of magnitude, at low frequencies even multiple orders of magnitude. Figure 1.13 shows the predicted sensitivity of ET, compared to the current detectors, where it can be seen that ET will have an increased sensitivity and that it has the ability to detect low frequency waves [13, 14].

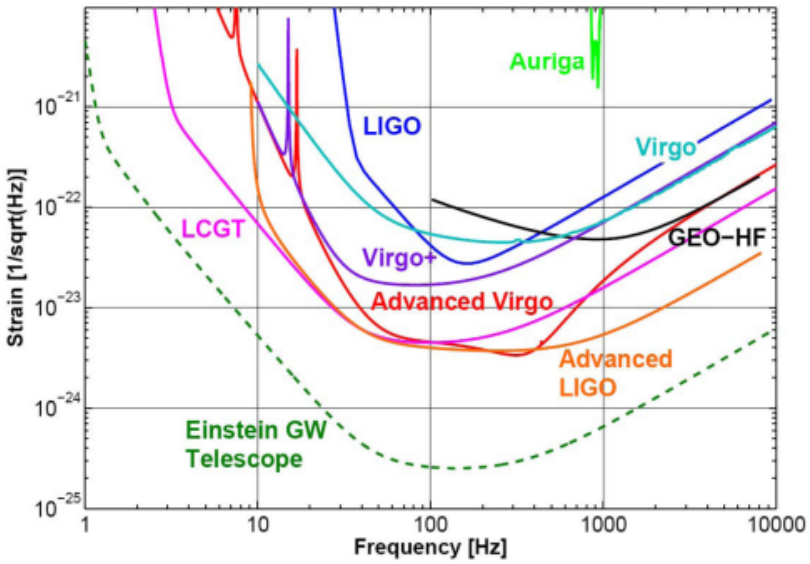


Figure 1.13: Sensitivities of the current detectors and the predicted sensitivity of the Einstein Telescope [13]

This will make it possible to observe way more and weaker events, such as the inspiral phase for hours or even days before merger. Moreover, it will allow us to detect intermediate-mass binary systems, study dark matter and gravitational waves from the early universe, all the way back to right after the big bang, and much more
The improvements are due to a new design, the existing detectors are L-shaped but ET will likely be shaped as a triangle with arms of 10 km. The corners will each have two interferometers, one with a low frequency laser and one with a high frequency laser (Figure 1.14) [13].

### Why a triangle?

Current detectors are L-shaped with equal arms, optimal for the nature of gravitational waves, as we have derived, gravitational waves are transverse quadrupole waves. When they get stretched in one direction, they get squeezed in the orthogonal direction. Resulting in a maximal response in the detectors. This response can be generally written as

$$h(t) = F_+(t)h_+(t) + F_\times(t)h_\times(t) = \sin\zeta\, f(t,\psi,...) \tag{1.48}$$

with $\zeta$ the opening angle of the interferometer arms, $F_+$ and $F_\times$ the beam pattern functions and $f(t,\psi,...)$ a function of the remaining parameters describing the geometry. For an equilateral triangle, the angle is $60^\circ$ such that the response is around 15% less. But a strong advantage of the triangular shape is that it can simultaneously measure both polarizations. Unlike a single L-shaped detector, which can only detect one linear polarization combination at a time, the triangular geometry provides complete polarization information continuously, essential for a more accurate source parameter estimation. Additionally, the triangular layout offers better redundancy, as the data from any two interferometer arms can reconstruct the third ($-h_{0^\circ} = h_{120^\circ} + h_{240^\circ}$) ensuring uninterrupted operation during maintenance or upgrades. This also allows us to create null-streams, a data analysis tool that helps isolate uncorrelated noise, increasing the detection confidence without the need of an additional detector [13].

### Sensitivity Improvement and Noise Reduction

To reach the sensitivity level that ET claims to get, the arms of the interferometer need to increase a lot. LIGO has 4 km arms and Virgo has 3 km arms. ET will need to have arms of 10 km to limit

the displacement noise to a tolerable level. The main noise sources that are limiting sensitivity are seismic, thermal, and quantum noise. Seismic noise, caused by ground vibrations from natural and human sources, is suppressed by building ET underground and using innovative suspension systems (see Section 1.4.3). Thermal noise, from thermal movements of atoms in mirrors and the suspension systems, is reduced by cooling parts of the detector to cryogenic temperatures. Quantum noise refers to limits coming from quantum mechanical effects like shot noise (uncertainty of the number of photons) and radiation pressure noise (momentum transfer from photons onto the mirrors). To tackle these problems across the full frequency range, each corner will have two interferometers: a low-frequency interferometer (1.5–30 Hz), operating at 10 K, and a high-frequency interferometer (30 Hz–10 kHz), at room temperature. This "xylophone" setup, combined with the use of squeezed light (non-classical light with correlations between its phase and amplitude), will help to optimize the sensitivity. Figure 1.15 shows an artistic representation of the Einstein Telescope [13].

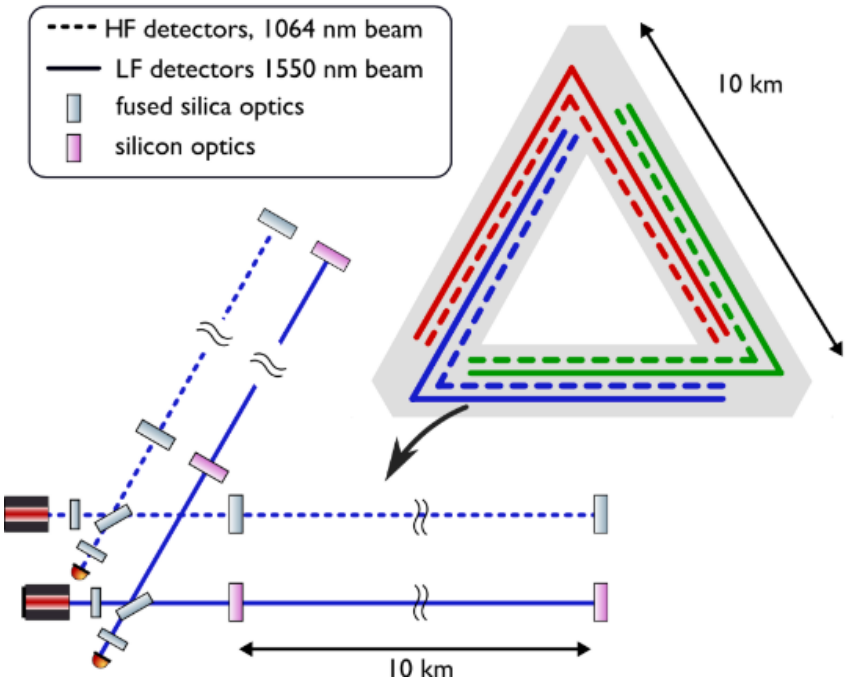


Figure 1.14: Schematic representation of ET [16]

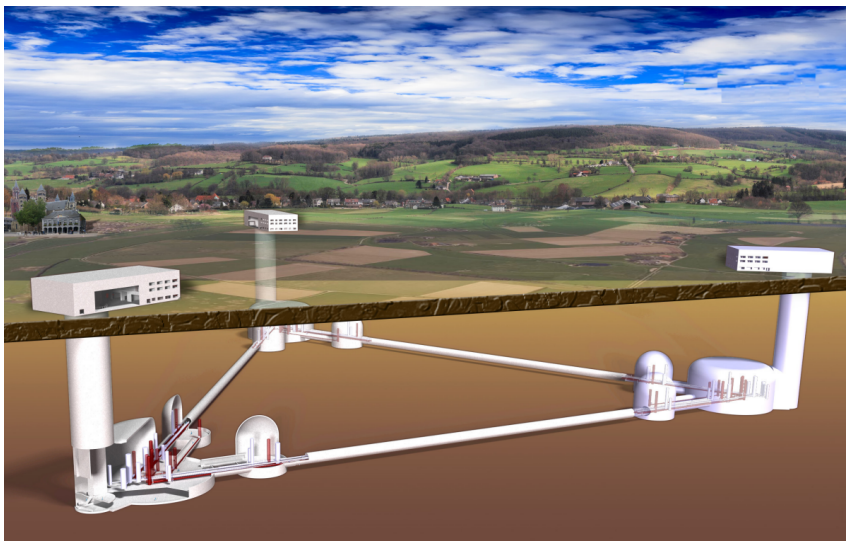

Figure 1.15: Artistic representation of ET [13]

### 1.4.2 ETpathfinder

In preparation of ET, an R&D prototype facility located in Maastricht with the name ETpathfinder, is currently under construction. ETpathfinder is not a gravitational wave detector itself, but a scaled prototype. This lab focuses on developing and testing the new technologies like, cryogenic cooling, seismic isolation and advanced optics for the ET's improved sensitivity and noise reduction. They are testing cryogenic mirrors, silicon mirrors (instead of quarts) and 1550 nm and 2090 nm optics. It is here that this work can be tested or used. Figure 1.17 shows a schematic representation and a layout of ETpathfinder and Figure 1.16 shows a picture of ETpathfinder in the cleanroom.[15]

Figure 1.16: Picture of ETpathfinder made in the cleanroom in Maastricht [17]

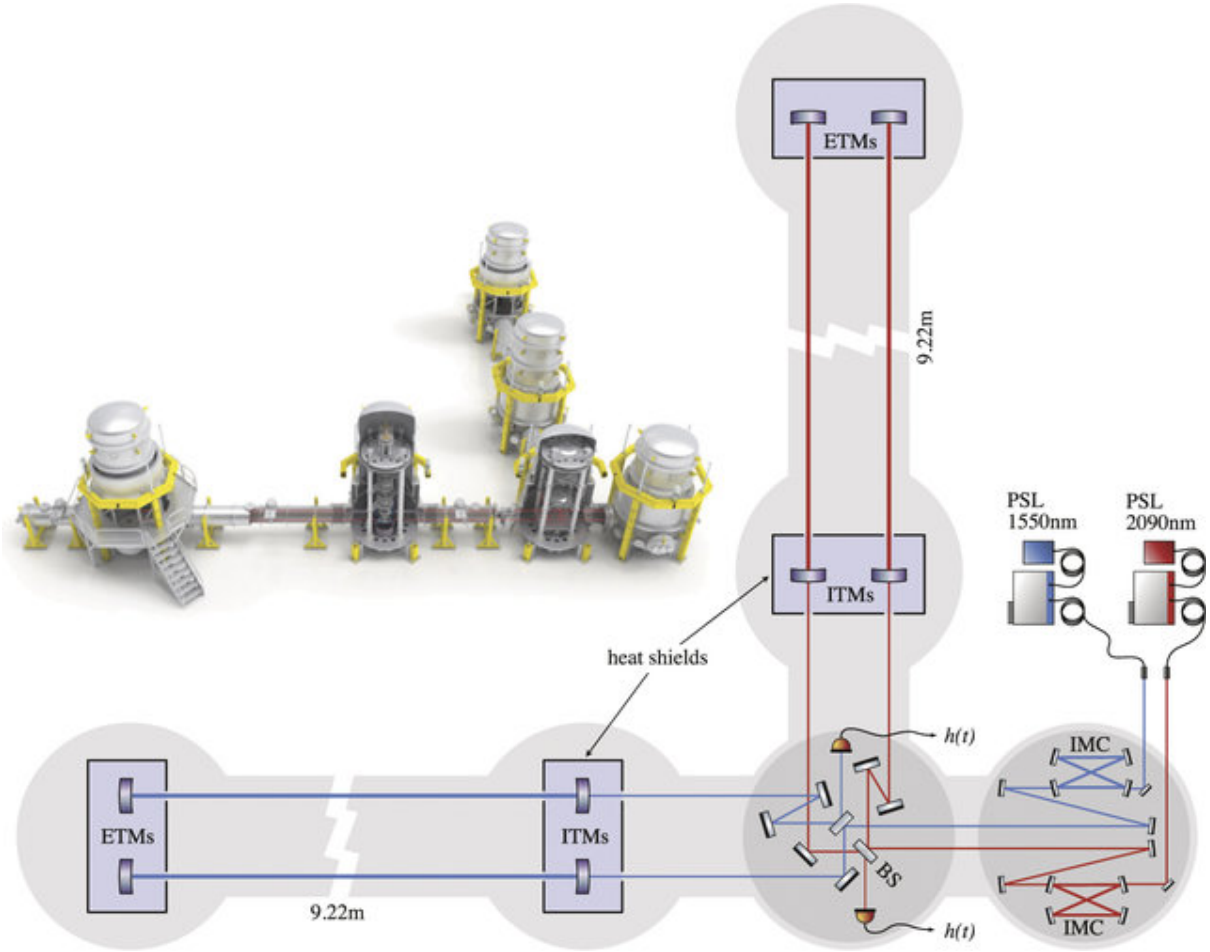


Figure 1.17: Artistic representation and schematic layout of ETpathfinder [2]

At Figure 1.17, one can see 4 mirror towers, labeled with 'ITM' (input test masses) and 'ETM' (end test masses). This is where the suspension systems for the mirrors will be implemented. The ITM and ETM together form the Fabry-Perot cavity, where the laserbeam will be reflected numerous times. The arm of the red laser (2090 nm) will be cooled to 10-15 K, the arm of the blue laser (1550 nm) will be cooled to 70 K. In reality, the lasers will not have these colors (they are both in the IR region), it is merely to give a clear distinction. The other two towers have the lasers, optical elements and sensor components placed on optical benches. The work that this thesis focuses on can be used in all 6 towers [15].

### 1.4.3 Suspension System

The suspension system in the towers incorporates a lot of techniques to reduce vibrations in all spatial directions. Additionally there are a lot of sensors to monitor any displacements with sub-micrometer accuracy. The suspension system mainly exists out of inverted pendulums (IP) and geometric anti-spring (GAS) filters, together with regular pendulums. GAS filters are designed to provide vertical isolation and inverted pendulums are crucial for horizontal isolation. In this isolation stack, inverted pendulums are placed at the top, followed by multiple GAS filters. Inside the mirror tower there is one large inverted pendulum with four legs, supporting a top shelf. On that shelf are two GAS-filters, each supported by a smaller IP with three legs. The mirror suspension starts with those two GAS-filters and going down there are three more per chain. This will all be at room temperature. The chain ends with the mirror in a cryogenic chamber, which resembles the regular pendulum. Figure 1.18 shows a

schematic representation of the part at room temperature, Figure 1.19 shows a schematic representation of the whole suspension system [15].

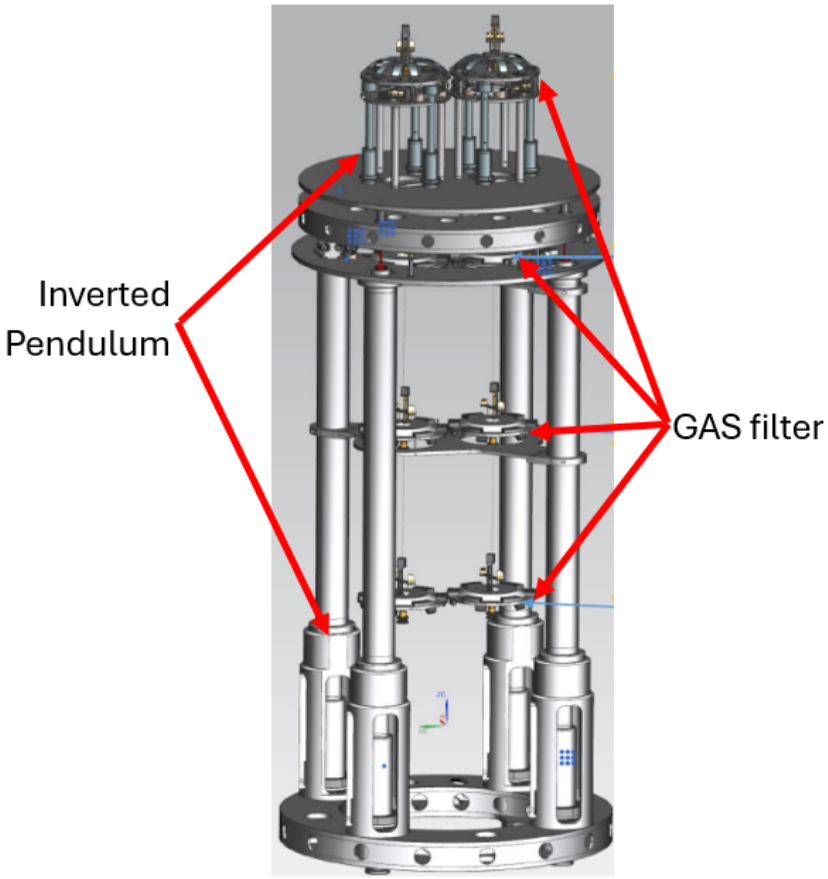


Figure 1.18: Schematic representation of the part of the suspension system in the mirror tower that is at room temperature [24].

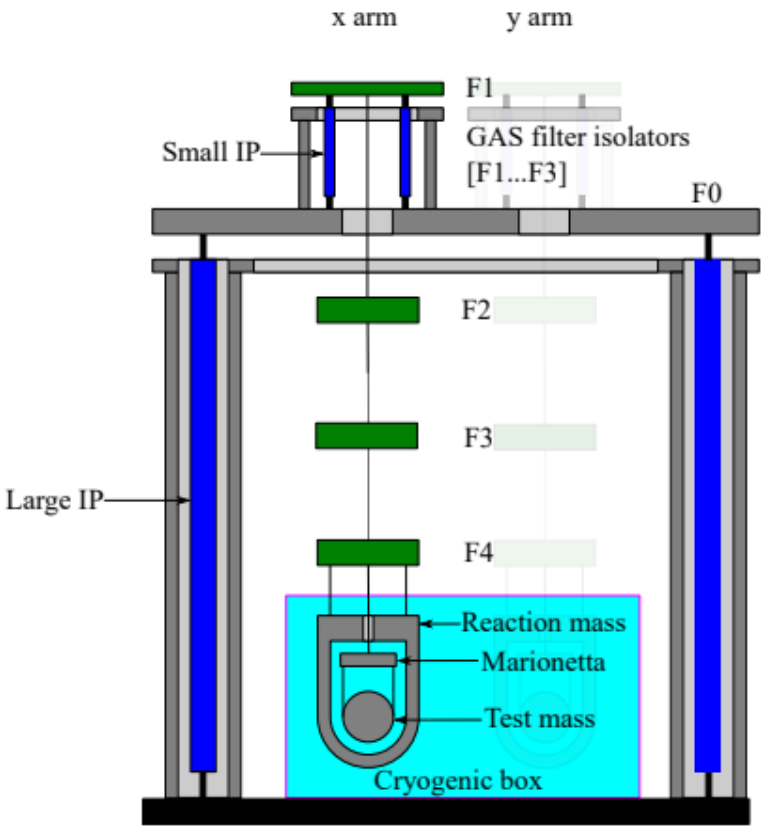


Figure 1.19: Schematic representation of the whole suspension system in the mirror tower [2]

A GAS filter consists of several cantilever blades that have inward compression. Under this compression, these blades bend slightly, introducing a geometric coupling between vertical and radial displacements. This coupling increases the system's effective vertical stiffness. Each GAS filter is equipped with an LVDT to sense the displacement. Figure 1.20 shows a GAS-filter and Figure 1.21 shows the LVDT at the GAS-filter. The reader might not recognize the LVDT yet, but later on I will refer back to this picture for an "aha-erlebnis".

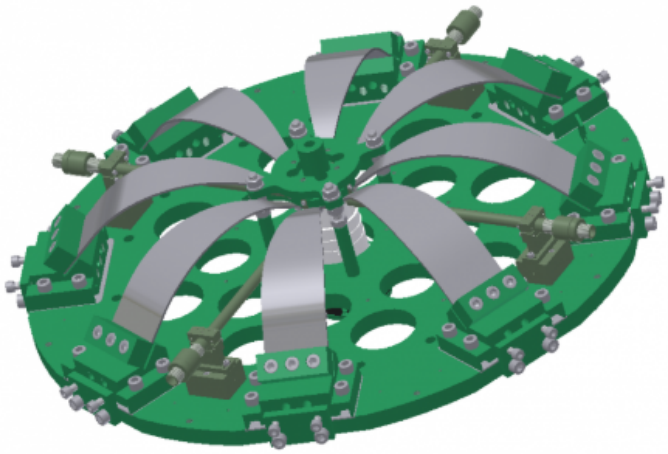

Figure 1.20: CAD model of a GAS-filter [34]

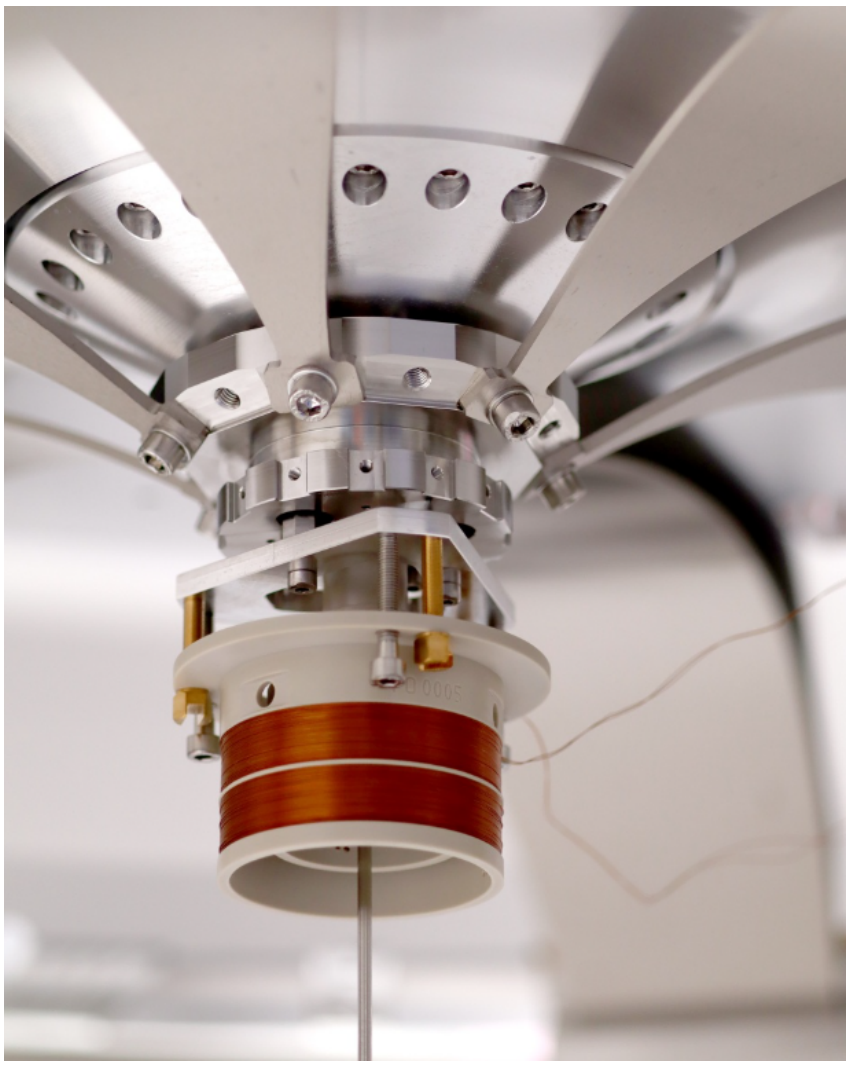

Figure 1.21: LVDT on a GAS-filter to monitor displacements [17]

Apart from the four mirror towers there are two more towers that have suspended benches for optical components like beam splitters and smaller steering mirrors. Together, these send in and read out the laser beams, but also managing and manipulating them. This equipment also needs to be isolated from vibrations [15]. The suspension of these benches also starts with a large inverted pendulum, followed by 3 GAS-filters and a bench that acts as a regular pendulum. Figure 1.22 and 1.23 show respectively a schematic representation of the bench tower suspension system and a picture where the 3 GAS-filters can be seen. Smaller bench-top suspensions like an HAM Relay Triple Suspension (HRTS) are placed on the optical table for a more refined isolation. Figure 1.24 shows a picture of an HRTS-system. Inside these, there are several BOSEM position sensors, and they are very close to each other. The usage of HRTS on the bench is rather new. It is constructed for the LIGO update and ETpathfinder ordered them as well. In the future the BOSEM's might be replaced by LVDT's or RLVDT's. It is in this specific case that the interference has to be studied, since the sensors are so close.

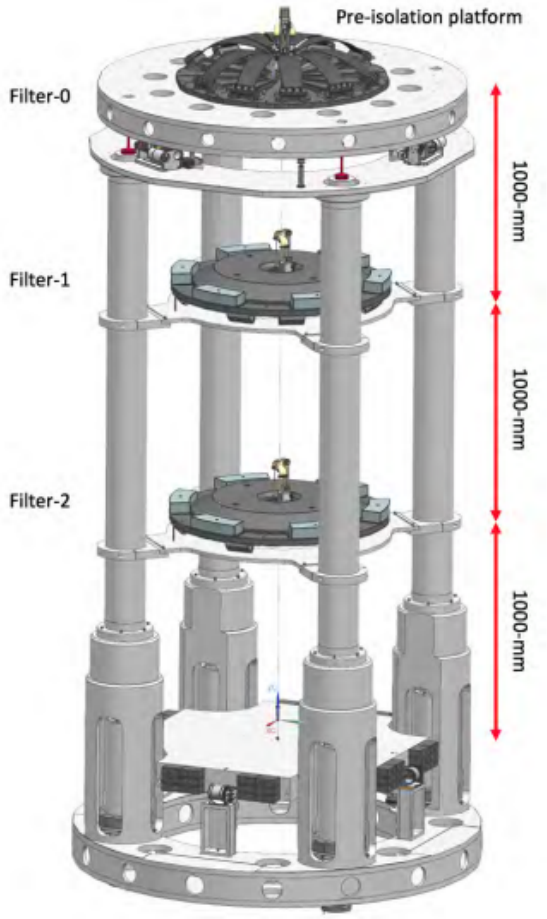


Figure 1.22: Schematic representation of the bench suspension [15]

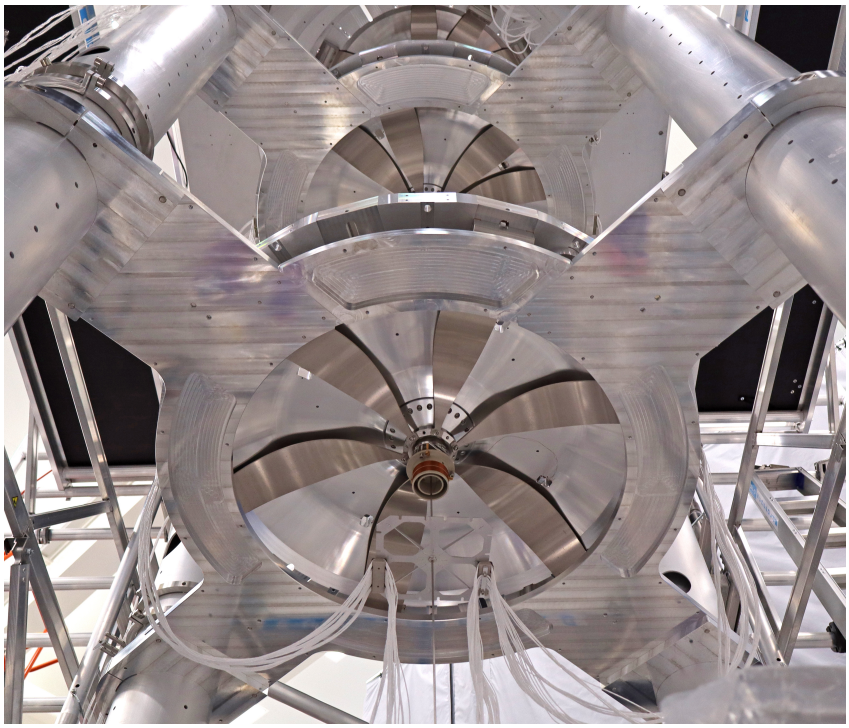

Figure 1.23: Picture of the GAS-filters of the bench tower (under construction) [39]

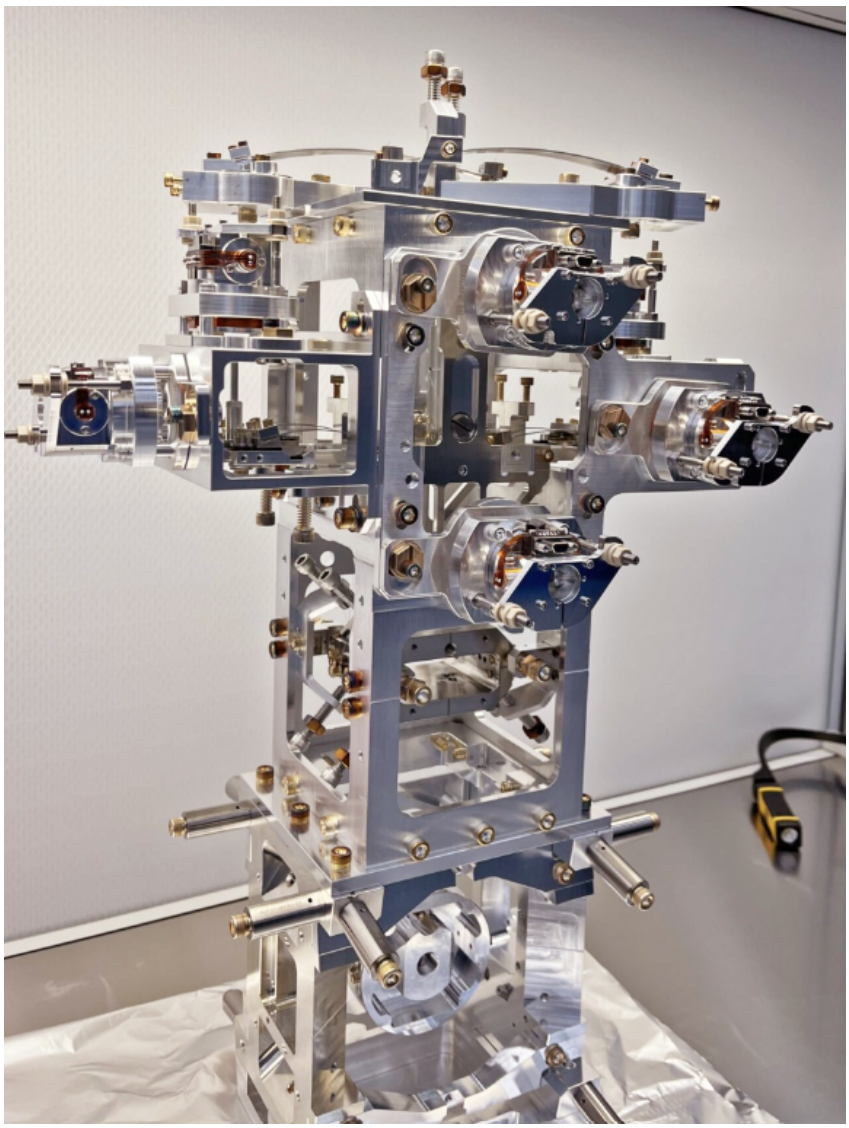

Figure 1.24: Picture of an HRTS system [38]

## 1.5 Linear Variable Differential Transformer (LVDT)

LVDT's have a key role in monitoring the precise position of the mirrors, but can also be used in accelerometers and future HRTS-systems. In this section, the theory of LVDT's is given.

### 1.5.1 Operating Principle

An LVDT consists of three coaxial solenoidal coils and a neodymium magnet as a core. The primary coil (inner coil) is centered between two secondary coils (outer coils), connected in series. Figure 1.25(a) shows a picture of an LVDT and Figure 1.25(b) gives a schematic representation of a cross-section of an LVDT [35].

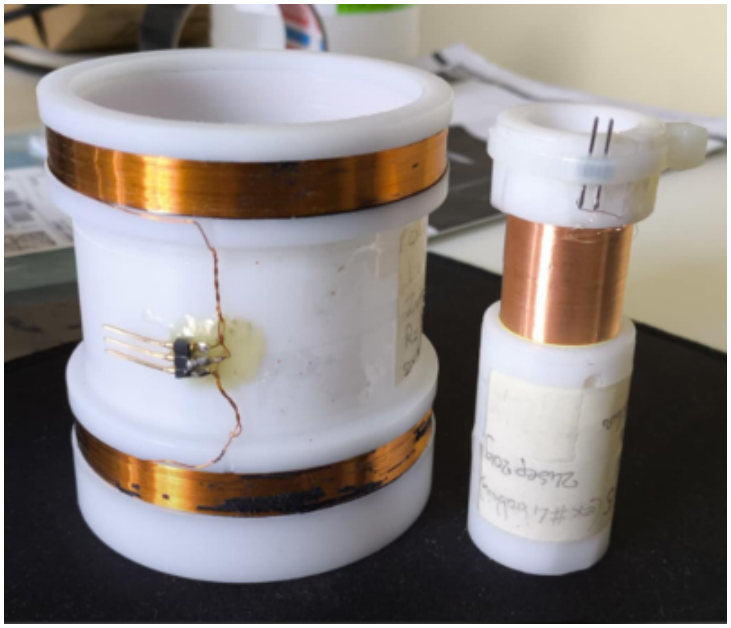

((a)) Picture of an LVDT where the inner coil (right) is taken out for visibility [20]

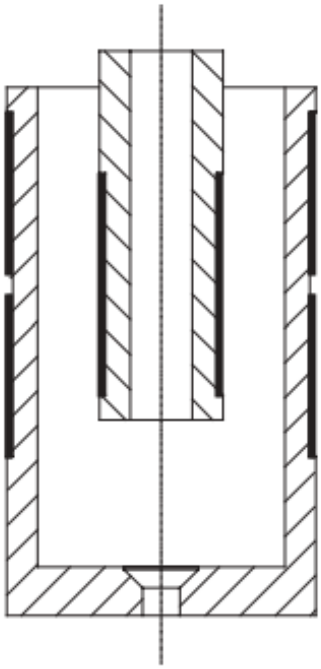

((b)) Schematic representation of an LVDT [35]

The primary coil is excited with a sinusoidal voltage of 10 kHz:

$$V_p(t) = V_0 \sin(\omega t). \tag{1.49}$$

This alternating current produces a changing magnetic flux, which couples inductively to the outer coils. According to Faraday's law of induction, the induced voltage in each outer coil is given by:

$$\mathscr{E}_{o_i}(t) = -N_i \frac{d\Phi_{B,i}}{dt}, \tag{1.50}$$

where $\Phi_{B,i}$ is the magnetic flux in the $i^{\text{th}}$ outer coil and $N_i$ the number of windings of the $i^{\text{th}}$ outer coil. For the LVDT-purpose, the number of windings in both coils is equal but direction of winding of the outer coils is opposite, so that their outputs are differential:

$$V_{\text{out}}(t) = V_{o_1}(t) - V_{o_2}(t). \tag{1.51}$$

When the inner coil is exactly in the middle of two outer coils, the mutual inductance is the same, resulting in equal and opposite voltages $V_{o_1} = V_{o_2}$, and hence $V_{\text{out}} = 0$. As the core moves away from the center, the induction in one outer coil increases while it decreases in the other, leading to a non-zero output voltage. This relation is approximately linear, if the displacement is not too big, represented in Figure 1.26 [18, 35, 56].

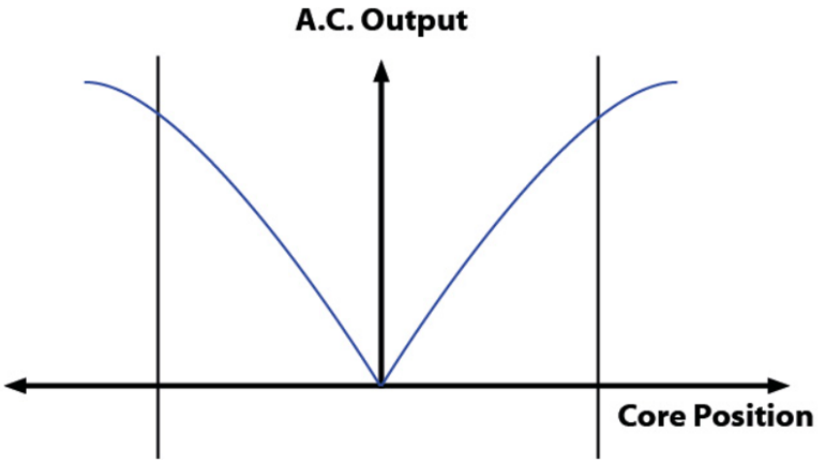


Figure 1.26: Output of an LVDT [18]

In this picture, the output is given as an absolute value, resembled by the V-shape. For linearity studies in a later chapter, the LVDT output is given with non-absolute voltages, since it makes the study more convenient. The output then looks like a $y = ax$ function, as can be seen on e.g. Figure 3.16. The physics and interpretation is the same for both cases.
The sensitivity of an LVDT can be characterized by the slope of the linear region. The slope is expressed as V/mm. A sensitive LVDT will generate more voltage per unit of displacement.
Since the slope is proportional to the excitation voltage we normalize the output by the excitation voltage. Therefore the response curve will be expressed with the unit $V/V_{exc}$ and the slope will be expressed as $V/\text{mm}V_{exc}$.

### 1.5.2 Position Sensing and Feedback Control

By using LVDT's in the suspensions and optical tables, we are able to register displacements with sub-micrometer accuracy. Every displacement is translated into a voltage signal by the LVDT.
The LVDT setup can also be used for active feedback, by including a voice coil (VC). Applying a DC signal to the outer coils will move the magnet (with the inner coil) due to the Lorentz force. So if a displacement is registered by the LVDT, we can use the VC function to get it back in place [61, 15].

### 1.5.3 Reversed LVDT

The LVDT-VC combination requires complex electronics. For the LVDT function, the inner coil is excited and the outer coils are read out while for the VC function, the outer coil are getting a current. This problem can be solved when using a reversed LVDT (RLVDT). The idea is the same, but instead of exciting the inner coil and reading out the outer coils, the roles get reversed. We excite the outer coil and read out the inner coil. When a displacement is registered, we can easily add a DC signal to the AC-excitation to move the magnet. However, this method makes the inner coil, and thus the registered displacement, more sensitive to noise. The readout of the normal LVDT is a differential voltage, eliminating background noise $n$.

$$V_{\text{diff}} = (V_1 + n) - (V_2 + n) = V_1 - V_2 \tag{1.52}$$

For the reversed LVDT, there is no such noise elimination. To use the RLVDT, we should optimize the set-up to make sure the inner coil does not sense any other magnetic field than the intended one, or minimize it as much as possible [31].
Currently, the RLVDT's are not yet used. Therefore, this thesis will test and study if they are usable. Does the excitation of the outer coils lead to an oscillation of the magnet? I.e. does it act like a voice coil at very high frequencies? This will be studied in chapter 3. On the other hand, is the background noise manageable? We could make electronics that will do advanced signal processing, but this makes it again more complex, taking away the advantage of using the RLVDT. Another option to deal with noise could be shielding. This will be the main topic of the thesis. Research about the readout has been done [5] and it can be concluded that the output is the same. Figure 1.27 shows the magnetic flux density for the LVDT (left) and RLVDT (right), while the magnetic field does not look the same, their output is, as can be seen at Figure 1.28.

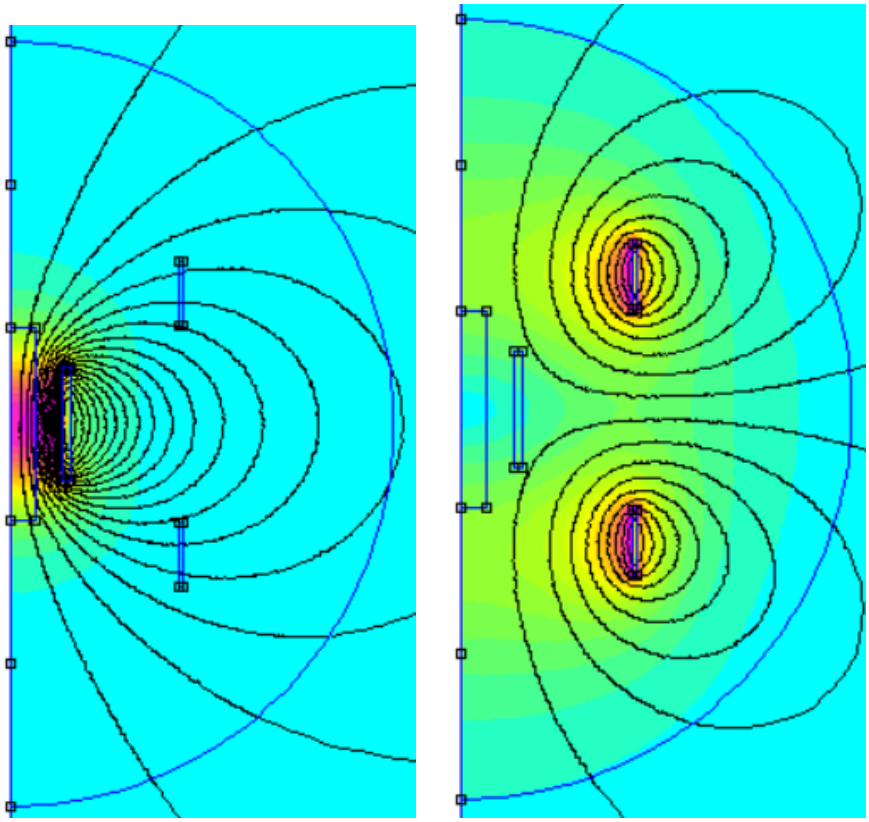

Figure 1.27: Magnetic flux density for an LVDT (left) and RLVDT (right) [19]

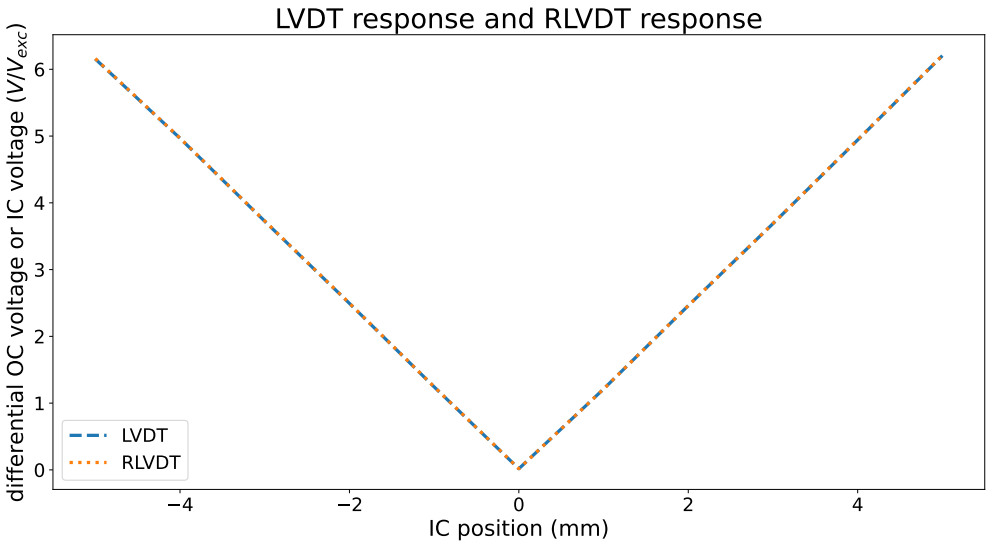


Figure 1.28: Output comparison between the LVDT and RLVDT of the same geometries [21]

In this figure, IC stands for inner coil and OC for outer coil.
Now that the reader knows what an LVDT is, how it works and what it looks like I can refer back to Figure 1.21.
Additionally, to show again how frequently used the LVDT's are in the suspensions, Figure 1.29 shows a picture where all the LVDT's are circled in red.

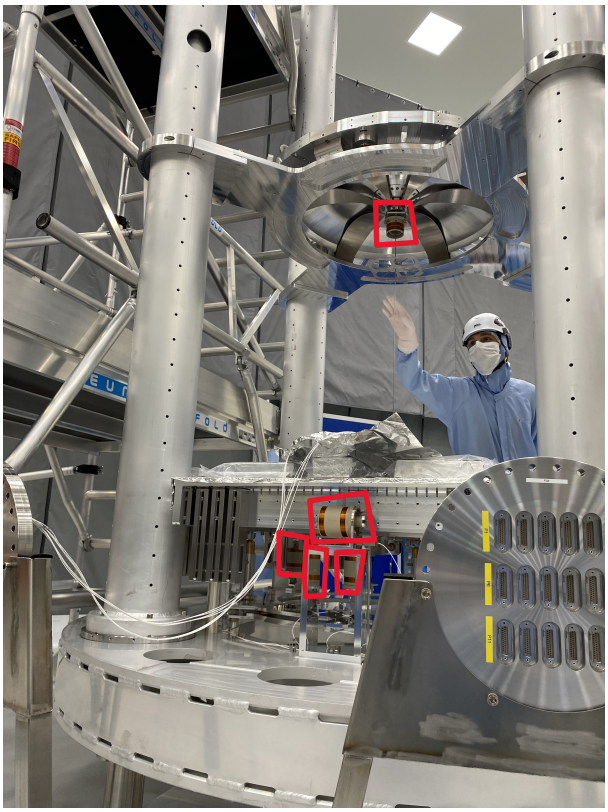

Figure 1.29: Picture of a suspension system from ETpathfinder with 5 LVDT's [17]

## 1.6 Electromagnetism

This section is to explain theoretical concepts in the field of electromagnetism that will be used throughout the thesis and is important since LVDT's are electromagnetic displacement sensors.

### 1.6.1 Eddy Currents

Eddy currents are circular loops of electric current induced within conductors because of a changing magnetic field. Their existence is explained by Faraday's law of induction, which states that an electromotive force (EMF) is generated when the magnetic flux changes over time. This electromotive force works on the free electrons in the material. Faraday's law is given by:

$$\mathscr{E} = -\frac{d\Phi_B}{dt} \tag{1.53}$$

where $\mathscr{E}$ is the induced EMF and $\Phi_B$ the magnetic flux. The generation of eddy currents can also be described using the Maxwell–Faraday law.

$$\nabla \times \mathbf{E} = -\frac{\partial \mathbf{B}}{\partial t} \tag{1.54}$$

This equation shows that a time-varying magnetic field induces a circulating electric field. In a conductor, this induced electric field drives electrons in closed circular loops, forming eddy currents. This is represented in Figure 1.30 [48, 44].

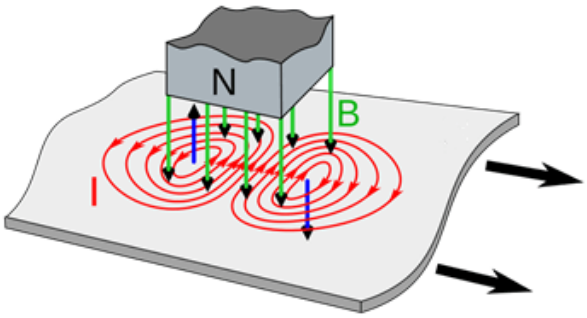


Figure 1.30: Representation of the generation of eddy currents. A metal plate is moving through a magnet, such that the local flux is changing [44].

At high frequencies, these eddy currents are largely confined to the surface of the conductor due to the skin effect. The depth to which they penetrate is called the skin depth $\delta$ and is defined by the dept where the current density is $1/e$ (with $e \approx 2.71828$, Euler's number), around 37%. The general formula for skin depth is given by:

$$\delta = \sqrt{\frac{2\rho}{\omega\mu}\left(\sqrt{1+(\rho\omega\varepsilon)^2}+\rho\omega\varepsilon\right)} \tag{1.55}$$

Where $\rho$ is resistivity, $\mu$ the relative permeability, $\varepsilon$ the relative permittivity and $\omega = 2\pi f$ the angular frequency of the magnetic field. But for frequencies much lower than $1/(\rho\varepsilon)$, the brackets yield something that is close to 1 such that the skin depth can get approximated by

$$\delta = \sqrt{\frac{2}{\omega\mu\sigma}}, \tag{1.56}$$

Where $\sigma = 1/\rho$ is the conductivity [59].
As the eddy currents flow, they produce secondary magnetic fields which oppose the magnetic field according to Lenz' law, they act against the change in magnetic flux. The opposing magnetic field generated by eddy currents is a consequence of Ampère's circuital law [45]:

$$\nabla \times \mathbf{B} = \mu_0 \mathbf{J} \tag{1.57}$$

This says that a current density gives rise to a circulating magnetic field.
This principle can be used in high frequency magnetic shielding: by enclosing sensitive components in conductive materials such as copper or aluminum, the induced eddy currents in the shield generate magnetic fields that oppose and partially cancel the original, unwanted, magnetic field [43, 48].

### 1.6.2 AC shielding

Magnetic shielding is often done with ferromagnetic materials. These materials have a high magnetic permeability, meaning the magnetic field lines will be redirected to go inside the material, taking away the magnetic flux behind the material. Higher permeability means that the material is better at redirecting the field lines, and are therefore better shielding materials. Non-ferromagnetic materials like copper or aluminum have a permeability like air. They do not have the ability to redirect the field lines.
For high frequency AC fields the shielding ability of the ferromagnetic materials disappears because of the drop in permeability. This paragraph is to explain the physics of the collapse of the permeability at high frequencies. The general expression of (frequency dependent) permeability is

$$\mu(\omega) = 1 + \chi_{dw}(\omega) + \chi_{sp}(\omega) \tag{1.58}$$

where $\chi_{dw}$ is the domain wall susceptibility and $\chi_{sp}$ the spin resonance susceptibility.

$$\chi_{dw}(\omega) = \frac{\chi^0_{dw}\omega^2_{dw}}{\omega^2_{dw} - \omega^2 + i\omega\beta/m_{dw}} \tag{1.59}$$

where $\chi^0_{dw}$ is the static domain wall susceptibility and $\omega_{dw} = \sqrt{k/m_{dw}}$ is the domain wall resonance frequency, the eigenfrequency of the domain wall. Above $\omega_{dw}$ (a quantity depending on the material properties, 1 kHz for Mu-metal) the susceptibility $\chi_{dw}$ decreases as $\omega^2$ and will therefore be negligible at 10 kHz.
When domain walls freeze out ($\omega \gg \omega_{dw}$), permeability relies on spin rotation, the reorientation of magnetic moments within domains. This process is described by the Landau-Lifshitz-Gilbert equation:

$$\frac{d\mathbf{M}}{dt} = -\gamma \mathbf{M} \times \mathbf{H}_{\text{eff}} + \frac{\alpha\gamma}{M_s}\mathbf{M} \times (\mathbf{M} \times \mathbf{H}_{\text{eff}}) \tag{1.60}$$

where $\mathbf{M}$ is the magnetization, $\gamma$ is the gyromagnetic ratio, $\alpha$ is the damping factor, $\mathbf{H}_{\text{eff}}$ is the effective magnetic field and $M_s$ is the saturation magnetization, the maximal magnetization a material can achieve. The link between magnetization and susceptibility is given by $\chi = \frac{\partial M}{\partial B}$. After solving, the spin resonance susceptibility follows a Debye relaxation model:

$$\chi_{sp}(\omega) = \frac{\chi^0_{sp}}{1 + i\left(\frac{\omega}{\omega_{sp}}\right)} \tag{1.61}$$

where $\omega_{sp} = \gamma\alpha\mathbf{H}_{\text{eff}}$ is the relaxation time of spin rotational magnetization. For $\omega > \omega_{sp}$ the spins lag behind the AC field, reducing $\chi_{sp}$. So if we substitute Equation 1.59 and Equation 1.61 into Equation 1.58 we see that for high frequencies the relative permeability indeed goes back to 1 [6, 32, 25, 27].

## 1.7 Research Topic

Can RLVDT's be used? The LVDT's in the big suspension systems and mirror towers are usually far away from each other and other kinds of electromagnetic sources, so that the change to RLVDT's can be realized. However, RLVDT's can also used in accelerometers and smaller bench-top suspensions like the HRTS. Here, the RLVDT's will be very close to each other so that interferences and mutual inductance's might be problematic. It is in cases like these, that we want to know if noise like this can be minimized. Shielding is the main idea to achieve this goal, which is where this thesis will focus. Different materials and geometries will be studied to understand their shielding effectiveness, but also their influence on the RLVDT response. This will be done with numerical simulations and experimental measurements. The design and optimalisation of the shielding will be studied with FEMM-simulations to get a detailed understanding of the electromagnetic interactions. The influence of an adjacent RLVDT will be studied, both experimentally and through simulations. It is essential to understand these interactions when having multiple sensors close to each other. Through experimental research, we also check the possibility of exciting RLVDT's at different frequencies to reduce the interference and mutual inductance.
In addition to shielding, the sensitivity of the RLVDT as a function of excitation frequency will be examined. This includes analyzing the impact of different excitation frequencies on both signal quality and the dynamic response of the system. To give an idea how extensively used the LVDT's are in ETpathfinder, Figure 1.31 is shown. On this picture it can be seen that there are 46 LVDT's in the mirror tower and currently 13 LVDT's in the bench tower. Given that there are 4 mirror towers and 2 bench towers, in ETpathfinder there will be 210 LVDT's. Add to this the potential use of LVDT's instead of BOSEM's in HRTS-systems. In ET, which will much more, higher and more complex towers, there will be in the order of a few thousands LVDT's. It can easily be concluded that LVDT's will be a very important element in the future Einstein Telescope, illustrating the importance of this thesis if the LVDT's will be transformed into RLVDT's.

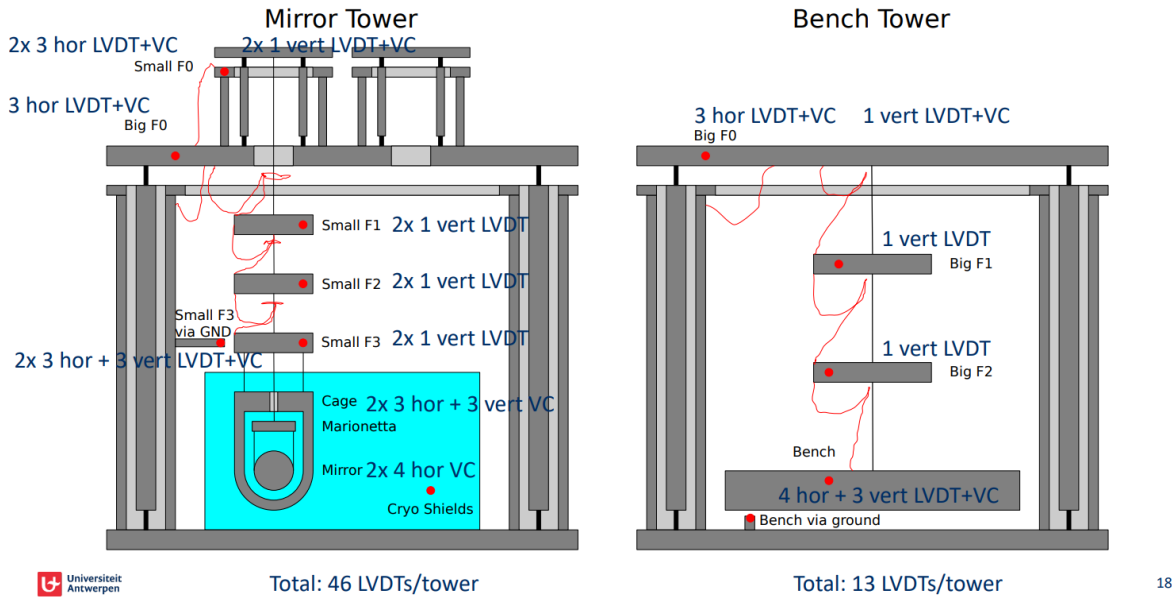


Figure 1.31: Overview of LVDT usage in ETpathfinder [40]

# 2 Methodology

> **"A good methodology does not guarantee success, but a poor one almost always guarantees failure."**
> ***Gerhard Lenski***

To investigate the shielding effectiveness and performance of RLVDT's, a combination of numerical simulations and experimental analysis is used. This approach allows for both theoretical insight and practical validation of the shielding.

## 2.1 Numerical Simulations

Numerical simulations are performed using the *Finite Element Method Magnetics* (FEMM) software. This is designed to study two-dimensional planar or (conceptually) 3D-axisymmetric electromagnetic problems via the Finite Element Method (FEM).
FEM is a numerical approach for solving, in this case, electromagnetic problems by dividing complex geometries into small, manageable elements (see Figure 2.1). It calculates magnetic fields, currents, and forces by solving Maxwell's equations over these discretized regions.
FEMM allows the user to add nodes (black squares) and lines or arcs (blue). By combining these one can draw shapes like rectangles, triangles or more complex shapes. These shapes can be assigned material properties by adding blocklabels (green squares) and selecting the material. This material can be a preinstalled material but it also allows to create a new material and assigning it the correct values like conductivity, permeability,... For coils, it is possible to specify the number of turns, wire size and assign them a certain circuit, which is characterized by series/parallel and the current that goes through them. In order to solve a problem, boundary conditions are necessary. The boundary conditions are specified by the semicircle seen on (Figure 2.1). The studies performed in this thesis used consistently Dirichlet boundary conditions [29, 49].

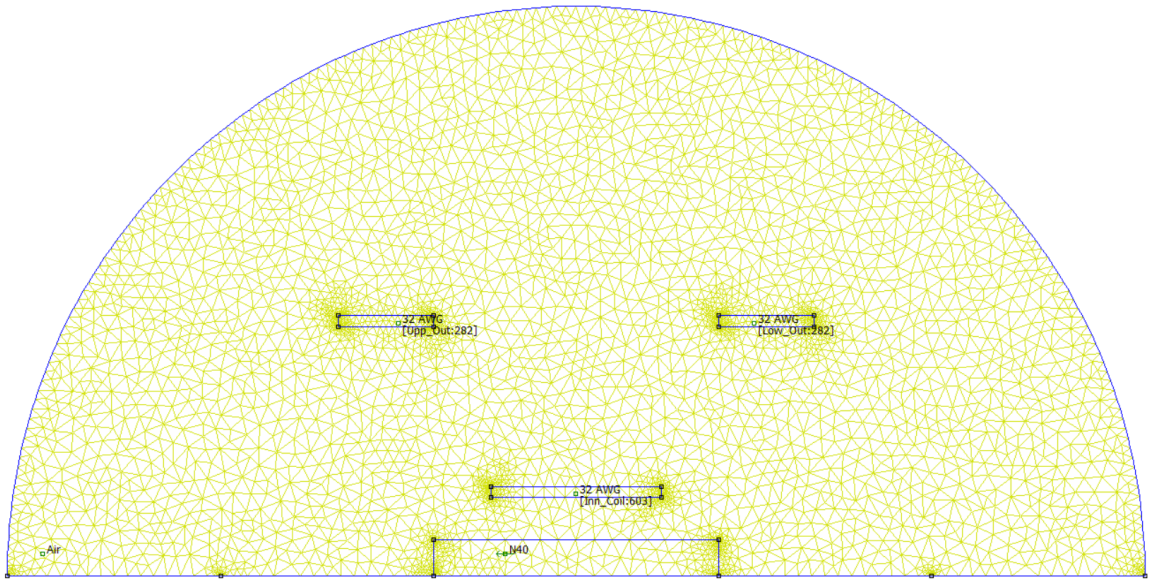


Figure 2.1: Meshgrid: the division of the problem into small finite elements (rotated over 90°) [19]

FEMM can be accessed via the application itself or by making use of pyFEMM, the Python interface to FEMM. It is the latter method that will mainly be used because of convenience and proficiency.
To evaluate the sensitivity of the RLVDT, the inner coil structure is displaced in discrete steps along the axis of symmetry, this is usually done over a range of $\pm 5$ mm around the center with steps of 0.5 mm. For each position, FEMM computes the magnetic field, generated eddy currents,... to then be able to return the induced voltage amplitude in the secondary coils. Plotting the resulting voltage against the core position yields an approximate linear relationship within a defined operational range. The degree of linearity is quantified as alinearity or linearity deviation, which will be introduced and discussed in detail in a later chapter.
In addition to sensitivity and linearity analysis, FEMM simulations are used to investigate the effect of magnetic shielding. By computing the spatial distribution of the magnetic flux density **B** with and without shielding materials, it is possible to assess the attenuation performance of different shield configurations. The comparative analysis provides quantitative insight into the order of suppression and field leakage.

### 2.1.1 Planar vs Axisymmetric

Figure 2.2 illustrates two types of geometrical configurations of the LVDT used in the modeling: a planar cross-section and an axisymmetric formulation. The latter better reflects the physical structure of the LVDT but because of the symmetry, it is not possible to add a second LVDT and study the interaction between the two, or to add a new source and study the shield efficiency. For this reason, studying shielding effects, LVDT interference and source influence will mainly be done using the planar configuration, while studying shielding influence on LVDT response (sensitivity and linearity) will be done in the axisymmetric configuration.

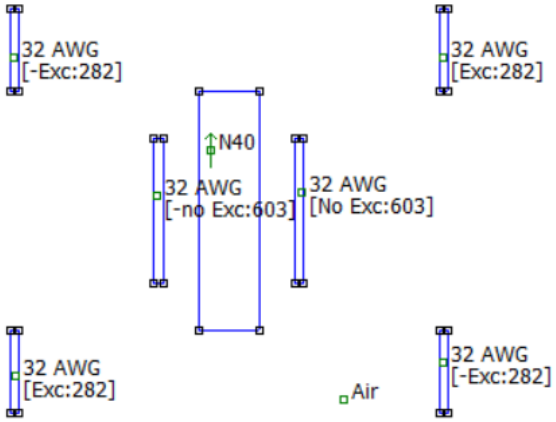


((a)) Planar $(x, y)$: a cross-section of the coils and magnet. The (0,0)-coordinate is at the center of the magnet [19].

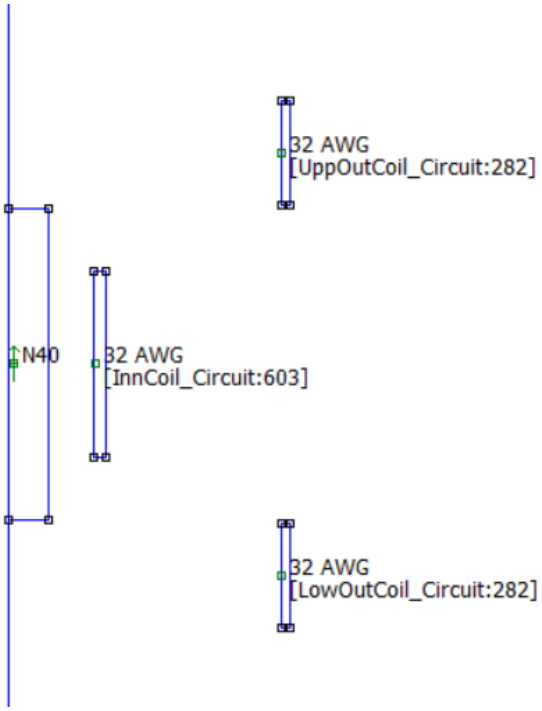


((b)) Axisymmetric $(\rho, z)$: when calculating, the software will, conceptually, make a $2\pi$ rotation around the $z$-axis and integrate the results [19].

Figure 2.2: FEMM modeling approaches: planar and axisymmetric geometries.

To make sure that these configurations are compatible, the magnetic flux density is analyzed along a vertical line to check if the pattern is the same. Since the outer coils resemble a Maxwell-coil we know what to expect. On the axis of symmetry ($x = 0$) for planar, ($\rho = 0$) for axisymmetric, we should get two maxima where the coils are and between the coils we expect a linear region that becomes zero in the middle between the coils. The linear region is a consequence of the constant gradient $\frac{dB}{dZ}$ between the coils, a property of the Maxwell coil. Off-center ($x \neq 0$, $\rho \neq 0$) we expect a more rounded profile, the slope is less steep and the linear region is blurred. There should be no zeropoint because there is a loss

of symmetry [57, 28, 1]. Figure 2.4 shows the simulated results for a vertical line at position $x = \rho = 0$ and an off-axis vertical line at distance $x = \rho = 25$ mm. This figure will have the $x$-axis expressed in distance, this is the distance on the vertical line, not the distance from the vertical line to the central axis. The $y$-value at e.g. $x = 50$ mm gives the $y$-value 50 mm after the start of the vertical line. Figure 2.3 shows the vertical line at distance $\rho = 25$ mm for the axisymmetric case.

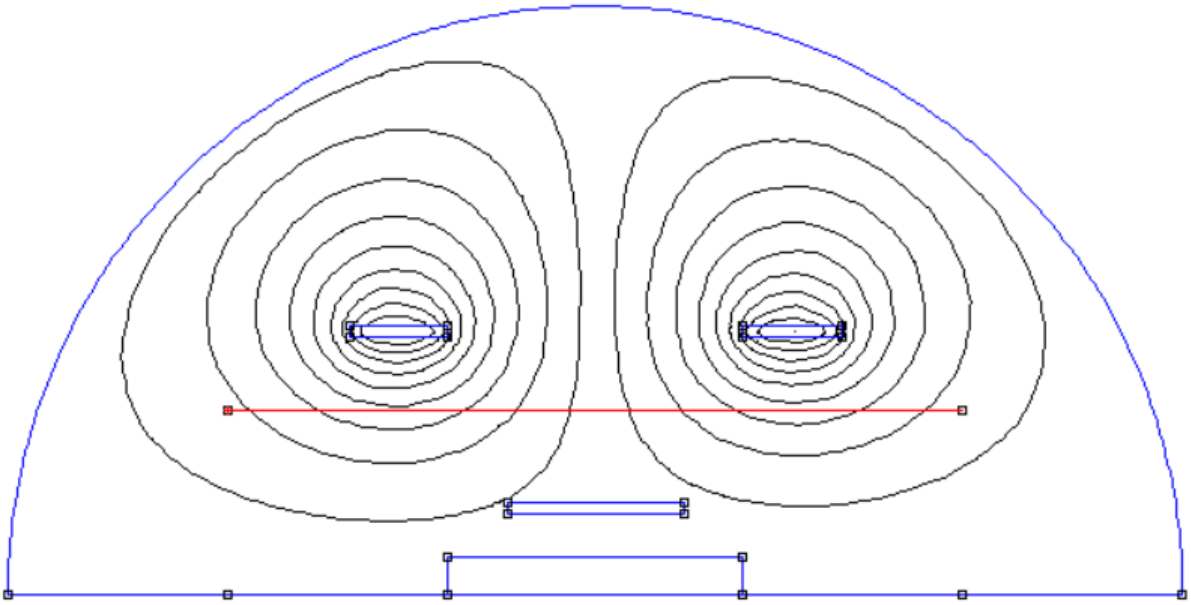

Figure 2.3: Axisymmetric RLVDT model with a vertical line at $\rho = 25$ mm (rotated over 90°) [19]

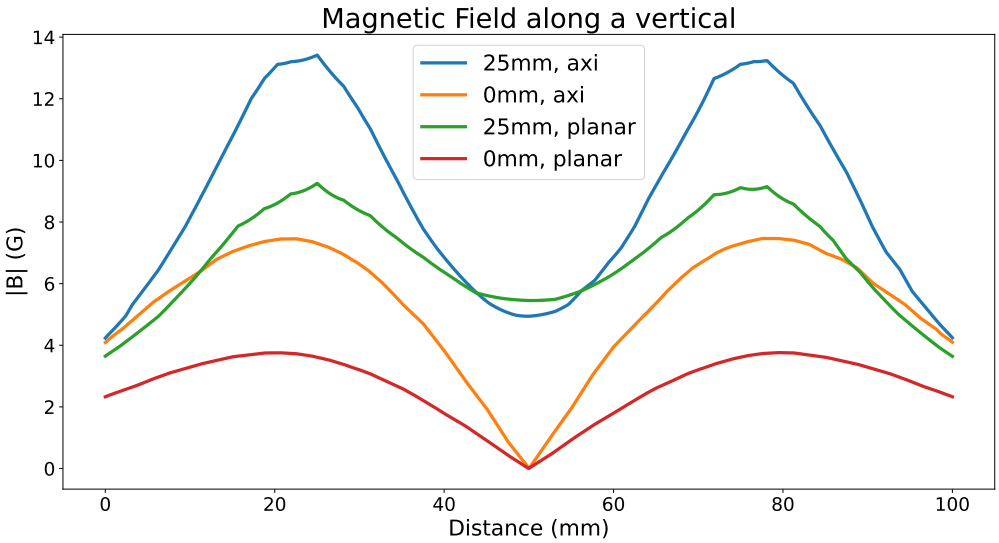


Figure 2.4: Absolute value of the magnetic flux density along a vertical line with constant $x$ or $\rho$ [21]

There is no exact overlap, which can be explained by the fact that the planar configuration has four separate, unlinked sources, while the axisymmetric solver "knows" that we have a full coil, so it integrates over $2\pi$. Fortunately, the main shapes are similar and what was expected for a Maxwell Coil. This indicates that we can confidently use both situations, but keeping in mind that the values of the planar simulations will differ.

### 2.1.2 Implementation of the shield

In the axisymmetric case, the shield can be implemented in two different ways, either as one block, or in three distinct blocks representing the cylindrical shell, the top circular disc and the bottom circular disc. In the case of three different blocks, there is a space of 0.5 $\mu$m between them. Based on previous experiences, FEMM tends to give results that are not agreeing with expectations when using complex shapes. In order to decide which of the shield implementations will be used, a study was done that compared the magnetic flux density and eddy current density inside the shield for both possibilities. Figure 2.5 shows the implementation of a shield, in this case the one-block shield, with the contour that is used to determine the densities. The magnetic flux density comparison is shown in Figure 2.6 and the eddy current density comparison in Figure 2.7. These figures will have $x$-axis expressed in length, this is the length of the contour. The $y$-value at e.g. $x = 50$ mm gives the $y$-value 50 mm after the start of the contour, in this case top-left. The shield has a radius of 60 mm, a height of 80 mm and a thickness of 2 mm.

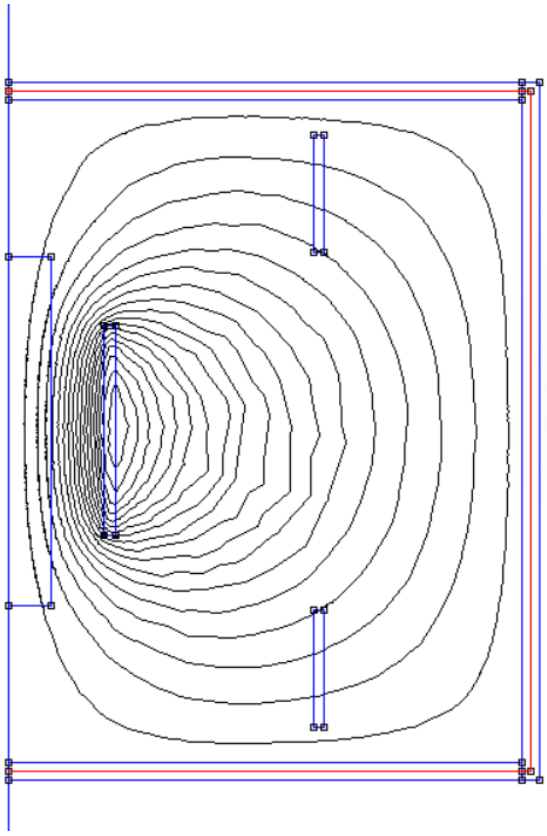

Figure 2.5: The contour (red) along which the flux density and eddy current density are taken [19]

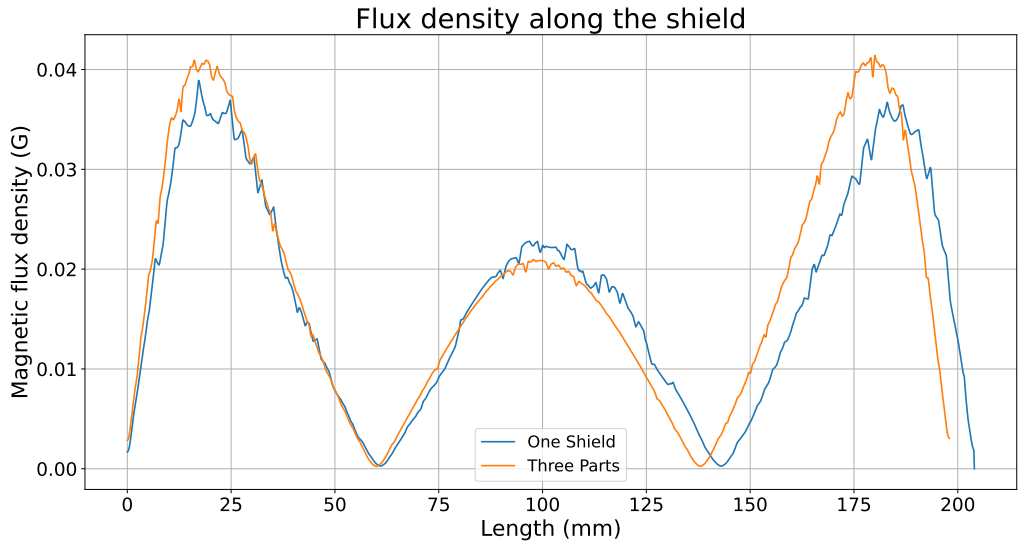


Figure 2.6: Absolute value of the magnetic flux density along the shield, expressed in Gauss [21]

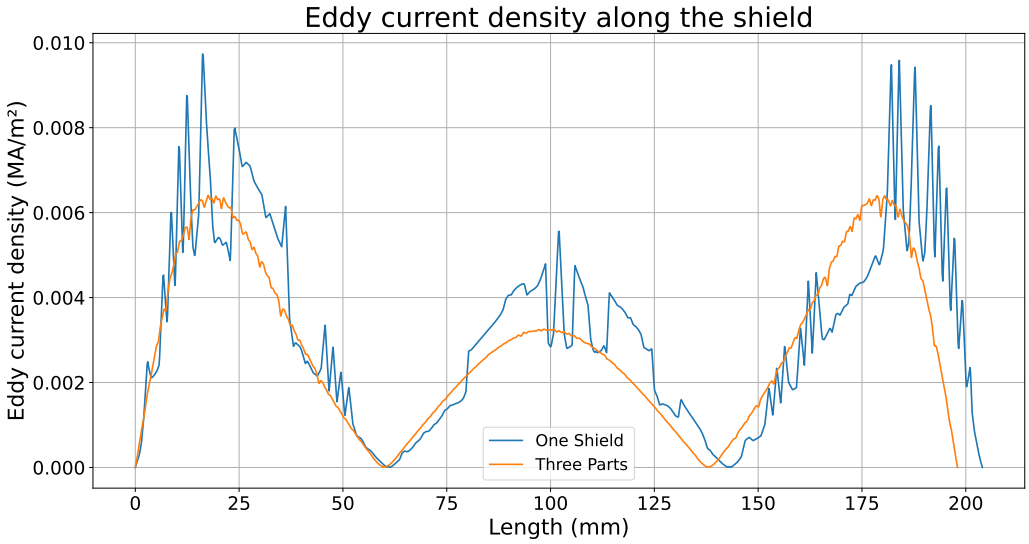


Figure 2.7: Eddy Current Density along the shield [21]

Based on these figures, it is decided that the configuration of three separate blocks will be used to implement the shield. The one-shield method has extreme oscillations in the eddy current density that, from the theory perspective, should not be there. This is probably due to numerical errors. The reason that the one-shield curves go a little bit further is an implementation error.

### 2.1.3 Materials and Conventions

To prevent giving all the details about the materials and geometries of the RLVDT's throughout the entire thesis, they are mentioned in this paragraph. Unless specified otherwise, these are the specifications used.

The LVDT and RLVDT geometries that are used in all the simulations are based on the LVDT type-A, designed by NIKHEF [26]. The magnet used is an N40 neodymium permanent magnet (with the label N40 in FEMM), it has a radius of 5 mm and a total height of 40 mm. The inner coil has an inner radius of 11 mm, a thickness of 1.4 mm and a height of 24 mm. It is winded with copper wire of the type 32 AWG, has 603 turns spread over 6 layers. The two outer coils have an inner radius of 35 mm, a thickness of 1.2 mm, and have a height of 13.5 mm. They are 54.5 mm apart from each other. The outer coils are also winded with 32 AWG, with 282 windings spread over 5 layers. The frequency of the excitation is always 10 kHz and the current given is $I = 0.0076$ A or $I = 0.02$ A, this will be mentioned in the sections.
To study the shielding, preinstalled materials are used. In FEMM they are called 'Aluminum, 1100', 'Pure Iron', 'Copper', 'Mu Metal' and '430 Stainless Steel', which we will refer to respectively as 'aluminum', 'iron', 'copper', 'mu-metal' and '(stainless) steel'. Mu-metal is an alloy with very high permeability ($\mu_r = 80000 - 100000$), often used for electromagnetic shielding purposes [12]. FEMM makes use of pure iron, which has a permeability of $\mu_r \approx 200000$, this is not achievable in real life.

## 2.2 Experiments

### 2.2.1 Experimental Set-Up

For the experiments, we used the experimental setup that was available at the University of Antwerp. It is a fully customized setup developed by both physicists and engineers, made from 3D-printed pieces and components made in the UA workshop.
The setup has an aluminum frame standing on an vibration isolation table. The support for the outer coils is partly made with a 3D-printer and represents a stable reference. It has incorporated a leveling system to perfectly align the coils. The inner coil is attached from above, from where it can be controlled. The inner coil system has a vertical and horizontal step motor to move the inner coil with micrometer accuracy. It has a laser that can determine the position of the inner coil to sub-micrometer level. Additionally, there is a scale that can be used to measure the VC-force. The laser and the scale were not used for the experiments performed in this thesis. Figure 2.8, 2.9 and 2.10 show respectively the whole setup, the inner coil system and the LVDT part, both a CAD representation a real photo.

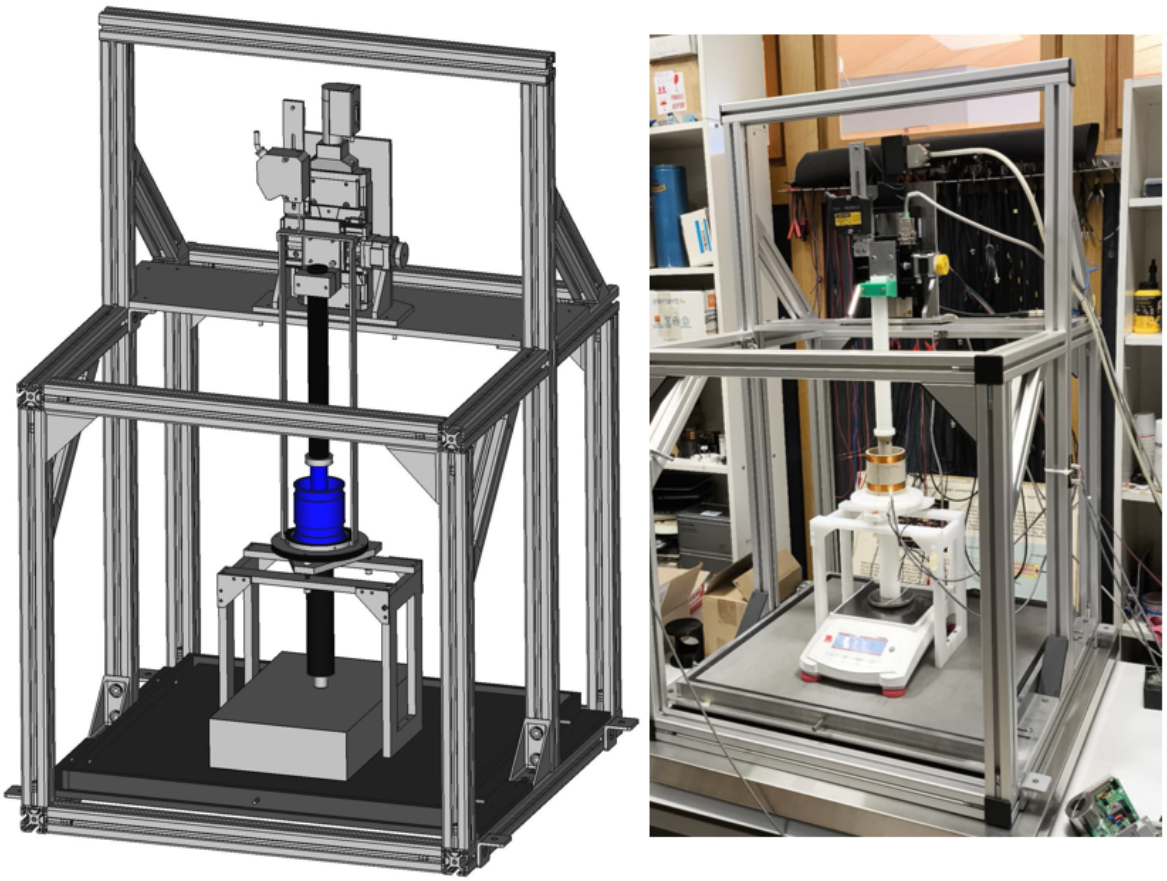

Figure 2.8: Left: CAD representation of the full set-up [38]
Right: actual photograph of the full set-up [20]

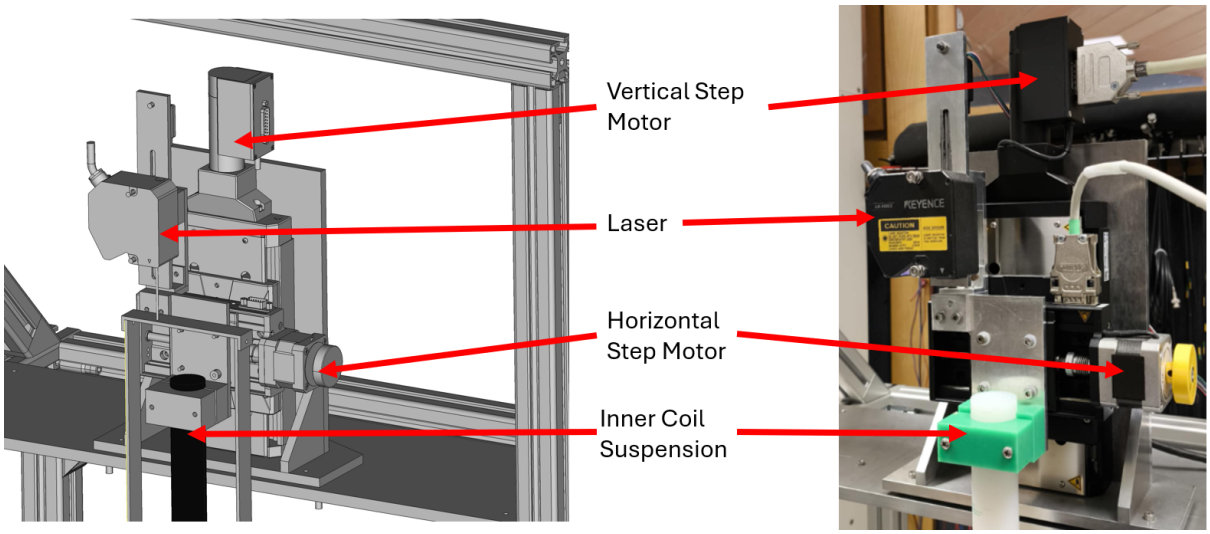


Figure 2.9: Left: CAD representation of the inner coil suspension [38]
Right: actual photograph of the inner coil suspension [20]

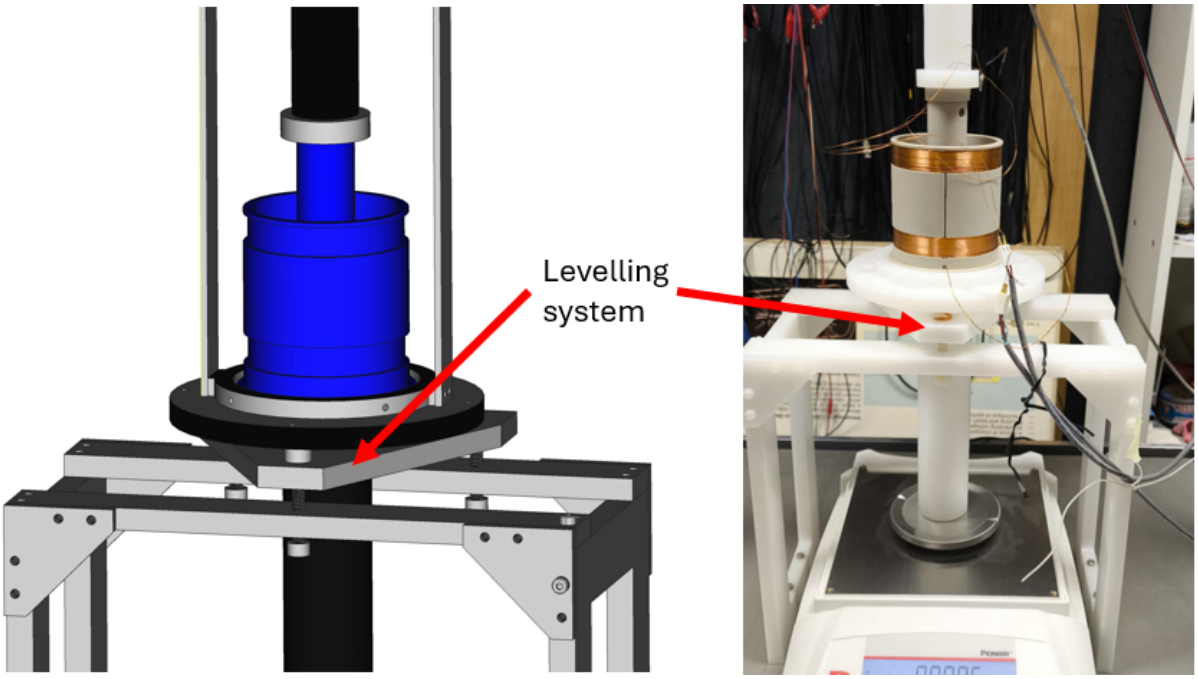


Figure 2.10: Left: CAD representation of the LVDT-part [38]
Right: actual photograph of the LVDT-part [20]

### 2.2.2 Add-on's

The experimental part of this thesis will focus on the influence of a second RLVDT (i.e. the excitation of the outer coils) on the main RLVDT (i.e. the signal registered by the inner coil). To do this, a support for the extra outer coils is needed. Since 3D-printing is a time consuming and expensive process, an alternative construction method was used: LEGO®. This made it possible to add a second RLVDT and even make it possible to create something that can hold the outer coils at a certain angle. For the shielding problem, an aluminum sheet was placed in between both RLVDT's. Figure 2.11 gives a picture of the new support for the second RLVDT and Figure 2.12 shows the angle holder.

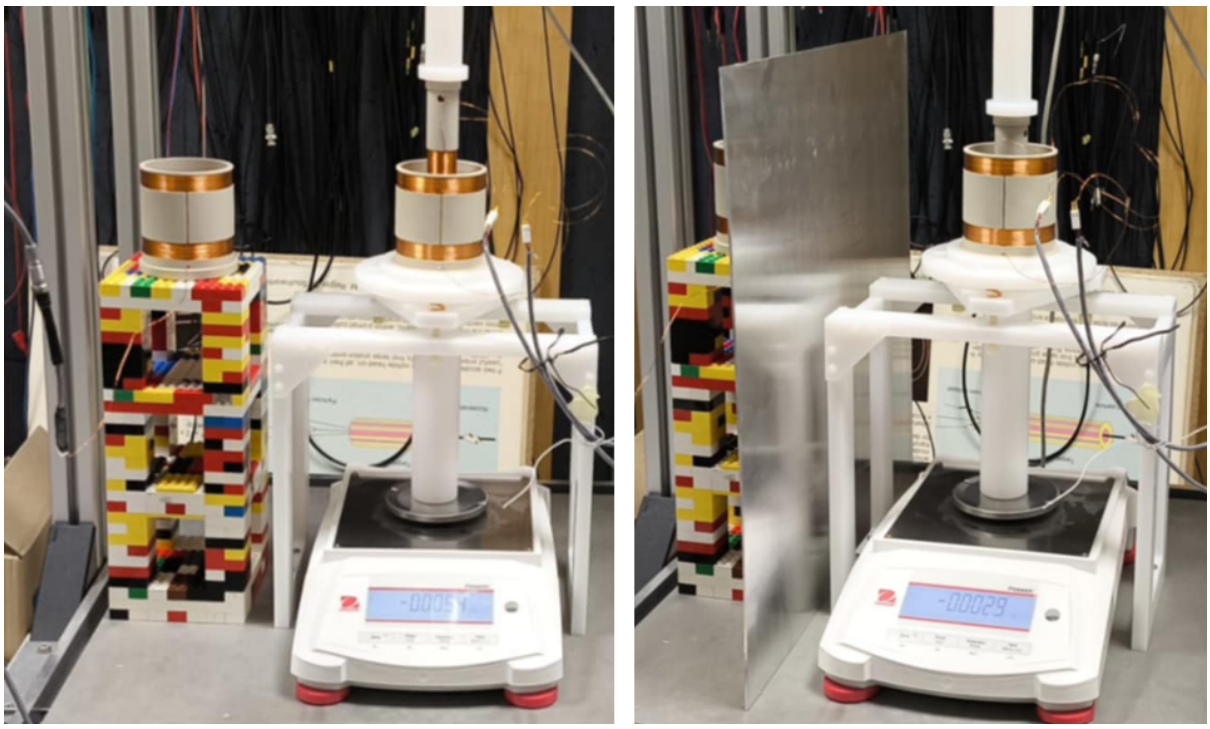

Figure 2.11: Left: two RLVDT's, one on the main suspension and one on the LEGO®-suspension
Right: two RLVDT's separated by an aluminum sheet [20]

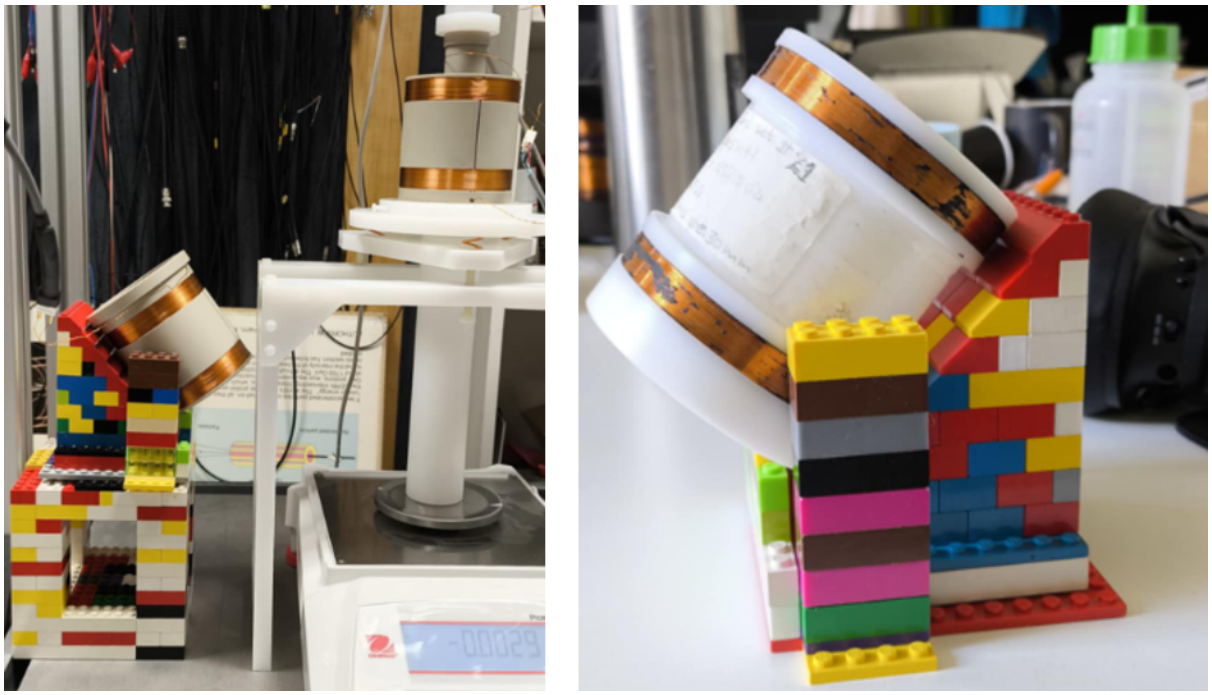

Figure 2.12: Left: two RLVDT's, one on the main suspension and one in the angle holder
Right: detailed picture of outer coils in the angle holder [20]

### 2.2.3 Input and Output

What is the in- and output of this experimental set-up? For the experiments performed in this thesis, the input is a sinusoidal voltage of a certain frequency, usually 10 kHz, but there will be a part where the frequency changes. This input signal will run through the outer coils and induce another voltage, of the same frequency, in the inner coil. This is the output. The registered signal is digitized and acquired with a sample rate high enough to measure 10 kHz waves (100 kHz). These datapoints represent, according to the theory, a sine wave. Through the datapoints, a sinefunction will be fitted:

$$x(t) = a\sin(bt + c) + d \tag{2.1}$$

where $a$ is the amplitude, $b$ is the frequency, $c$ is the phase and $d$ is the DC offset. The curvefit function will fit a sinefunction of given fixed frequency. The amplitude of that fitted sine will give the response voltage at a certain position. It is these amplitudes that the dots represent in the response curves. Figure 2.13 shows the registered datapoints with a fitted sine wave at a certain inner coil position.

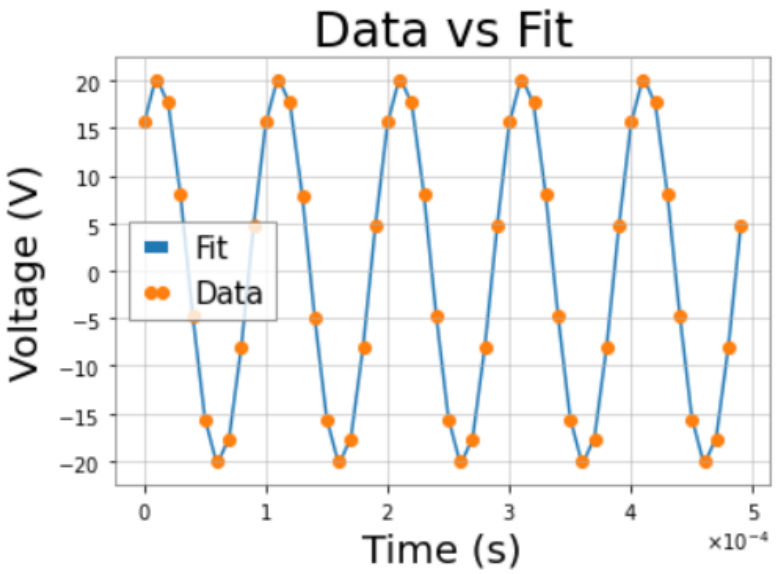


Figure 2.13: Data (orange): registered datapoints at a certain inner coil position.
Fit (blue): result of the sine wave fit function at $b$=10 kHz. The amplitude in this case is 20 V [21].

The in- and output are being monitored by the data acquisition system (DAQ) that is visible at the right panel of Figure 2.14. The top left panel of this figure shows an excitation board. The DAQ has a Digital-to-Analog converter (DAC) that translates a given number to a voltage and the excitation board sends this to the coils. The bottom left panel shows a combination board that is responsible for amplifying and reading the data from the inner coil, after which it is digitized with an Analog-to-Digital converter in the DAQ. This is also the board that controls the voice coil function. It can easily be seen that the electronics on that board is quite complex, which is why the RLVDT option is studied. The DAQ has a lot of these two boards.

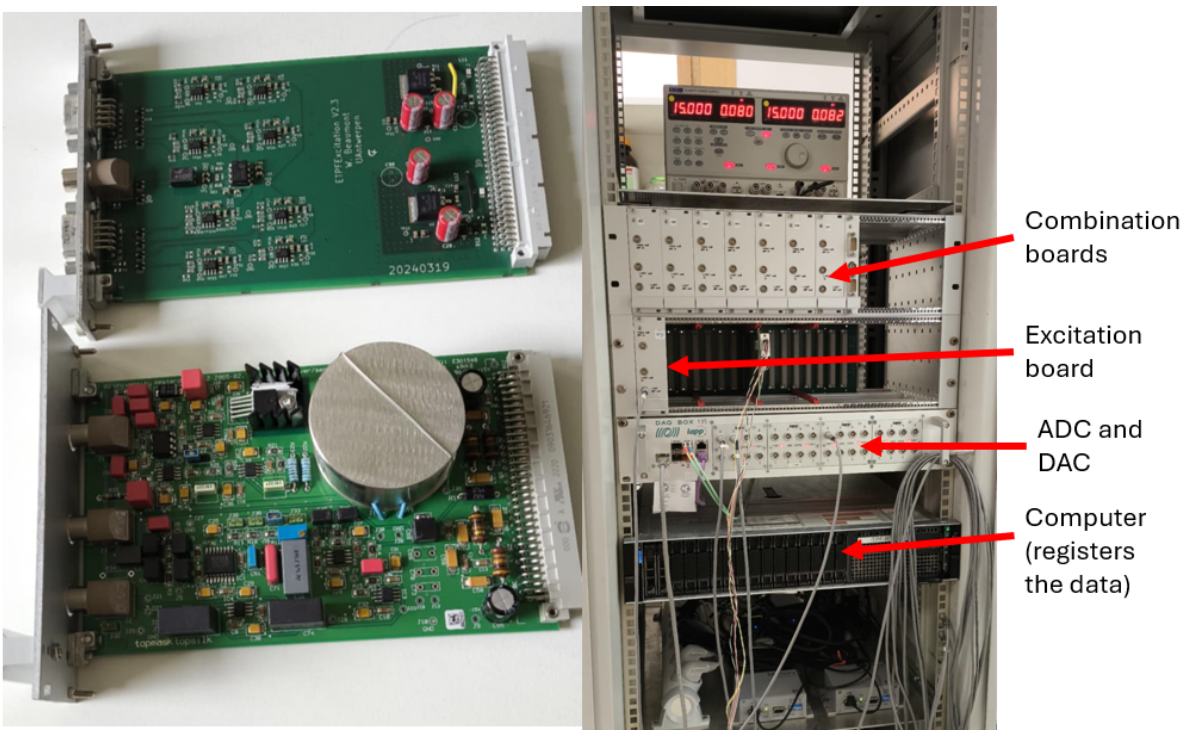


Figure 2.14: Top left: Excitation board
Bottom left: Combo-board (read-out and VC)
Right: DAQ filled with Excitation and Combination boards [20]

# 3 Simulation Results

> **"Research is what I'm doing when I don't know what I'm doing."**
> ***Wernher von Braun***

## 3.1 Excitation Frequency

In this section the relationship between sensitivity and excitation frequency is studied. On another note, when using the RLVDT, the outer coils are excited. Since the inner coil is not mounted to a steady structure and the fact that voice coils are used to move objects, it should be studied whether or not the inner coil has unwanted oscillations.

### 3.1.1 Sensitivity

The sensitivity of an LVDT (and RLVDT) is roughly determined by the slope of the response curve, which relates core displacement to output voltage. A high slope indicates greater sensitivity, meaning that even a small displacement of the core produces a significant change in output voltage. Figure 3.1 shows the current-normalized response curve and the current-normalized slopes of the response curve related to the chosen excitation frequencies.

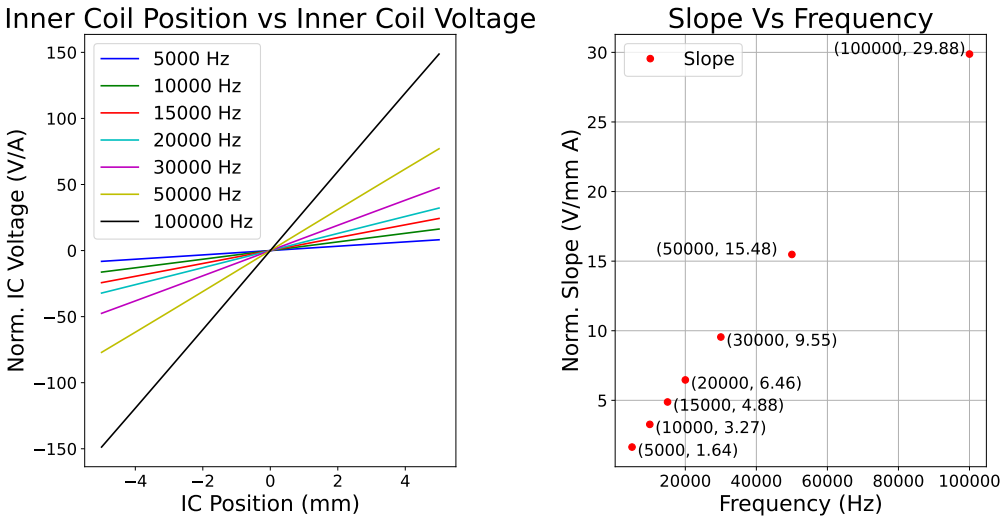


Figure 3.1: Left: Response curves, Right: Slope of the response curve [21]

Based on these results, it is more favorable to have a high frequency. Unfortunately, this is where we reach the practical limits, exciting the RLVDT with an infinitely large frequency means that we also

need an infinitely high sampling rate to read the data. The choice of 10 kHz is a conventional frequency that balances sensitivity and practical limits.

### 3.1.2 Mechanical Response

To study the mechanical response, a more theoretical approach is taken. Starting from the force generated by the voice coils

$$F_{VC}(t) = B \cdot I(t) \cdot L \tag{3.1}$$

Where $B$ is the magnetic flux density, $I(t)$ the current through the coil, which will be sinusoidal $I(t) = I_0 \sin(\omega t)$ and $L$ the length of the wire in the magnetic field. The voice coil force can therefore be written as $F_{VC}(t) = F_{VC}^0 \sin(\omega t)$. The acceleration of the inner coil $a$ is obtained using Newton's second law $a(t) = F_{VC}(t)/m$ where $m$ is the mass of the inner coil (and the mirror hanging from it). From acceleration we get the velocity by integrating:

$$v(t) = \int_0^t a(t')dt' \tag{3.2}$$

$$= \int_0^t \frac{F_{VC}^0 \sin(\omega t')}{m} dt' \tag{3.3}$$

$$= \frac{F_{VC}^0}{\omega m} \cos(\omega t) \tag{3.4}$$

From velocity we get position by integrating again

$$x(t) = \int_0^t v(t')dt' \tag{3.5}$$

$$= \int_0^t \frac{F_{VC}^0}{\omega m} \cos\big(\omega t'\big) dt' \tag{3.6}$$

$$= \frac{F_{VC}^0}{\omega^2 m} \sin(\omega t) \tag{3.7}$$

and since $\omega = 2\pi f$ with $f$ the excitation frequency:

$$x(t) = \frac{F_{VC}^0}{4\pi^2 f^2 m} \sin(2\pi f t) \tag{3.8}$$

The motion of the inner coil describes a sinusoidal oscillation with an amplitude depending on the voice coil force, the frequency and the mass [31].
Figure 3.2 shows the amplitude as a function of mass and frequency for a voice coil force of $F_{VC} = 0.05$ N. This voice coil force is a directional number that is expected (and measured) from a NIKHEF type-A LVDT [26, 31].

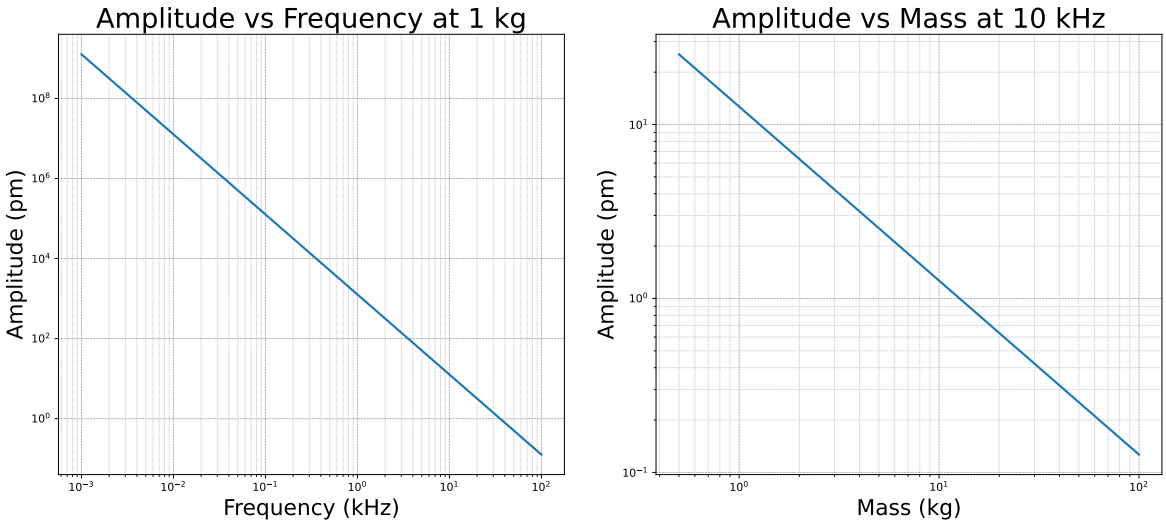


Figure 3.2: Left: Amplitude-Frequency at fixed mass of 1 kg, Right: Amplitude-Mass at fixed frequency of 10 kHz [21]

We conclude that the amplitude decreases when the excitation frequency and mass increase.
The amplitude of the oscillation at $f = 10$ kHz, a mass of $m = 1$ kg and a voice coil force of $F_{VC} = 0.05$ N is $\Delta x = 12$ pm $= 12 \cdot 10^{-12}$ m. This is within the error range of the detector. The mirrors in ETpathfinder and ET will even be around 100kg, further decreasing the oscillation amplitude.

## 3.2 Shielding

Because of the very sensitive equipment, we want to have as little external noise as possible in the sensors. The structures will have a lot of LVDT's and electronics so it is natural to ask whether or not the RLVDT's will influence each other and if they need shielding to prevent potential influences. However, we do not want the shielding itself to corrupt our data.
In this section, the influence of a cylindrical shield around the LVDT is examined. We analyze the effects on the magnetic flux density, sensitivity, and linearity for different dimensions and materials.

### 3.2.1 Magnetic Flux Density

#### Simple Planar Configuration

Before examining the exact setup, we first take a look at a simpler configuration (Figure 3.3) of just one source (height: 5 mm, thickness: 1 mm) at coordinate (0,0) and a wall at 6 mm distance from the source and a height of 60 mm. The thickness and material of the wall will vary in the simulations and we will look at the flux density at point A(25,15). This point is chosen to be off-center of the coil such that there are no symmetry elements. We compare the results to when there is no wall. This experiment was performed for both an AC source (coil) and a DC source (permanent magnet).

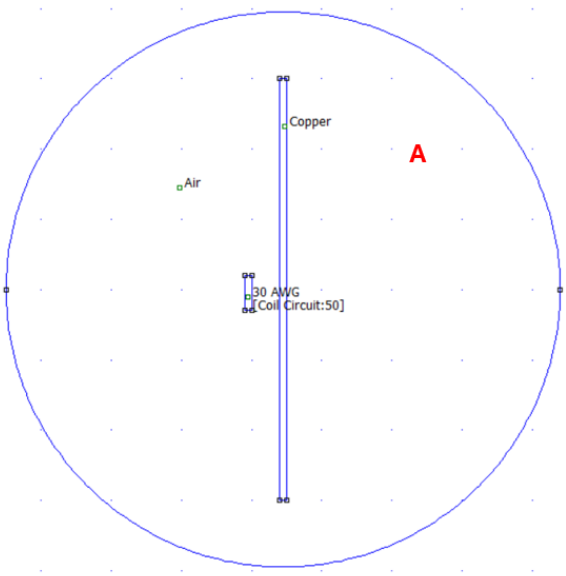


Figure 3.3: Configuration of the simple setup with the chosen point A [19]

The examined materials are Pure Iron, Copper, Aluminum and Mu-metal. The latter is a material that is specifically designed for magnetic shielding. It is a ferromagnetic alloy with a very high permeability. First, we examine the magnetic flux density and field lines for copper and mu-metal walls with thicknesses of 1 mm and 10 mm on Figure 3.4. They illustrate well the effect of material and wallthickness. These figures can also be made for aluminum, but this is similar to the ones from copper and the figures for iron are similar to the ones from mu-metal.
Starting with the AC source, a copper-wire coil (30 AWG, $N$=50), this has a current of $I = 0.02$ A and a frequency of $f = 10$ kHz.

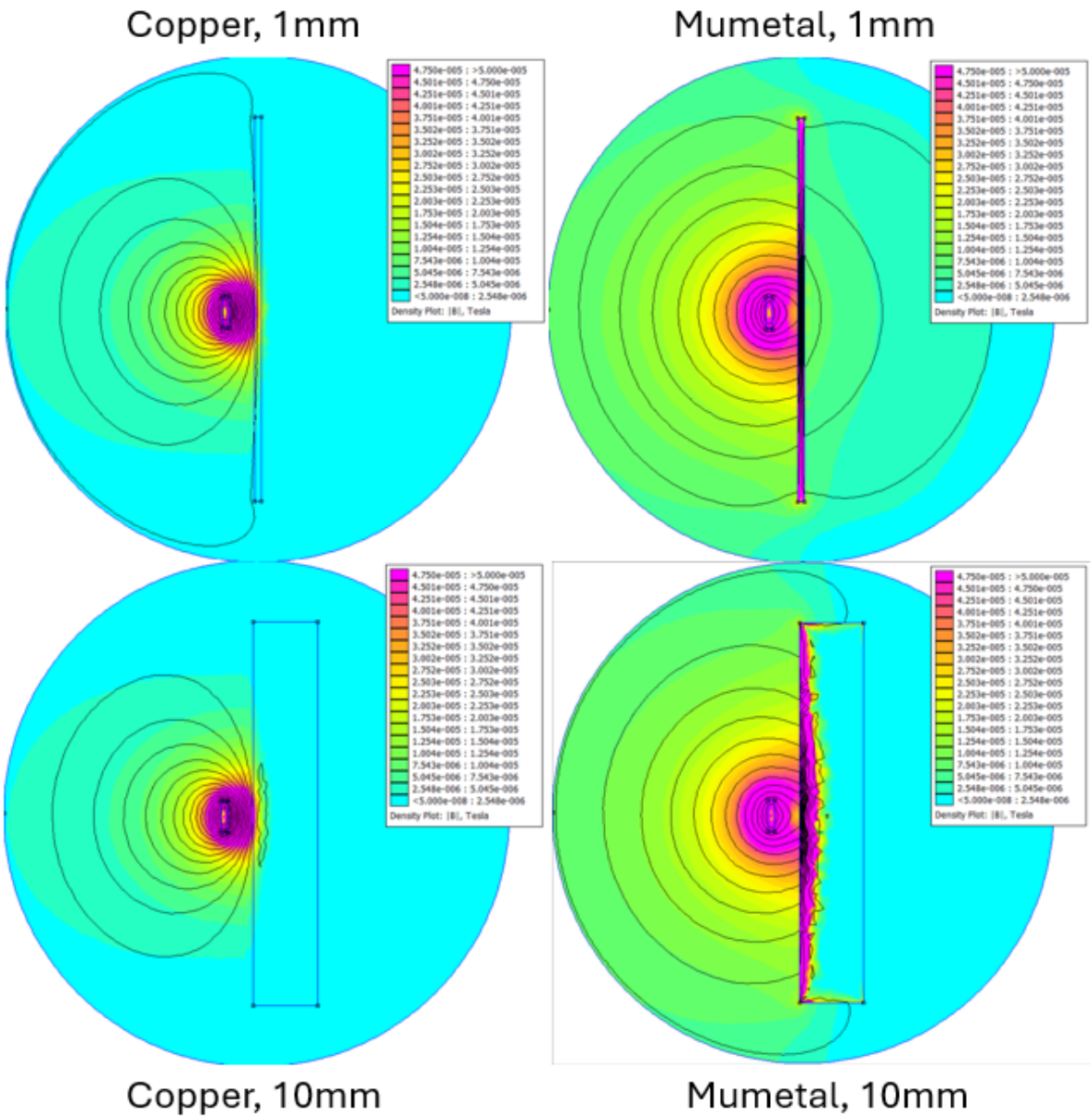


Figure 3.4: Simulated magnetic flux density and field lines (AC, 10 kHz) for copper and mu-metal barriers with thicknesses of 1 mm and 10 mm [19]

The normalisation for these four figures is the same with densities from $5 \cdot 10^{-6}$ T (blue) to $5 \cdot 10^{-5}$ T (pink).
In the top-left image, a 1 mm thick copper wall is shown. At 10 kHz, copper's high electrical conductivity induces strong eddy currents that oppose the incident magnetic field. However, due to the limited thickness, the shielding effect is modest.
The top-right image shows a 1 mm thick mu-metal wall. Although mu-metal has high magnetic permeability, it performs poorly at higher frequencies due to increased magnetic losses and limited eddy current generation. The field is only slightly reduced compared to copper of the same thickness.
In the bottom-left image, the copper wall is increased to 10 mm. The increased thickness significantly improves shielding performance, as the depth allows for more substantial eddy current generation and energy dissipation. The field behind the wall is well suppressed.
The bottom-right image shows a 10 mm thick mu-metal wall. Despite its increased thickness, the shielding performance remains poor at 10 kHz, with strong magnetic flux penetration. This highlights the

reduced effectiveness of high-permeability materials under high-frequency excitation.

We now examine the effects for a DC magnetic field, where the source is an N40 Neodymium permanent magnet. DC magnetic shielding depends on the magnetic permeability of the material. Figure 3.5 shows the magnetic flux density and field lines for copper and mu-metal barriers with thicknesses of 1 mm and 10 mm.

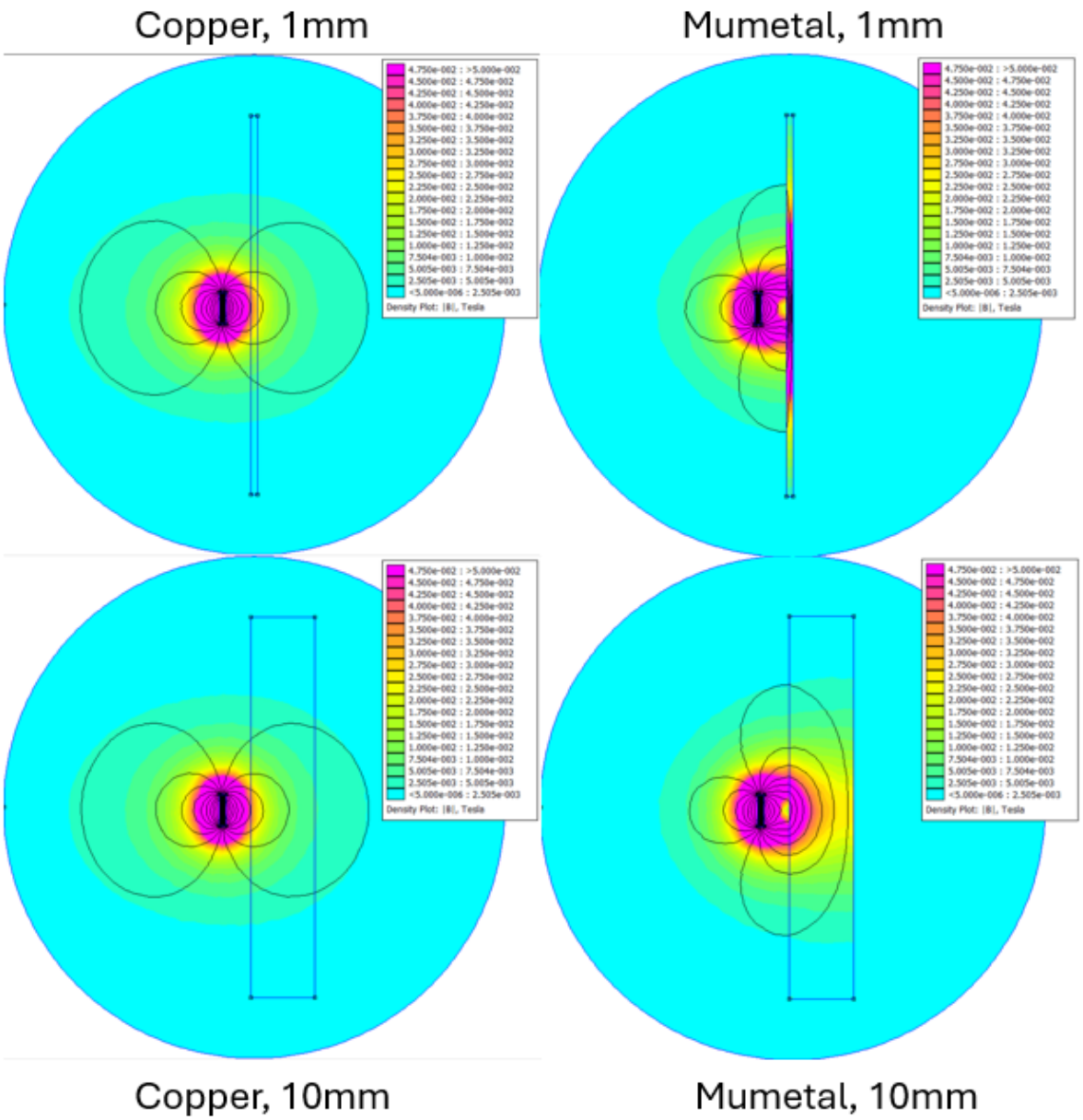


Figure 3.5: Simulated magnetic flux density and field lines (DC) for copper and mu-metal barriers with thicknesses of 1 mm and 10 mm [19]

The normalization for these four figures is the same with densities from $5 \cdot 10^{-8}$ T (blue) to $5 \cdot 10^{-2}$ T (pink).

In the top-left corner we have a 1 mm copper wall. As copper is non-ferromagnetic, the relative permeability is $\mu_r \approx 1$, it has no shielding effect, the field lines pass through it nearly unaffected. The magnetic

flux density behind the wall remains high, indicating minimal suppression.

The top-right corner has a 1 mm mu-metal wall. Unlike copper, mu-metal has an extremely high magnetic permeability, which allows it to redirect magnetic field lines effectively. Even at 1 mm thickness, it significantly reduces the field behind the wall.

In the bottom-left corner, the copper thickness increases to 10 mm. Despite the greater thickness, the shielding performance remains unchanged.

In the bottom-right corner, we have a 10 mm mu-metal wall. Here, the magnetic field is, again, concentrated within the material and almost completely excluded from the region behind it.
These results predict that mu-metal is highly effective for shielding DC fields, due to its high permeability, while copper is ineffective regardless of thickness, since DC shielding relies on redirection of magnetic flux rather than eddy current induction. On the other hand, copper will outperform mu-metal with AC shielding, given its ability to generate and conduct eddy currents more efficiently.

To quantify and verify the visually obtained AC predictions, Figure 3.6 and Figure 3.7 show the ratio of the magnetic flux density in point A with a specific wall (B) divided by the flux density in point A when there is no shield (Bn). A lower value offers the higher suppression, and are therefore better shieldings.

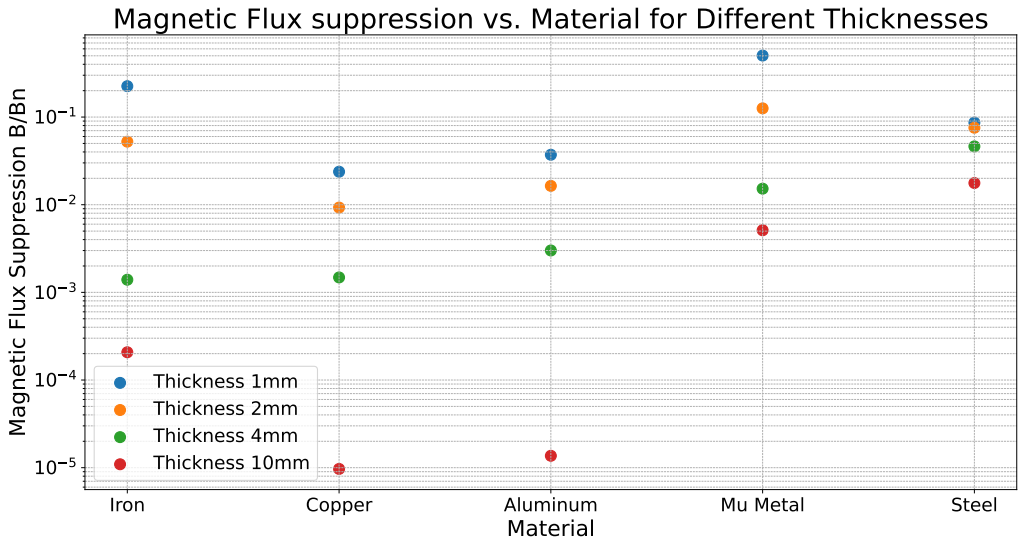


Figure 3.6: Flux density ratio vs different materials, distinguished by the thickness of the wall for the AC case [21]

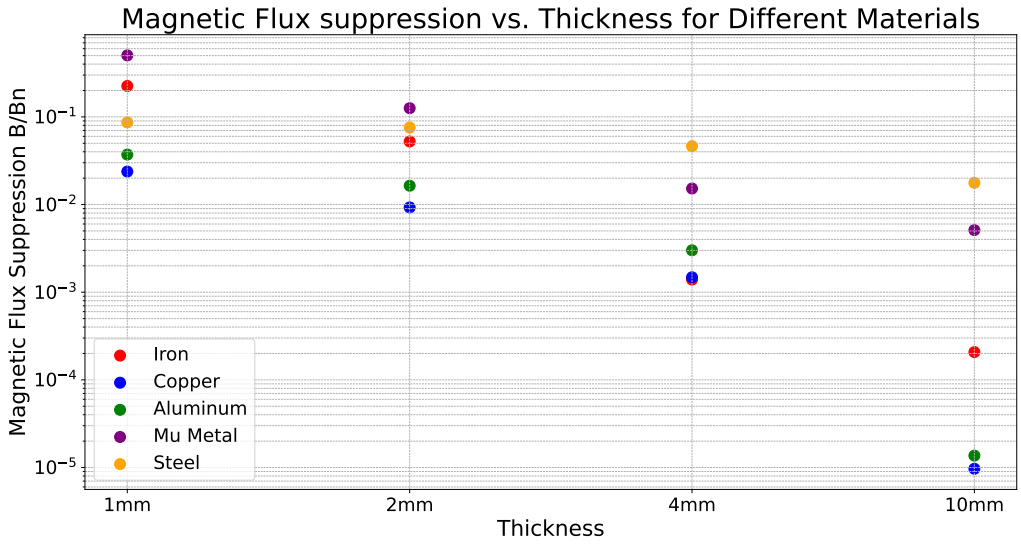


Figure 3.7: Flux density ratio vs the thickness of the wall, distinguished by material for the AC case [21]

The first observation is that thick walls suppress the flux density more than thin walls, a 1 mm copper wall suppresses the magnetic field with a factor $\approx 1.5 \cdot 10^{-2}$ while a 10 mm copper wall suppresses further up to $\approx 9 \cdot 10^{-6}$, this is $10^4$ times more efficient.
Based on these simulations, copper gives the highest suppression, followed by aluminum. Both of these are non-ferromagnetic materials. When looking at the ferromagnetic materials we see that thickness is an important property. The thickness of the wall determines which material suppresses the field more. When looking at a 1 mm wall, steel suppresses more than iron and mu-metal gives the least suppression. When looking at a 10 mm wall, both iron and mu-metal suppress more than steel. Another observation is that thickness has a less significant influence for steel than for the other materials.
For the DC source (permanent magnet) the results are shown in Figure 3.9 and Figure 3.8.

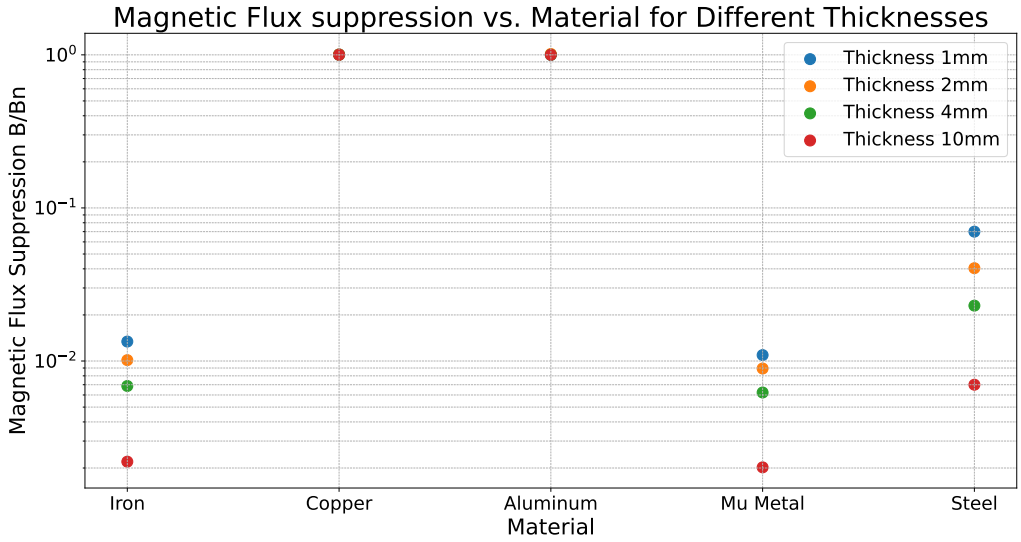


Figure 3.8: Flux density ratio vs different materials, distinguished by the thickness of the wall for the DC case [21]

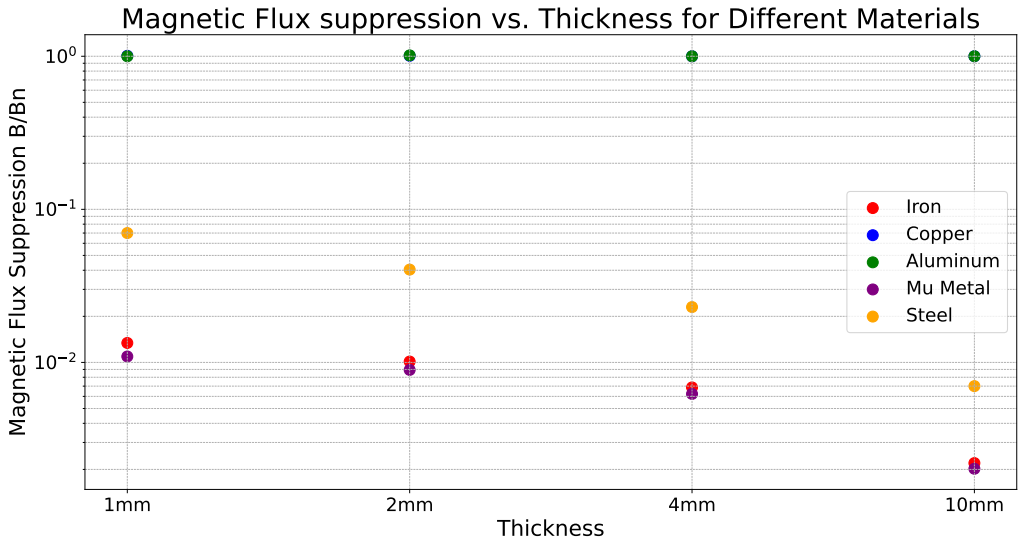


Figure 3.9: Flux density ratio vs the thickness of the wall, distinguished by material for the DC case [21]

In this case, the non-ferromagnetic materials copper and aluminum, do not give any suppression, no matter the thickness of the wall. The dots for all thicknesses of copper and aluminum at Figure 3.8 overlap, indicating that thickness is not an influence. On the other hand, mu-metal and iron perform similar, with a slight advantage for mu-metal. Also in the DC case, thicker walls are better at shielding. With a wall made from mu-metal that is 1 mm thick, we have a suppression of factor $\approx 10^{-2}$, while thickening the wall to 10 mm we can get it down to $\approx 10^{-3}$
The conclusion that can be drawn here is that a thick copper wall can be chosen if AC shieling is necessary, while DC shielding can be done with iron or mu-metal.

### Axi-symmetric Configuration

Since the 3D-properties of the RLVDT are an important factor, a similar research is done with the axially symmetric FEMM solver. However, since it is not possible to put a source next to the RLVDT (the asymmetric solver will make a ring from it), we test how well the field is kept inside shield. In other words, leakage to the outside is studied. We consider different materials and the impact of holes at the top and bottom. These holes are investigated because suspension is required in the actual setup. To incorporate the influence of the holes to the fullest, a normal LVDT is used in this part. This is because the holes will open above and below the source (inner coil), while for the RLVDT the sources (outer coils) are more enclosed by the shield, even when holes are present. The dimensions of the shield are constant (radius: $r = 60$ mm, height: $h = 80$ mm, thickness: $t = 2$ mm). The hole radii are: 0 mm, 2 mm, 10 mm, 20 mm, and the tested materials are iron and copper. The input current is $I = 0.02$ A. In Figure 3.10, the flux density is shown for the system with and without iron shield. It can be seen immediately that the flux lines of the $f = 10$ kHz AC source, are captured by the shield. The color plot clearly shows that on the outside, the magnetic field is significantly lower.

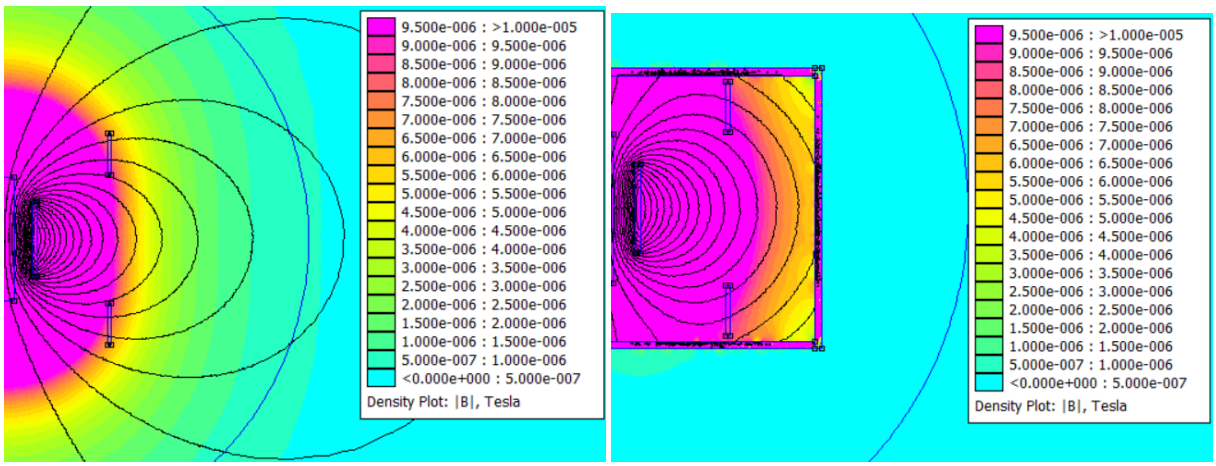


((a)) Flux density without shield ((b)) Flux density with iron shield

Figure 3.10: Magnetic flux density comparison between shield and no shield for a type-A LVDT The longitudinal distance between the shield and the outer coils is 1 mm, the radial distance is 25 mm, the longitudinal distance between the shield and the inner coil is 34 mm and the radial distance is 49 mm.[19]

The flux density for the system with a copper shield is shown in Figure 3.11. Since copper is not ferromagnetic, the flux lines do not enter the material itself but remain confined within, resulting in a different pattern of flux lines compared to the iron shield case. It can also be seen that the copper shield has significantly less magnetic flux density inside the shield than the iron shield.

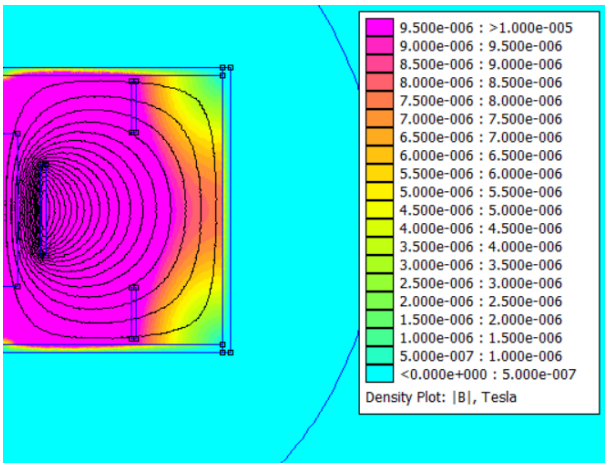


Figure 3.11: Flux density with copper shield [19]

As previously mentioned, the impact of holes in the center of the top and bottom surfaces of the cylindrical shield is examined. The field lines for this situation is shown in Figure 3.12, where it is evident that the magnetic field escapes.

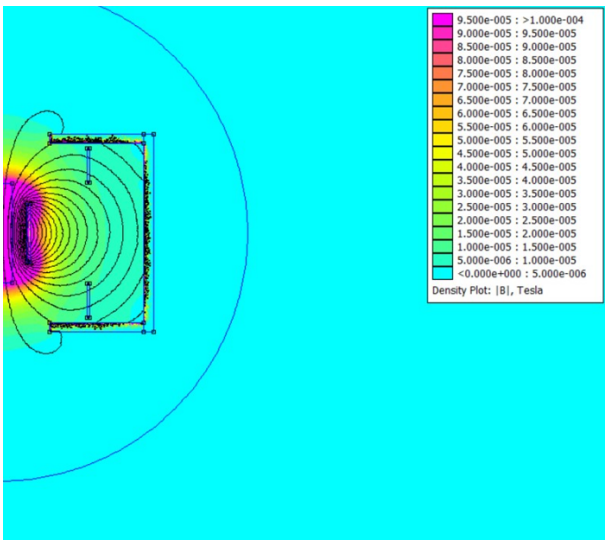


Figure 3.12: Flux density with iron shield and hole of 20 mm[19]

To further investigate how the materials and hole sizes affect the magnetic field in space, several fixed points (see Figure 3.13) are chosen where the numerically calculated flux densities are taken and divided by the density where no shield is present.

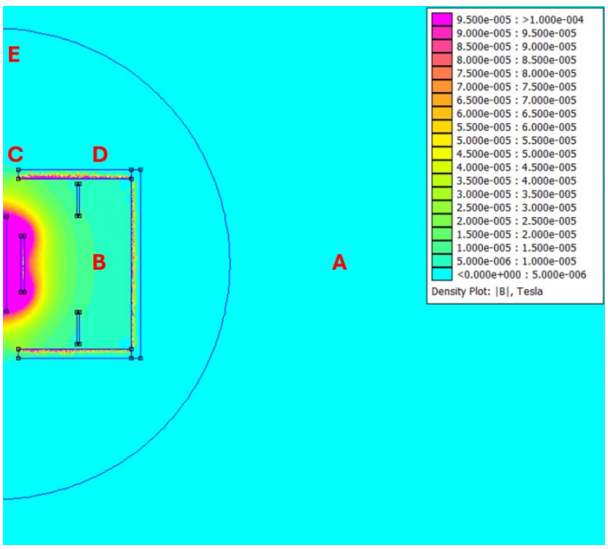


Figure 3.13: Chosen points [19]

The points are selected to provide insight into the magnetic field far outside the shield A (200,0), inside the shield B (50,0), above the hole C (5,50), close to the shield D (50,50), and far above the hole E (5,90). The flux density ratio at point B is given in Figure 3.14, the flux densities at other points are given in Figure 3.15.

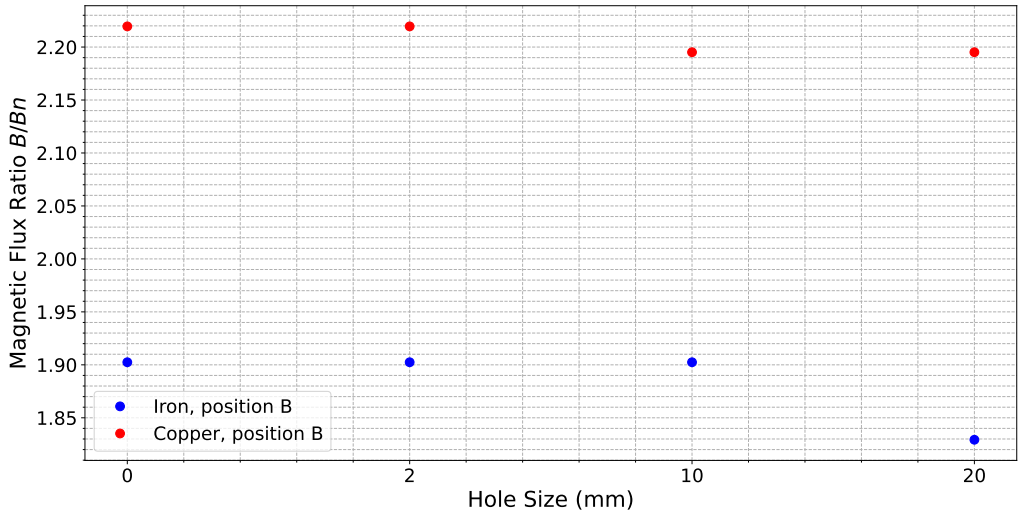


Figure 3.14: Flux Density ratio's for iron and copper with hole radii of 1 mm, 2 mm, 10 mm, 20 mm at position B [21]

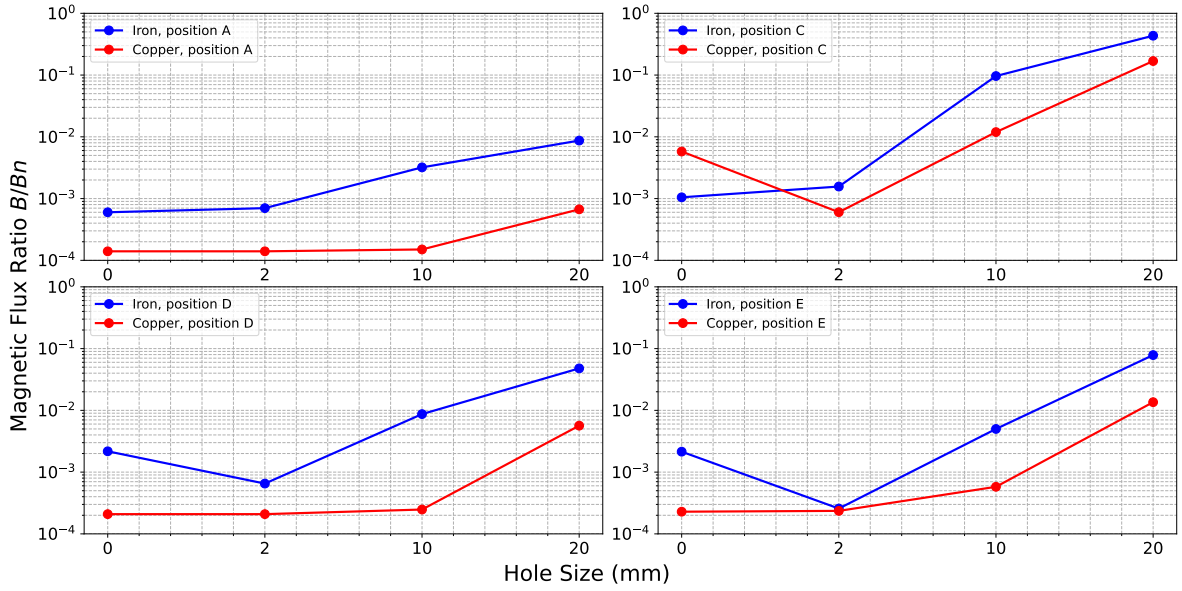


Figure 3.15: Flux Density ratio's for iron and copper with hole radii of 1 mm, 2 mm, 10 mm, 20 mm at positions A, C, D, E [21]

Following conclusions can be drawn:

- Inside the shield (point B): Magnetic flux density increases by a factor ≈2.2 for copper and ≈1.9 for iron.
- Far outside of the shield (point A): Iron suppresses the magnetic flux with a factor $2\cot 10^{-3}$ while copper gets it down with a full order of magnitude, to $2 \cdot 10^{-4}$. When a hole is present, the suppression gets less effective with almost an order of magnitude.
- Close to the shield (point D): Iron suppresses the magnetic flux with a factor $6\cot 10^{-4}$ while

copper gets it down to $1 \cdot 10^{-4}$ . When a hole is present, the suppression gets less effective with more than an order of magnitude.

- Above the hole (C, E): When the hole gets too big, field suppression is lost, with a decrease of 2 orders of magnitude.

**Conclusion**

The goal of this section was to find materials for shielding purposes. The planar configuration with a wall illustrated the behavior of field lines for the tested materials in both the DC case and a high frequency AC case. The axisymmetric solver showed again that copper is a better shielding material for a high frequency magnetic field.

### 3.2.2 Sensitivity & Linearity

This section will again work with a type-A RLVDT and the input current is $I = 0.0076$ A. Additionally, the voltages are multiplied by a factor 69 to mimic the gain factor in the electronics of the experimental setup.
Given that shielding has been shown to significantly suppress external fields, it is essential to study its impact on the measured response. Changes in sensitivity, characterized by the slope of the response curve, can be evaluated by comparing the slope obtained with a given shield configuration to that of the no-shield case. A key question is whether shielding increases, decreases, or leaves the sensitivity unaffected. If a reduction in sensitivity is observed, further investigation can be done to determine whether specific shield geometries can restore the original slope.
Another critical factor to be studied is the effect of shielding on the linearity of the RLVDT response. To quantify linearity, a small interval around the midpoint of the response curve, is fitted with a linear function. The percentage deviation from this fit is calculated as:

$$\left| \frac{\text{data} - \text{fit}}{\text{data}} \right| \cdot 100\% \tag{3.9}$$

yielding a percentage deviation.
Figure 3.16 gives a typical response curve with a linear fit over a 1 mm range around the center, such that it is surely in the linearity region. Figure 3.17 shows the linearity deviation for the no-shield case. Deviations remain below 1% within $\pm 5$ mm of the center. In reality, the inner coil will not move that far. The objective is thus to determine whether shielding preserves this linearity and, if not, what shield configurations can recover or approximate the unshielded RLVDT response.

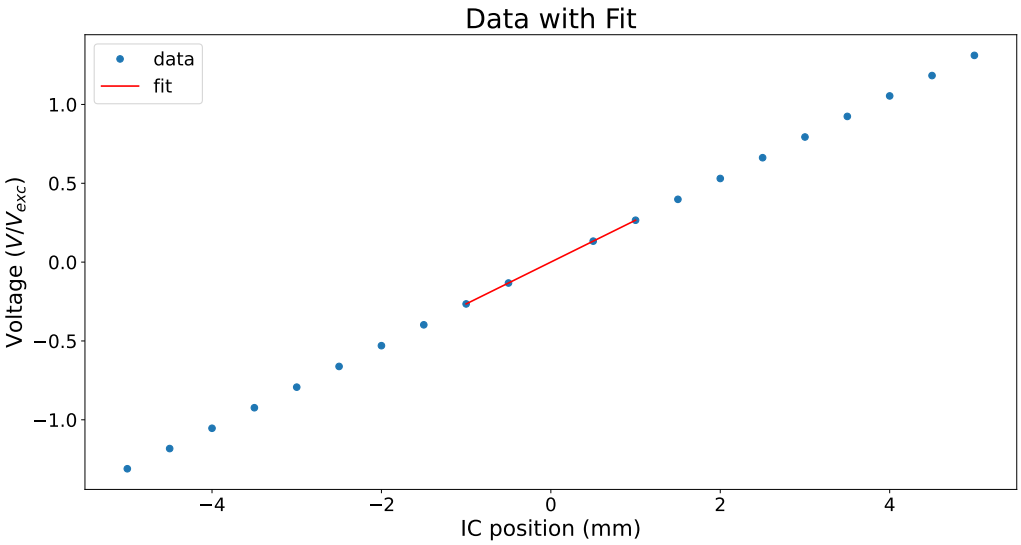


Figure 3.16: Response Data with linear fit $\pm 1$ mm round the center point [21]

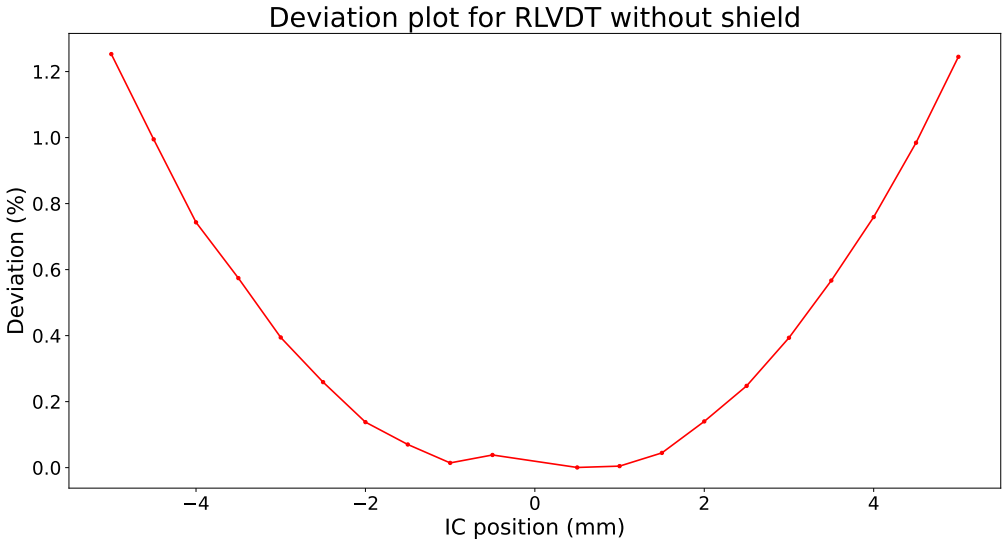


Figure 3.17: Linearity deviation for the case without shield [21]

The default shield configuration used in this study is as follows:

- Material: Copper
- Radius: 42 mm
- Height: 80 mm
- Thickness: 2 mm
- Hole: 0 mm
- Radial distance to coil: 4 mm

- Longitudinal distance to coil: 4 mm

In further paragraphs, the parameters are varied independently while keeping all others fixed.

### Material

The first shielding parameter that will be tested is the material. Similar to the magnetic flux suppression experiment for the simple case, we look at copper, iron, aluminum, mu-metal and steel. Figure 3.18, 3.19 and 3.20 show a response plot, a linearity deviation plot and the slope-ratio of these materials to the no-shield case. Figure 3.19 and 3.20 are the same figures where respectively iron, and mu-metal are removed to increase visibility in the linearity for the other materials.

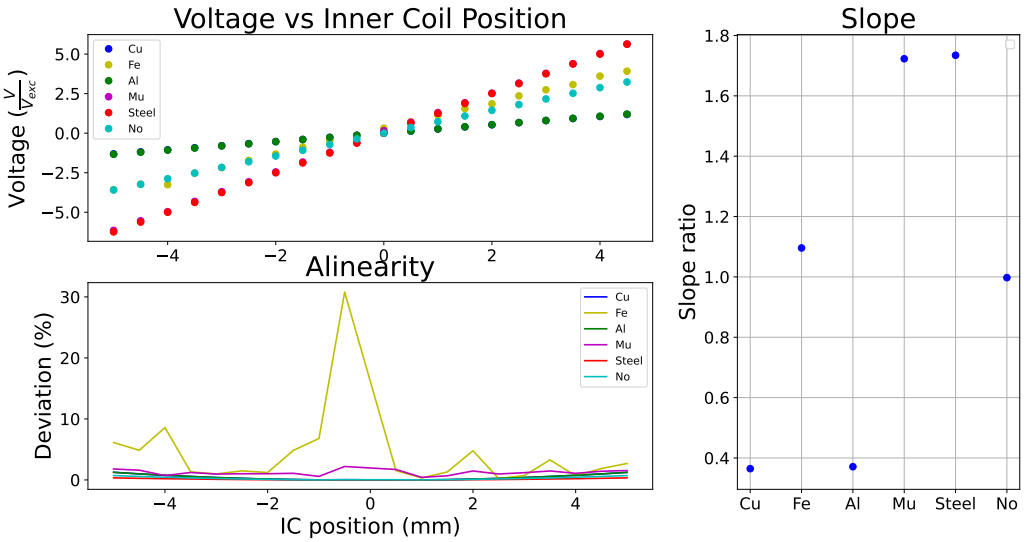


Figure 3.18: Top Left: Response normalized by excitation voltage
Bottom Left: Linearity deviation
Right: ratio of the slopes of the response plots with and without shield [21]

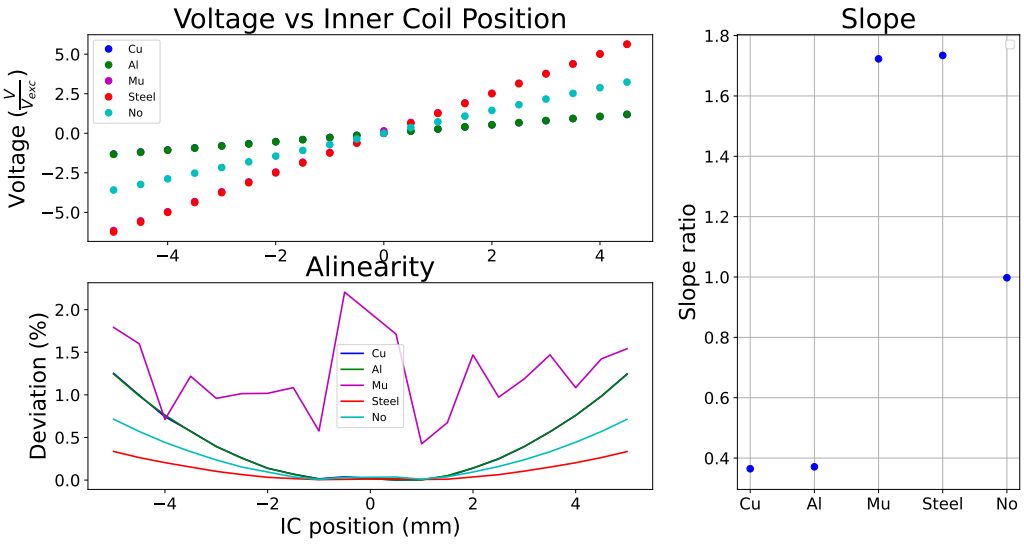


Figure 3.19: Top Left: Response normalized by excitation voltage
Bottom Left: Linearity deviation
Right: ratio of the slopes of the response plots with and without shield (without iron) [21]

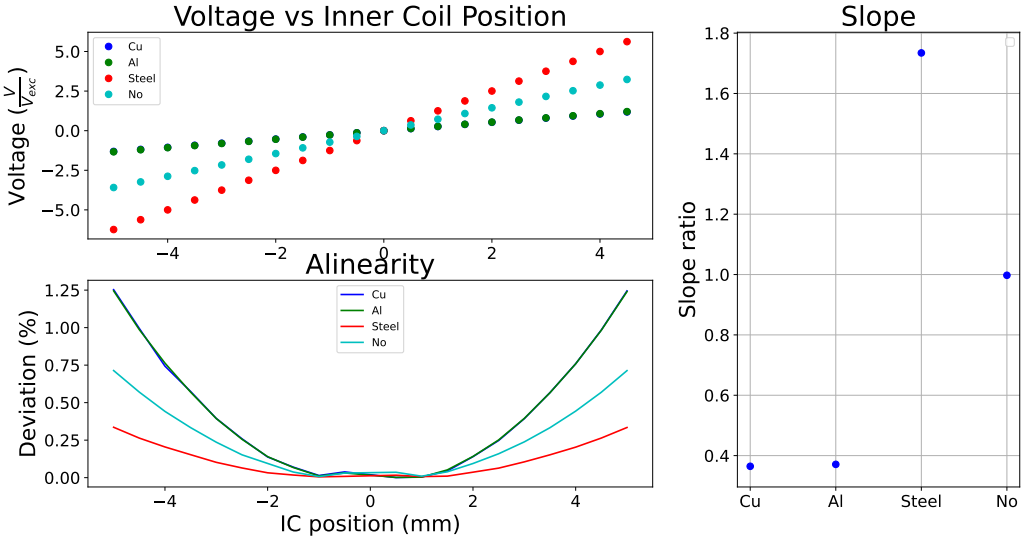


Figure 3.20: Top Left: Response normalized by excitation voltage
Bottom Left: Linearity deviation
Right: ratio of the slopes of the response plots with and without shield (without iron and mu-metal) [21]

Based on the high linearity deviation of iron and mu-metal we can exclude the use of these materials. They do have a higher slope and therefore increase the sensitivity but the linearity property has more impact. For aluminum and copper, the deviation increases but the shape of the graph stays the same. Nevertheless, a deviation less than 1.5% is still manageable. Unfortunately, the slope decreases with a factor $\approx 2.5$, which means that the implementation of an aluminum or copper shield with these geometries reduces the sensitivity. A shield made from stainless steel would reduce the linearity deviation and

increase the sensitivity, both of these aspects are favorable, however it is not the best shielding material, as seen before.
The bad linearity of the iron shield can be explained by a high fluctuation in magnetic flux density and eddy current density inside the shield. Figure 3.21 and Figure 3.22 show respectively the magnetic flux density and eddy current density inside an iron shield of 2 mm, along the contour defined in Figure 2.5. The same plots for a copper shield of 2 mm are added to visually compare the effects of the two different materials.

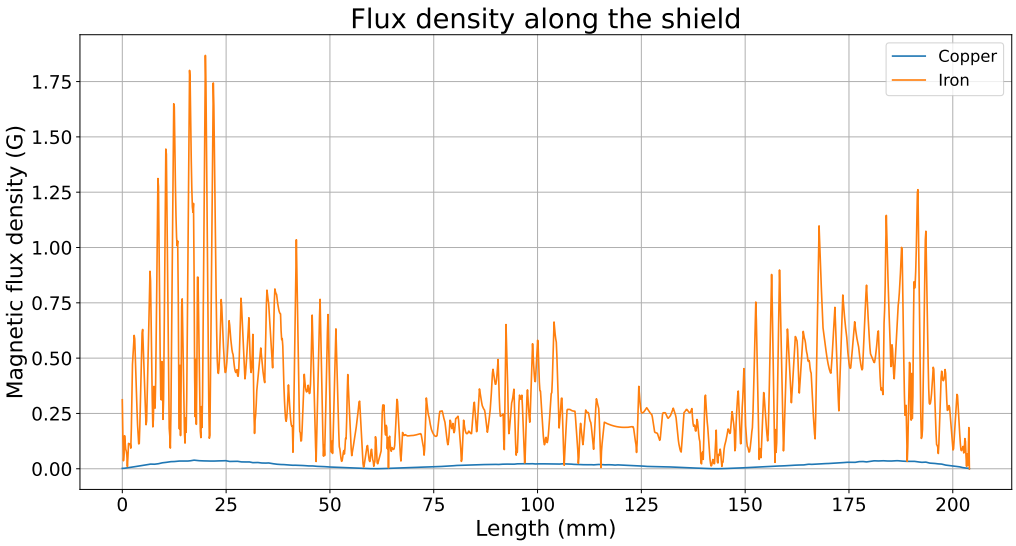


Figure 3.21: Magnetic flux density inside an iron and copper shield of 2 mm thickness [21]

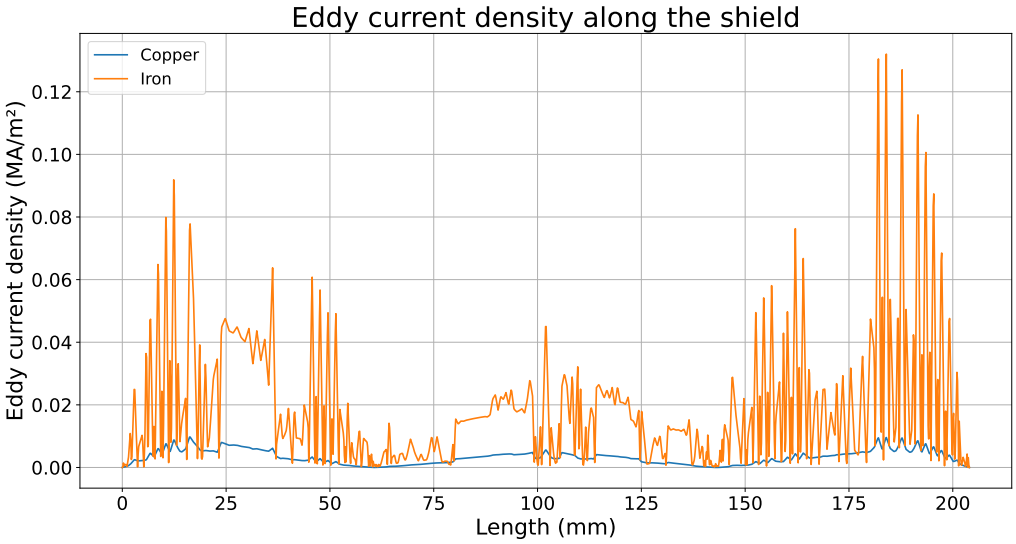


Figure 3.22: Eddy current density inside and iron and copper shield of 2 mm thickness [21]

### Thickness

In previous simulations it has been made clear that thickness plays a role in shielding efficiency, therefore it is necessary to determine how thickness influences the working of the RLVDT. Figure 3.23

shows the response, linearity deviation and slope-ratio for different thicknesses of the shield, where the distance between the coils and the shield had been kept the same.

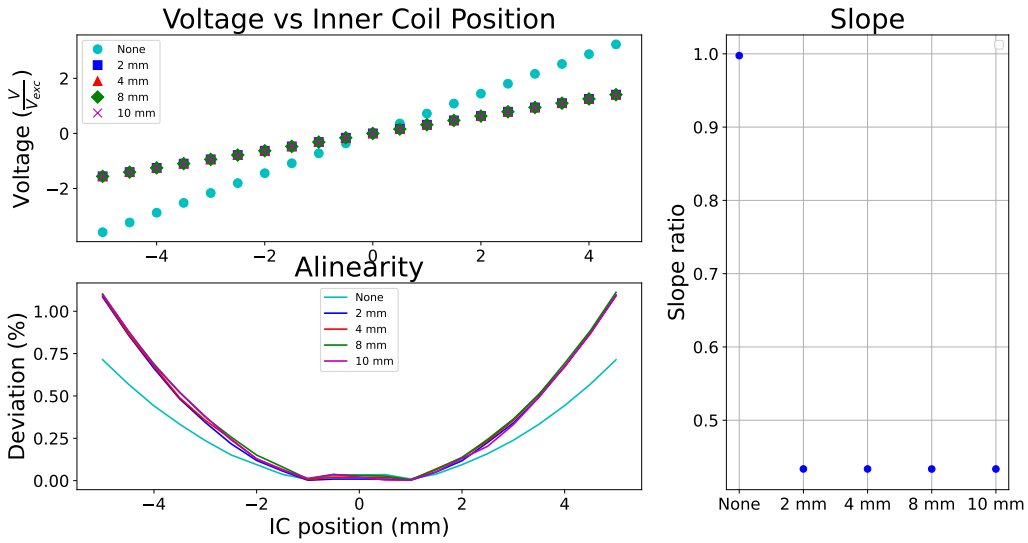


Figure 3.23: Thicknesses: 2 mm, 4 mm, 8 mm, 10 mm
Top Left: Response normalized by excitation voltage
Bottom Left: Linearity deviation
Right: ratio of the slopes of the response plots with and without copper shield [21]

It can be clearly seen that thickness has minimal influence on the data. Theoretically, increasing the thickness of a plate would increase the eddy current generation, because there is more space to develop them, but this is only true for thicknesses smaller than the skin depth $\delta$. When the thickness of a material exceeds the skin depth, further increasing the thickness has no effect. The skin depth of copper is only $\approx 66\ \mu$m, so smaller than the thickness of the thinnest implemented shield.

### Size

In this section, the size of the shield will be varied, both height and radius of the shield will change, and therefore also the distance between the coils and the shield. The different sizes tested are the default configuration where both radius and height is increased with 5 mm, 10 mm, 20 mm and 30 mm. Results are shown in Figure 3.24

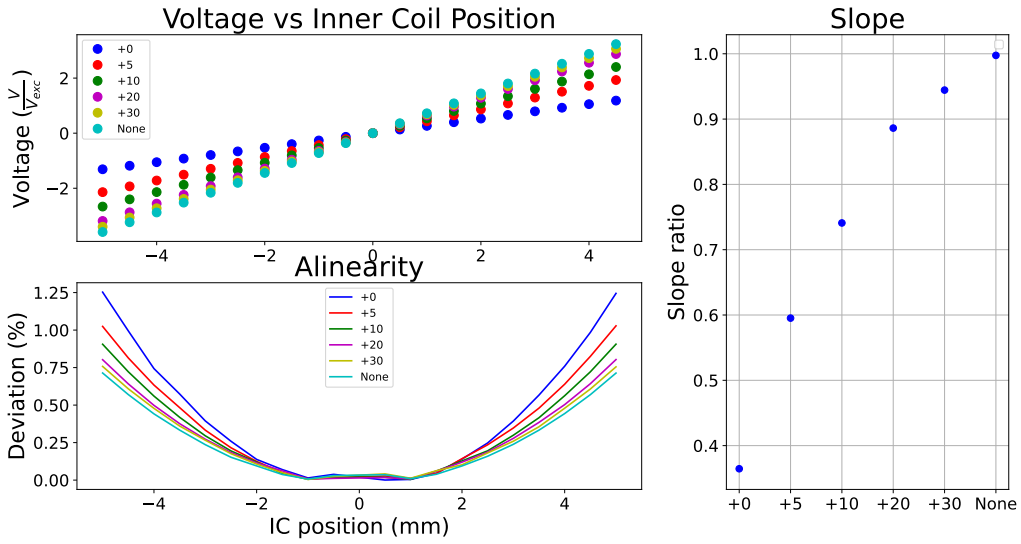


Figure 3.24: Increments: +0, +5 mm, +10 mm, +20 mm, +30 mm
Top Left: Response normalized by excitation voltage
Bottom Left: Linearity deviation
Right: ratio of the slopes of the response plots with and without copper shield [21]

The linearity and sensitivity are getting restored when the shield gets bigger, and the distance to the coil becomes larger. The generated eddy currents have a limited range and we see that the influence dies out far from the metal shield.

### Hole

As mentioned before, the shield and the RLVDT itself need to be suspended, preventing us from closing the shield entirely. This paragraph will study the influence of a hole on the RLVDT response. Figure 3.25 displays the simulated results.

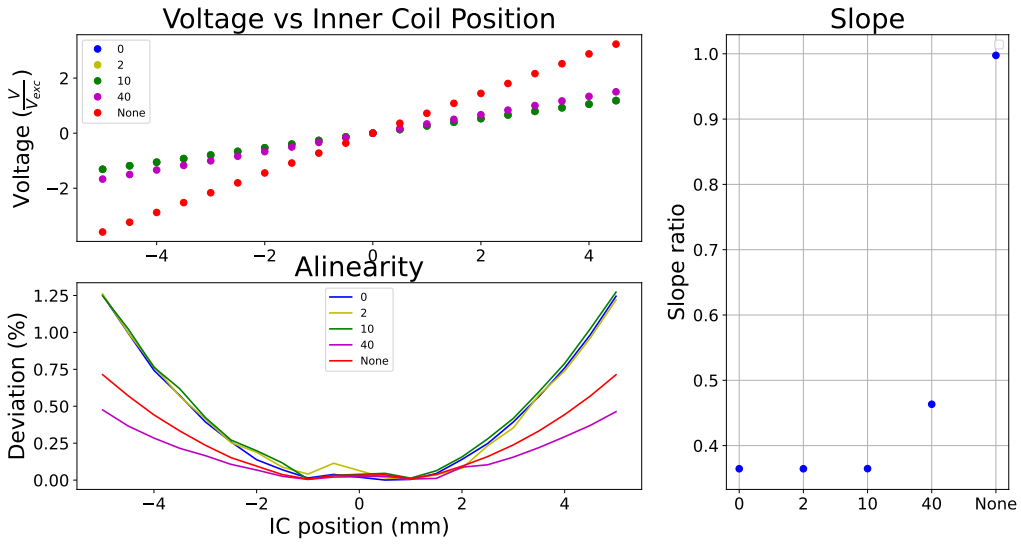


Figure 3.25: Hole radii: 0 mm, 2 mm, 10 mm, 40 mm
Top Left: Response normalized by excitation voltage
Bottom Left: Linearity deviation
Right: ratio of the slopes of the response plots with and without copper shield [21]

For hole radii of 0 mm, 2 mm and 10 mm there is no significant change. Working with the RLVDT means that the outer coils are getting excited. Since the outer coils themselves are at a radius of 35 mm, the absence of a shield around $r = 10$ mm appears to have no measurable effect. For a hole of 40 mm, there is no copper above the coils. The outer coils will not induce eddy currents in the top and bottom parts of the cylinder. There is less linearity deviation, even less than when there is no shield and the slope gets partially restored. This raises the question if only a cylindrical shell without top- and bottom part would function well enough as a shield.

### Multiple shields

Since iron is a good shielding material for DC magnetic fields, and copper for high frequency AC field, and we would like to shield our RLVDT from any kind of disturbances, we can look into a double shield where the inner shield is made from copper and the outer shield from iron. The question is if the iron shield will still disturb the linearity, or that the copper shield protects the data from the influence that iron has shown to give. Figure 3.26 shows the impact of an iron shield of 2 mm thickness at a distance of 0 mm ($\approx 0.1$ $\mu$m), 2 mm and 20 mm from the default copper shield (in height and radius).

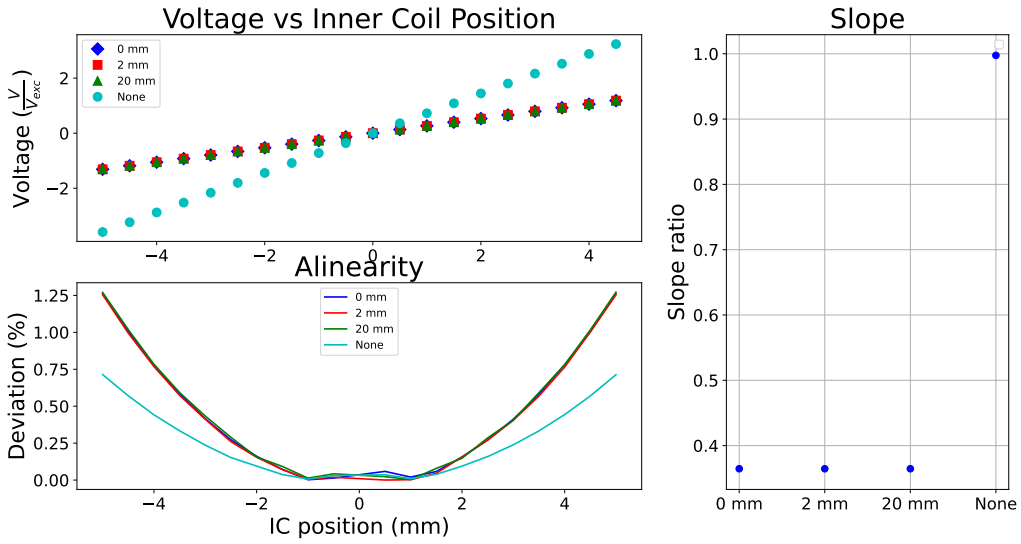


Figure 3.26: Two-shield distance: 0 mm, 2 mm, 20 mm
Top Left: Response normalized by excitation voltage
Bottom Left: Linearity deviation
Right: ratio of the slopes of the response plots with and without copper and iron shields [21]

As demonstrated in the figure, the presence of a copper shield effectively isolates the system from disturbances caused by an adjacent iron shield, even at minimal separation distances. Based these findings, it will be interesting to explore whether a three-shield configuration could offer further improvements, where the inner shield is made from stainless steel, the second shield from copper and the outer shield from iron. A shield made from steel would improve the sensitivity and have less linearity deviation. While it did not score well on the shielding part itself, it can serve as a shield for the negative influence a copper shield has on the RLVDT response (decreased slope and a slightly higher linearity deviation). This copper shield would however have the critical role in AC shielding. The outer shield, made from iron then serves as a shield against DC fields.
This three-layered approach is appealing because it combines the different electromagnetic properties of each material in a complementary manner to theoretically achieve superior shielding performance compared to no, single- or two-shield alternatives. However, multiple shield configurations are more difficult to construct and practically implement them in the set-ups.

Figure 3.28 Shows the comparison of this triple shield to the no-shield case, Figure 3.27 illustrates the configuration in FEMM and the solution with the flux density and field lines.

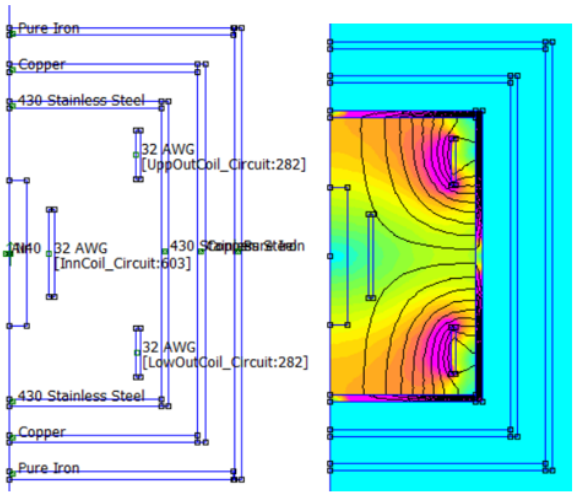


Figure 3.27: Left: configuration in FEMM
Right: Solution with flux density and field lines
The inner shield made from stainless steel has the geometry of the default copper shield, the middle shield has a radial and longitudinal distance of 10 mm to the inner shield and the outer shield has a radial and longitudinal distance of 10 mm to the middle shield. [19]

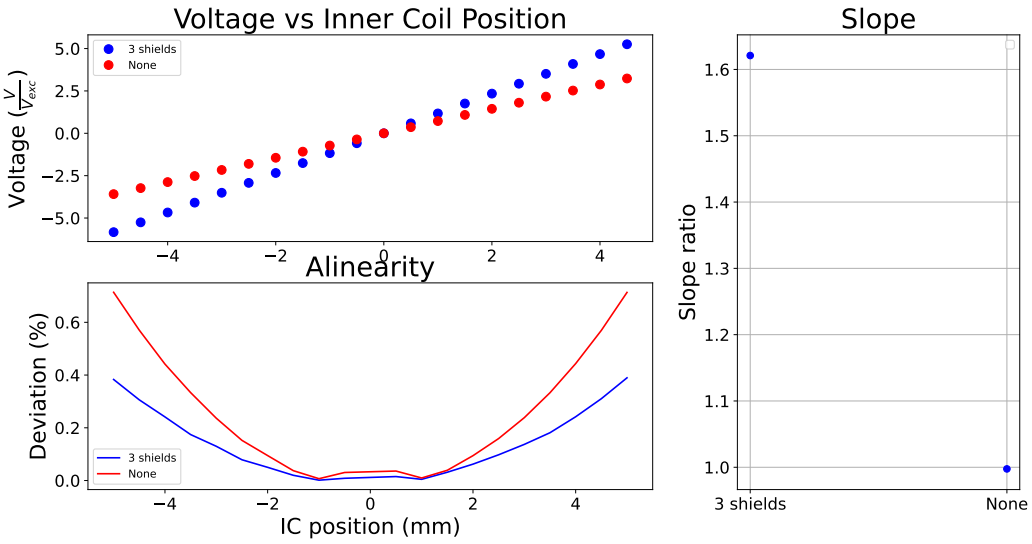


Figure 3.28: triple shield vs no shield
Top Left: Response normalized by excitation voltage
Bottom Left: Linearity deviation
Right: ratio of the slopes of the response plots with and without 3 shields [21]

We see that, when using an inner shield of stainless steel, the sensitivity increases and the linearity deviation decreases. Now the question rises if this configuration is also performing well at suppressing the magnetic flux. Figure 3.29 shows the FEMM solution for the DC and AC magnetism case, Figure 3.30 gives the quantified data, a suppression ratio for the single shield case (iron for DC, copper for AC), the two-shield configuration (copper and iron) and the three-shield configuration (stainless steel, copper, iron) to the no-shield case. As expected, adding more layers of shielding material will further suppress the magnetic field and no unwanted effects are taking place.

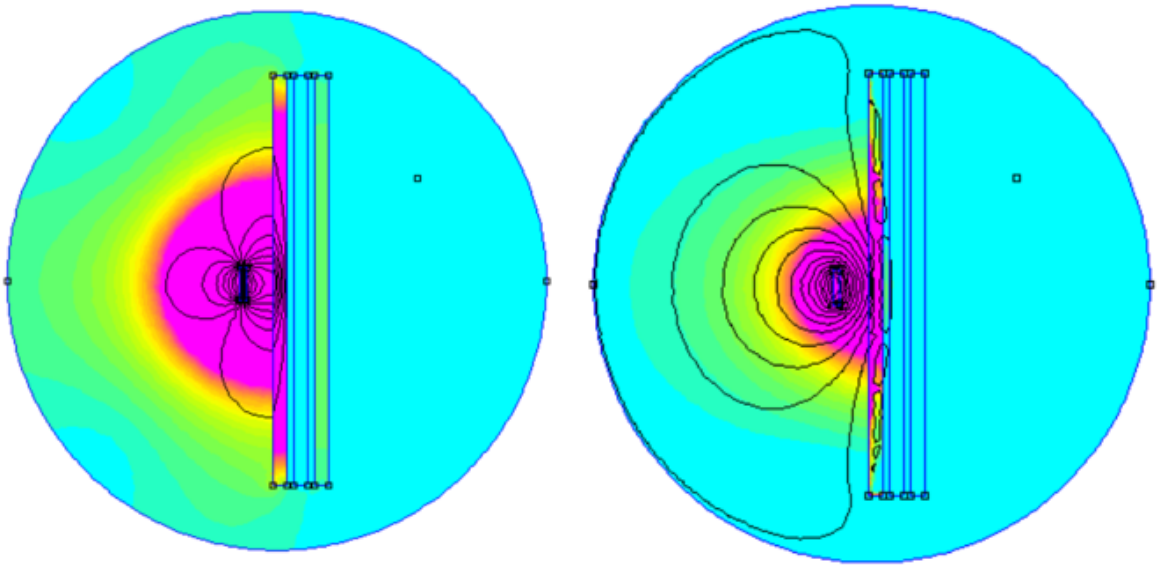

Figure 3.29: Left: Flux density and field lines in presence of a permanent magnet (DC)
Right: Flux density and field lines in presence of coil (AC)
From left to right: iron, copper, steel, 2 mm thickness [19]

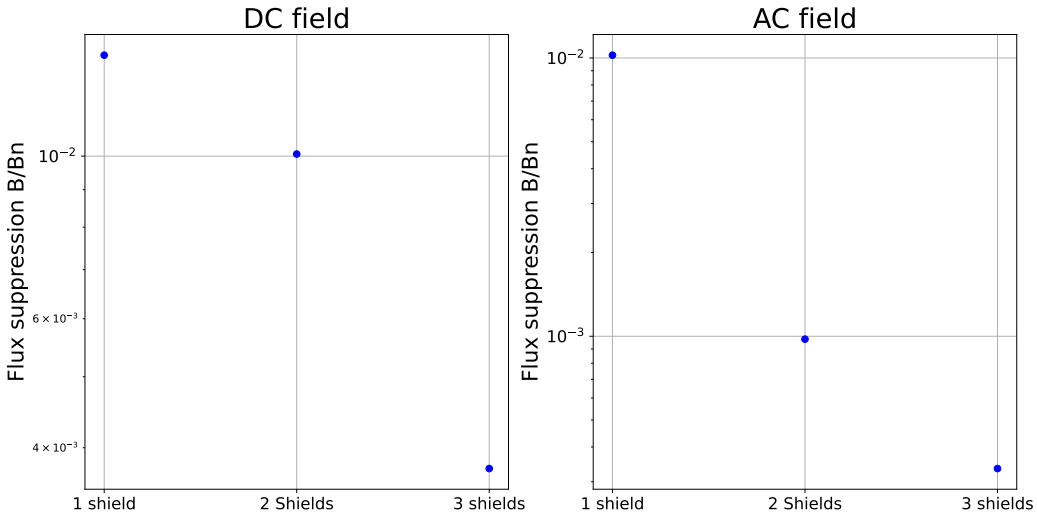


Figure 3.30: Ratio of 1 shield (iron), 2 shields (iron, copper), 3 shields (iron, copper, steel) to the no-shield case for DC (Left) and AC (Right) [21]

### 3.2.3 Shielding Options in ETpathfinder

Naturally, fabricating the ideal shield is not possible, there are always practical limits that will restrict us from implementing the perfect shield. The main problem would be suspension and its physical, mechanical restrictions. Figure 3.31 and Figure 3.32 are schematic representations of one of the current LVDT suspensions used in ETpathfinder. Based on this, we could think of a practically implementable shield.

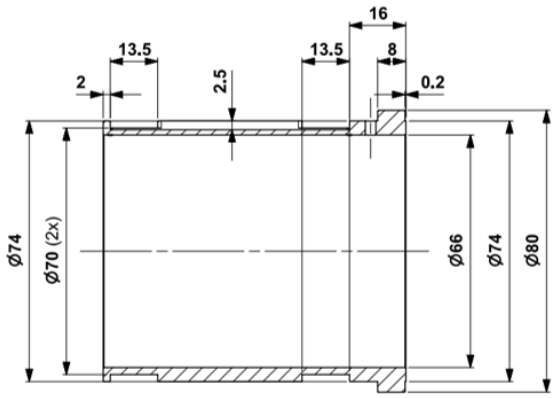


Figure 3.31: Schematic representation of the side view of the bobbin for the outer coils [38]

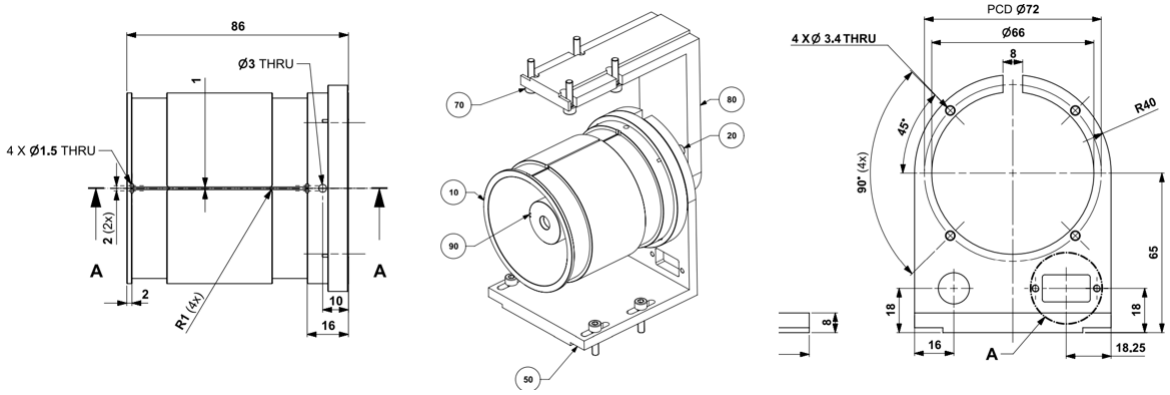


Figure 3.32: Left: Schematic representation of the bobbin's side view
Middle: Schematic representation of the LVDT with suspension
Right: Schematic representation of the suspension panel of the outer coil bobbin [38]

Based on these drawings we could estimate dimensions for a practical shield and explore limitations. We have already seen that, when using a single 2 mm copper shield, a big shield would be better for the sensitivity and linearity. Unfortunately, the middle drawing of Figure 3.32 shows that the radius has a limit since there is a panel above and below the bobbin. This means that the maximal radius can be 53 mm, which is only at 20 mm distance from the outer coil. Looking at Figure 3.24, this would yield a slope ratio of $\approx 0.9$ and a linearity deviation of 0.1% compared to the no-shield configuration. Given that the bobbin itself is 86 mm, the height could be made 90 mm. However, the back panel of the bobbin suspension doesn't allow to close the shield. Figure 3.25 shows that this is favorable for the data, but again raising the question if the shielding purpose is fulfilled. One can also look at the option of closing the shield at the left, but leaving the right part open, or closing it behind the bobbin. But this has shown to be disastrous, especially for the linearity, as Figure 3.33 shows different distances of the bottom panel to the cylinder.

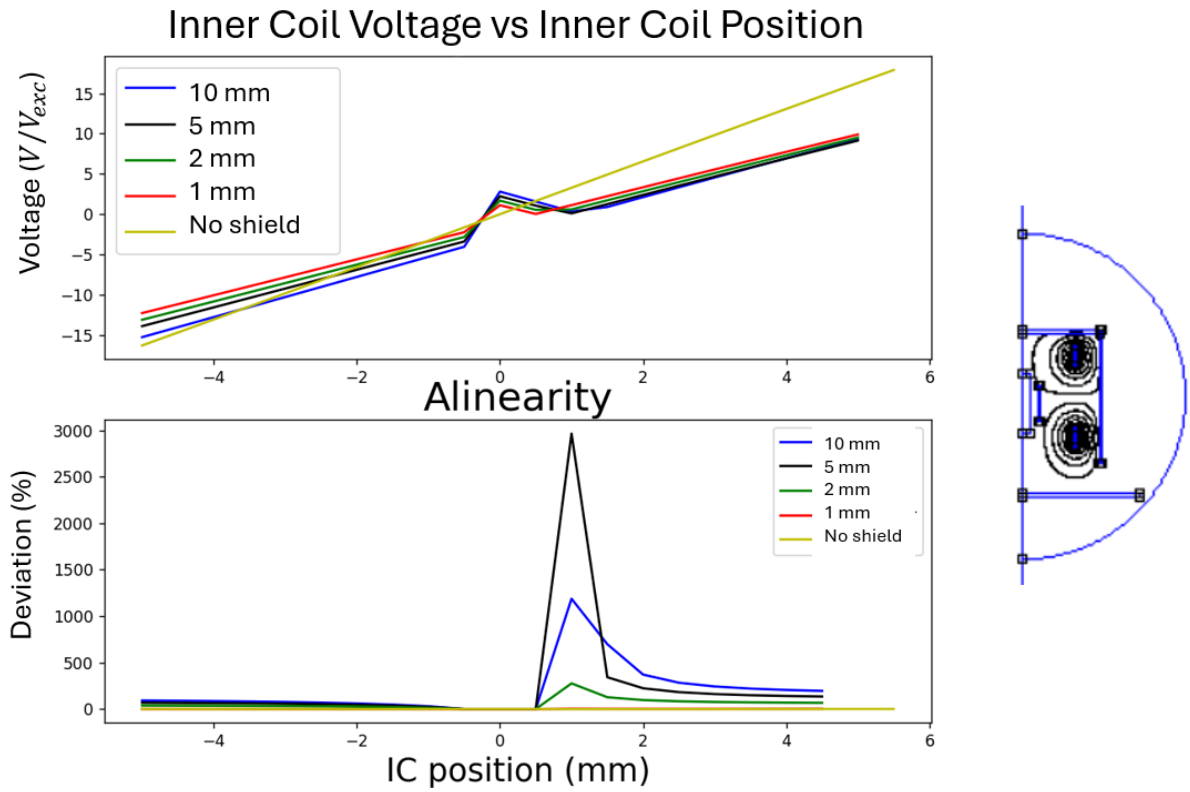


Figure 3.33: Distances: 10 mm, 5 mm, 2 mm, 1 mm
Top Left: Response normalized by excitation voltage
Bottom Left: Linearity deviation [21]
Right: FEMM configuration for distance of 10 mm [19]

The main conclusion to be drawn from this section is that the current models for LVDT suspension are not perfect for implementing a shield. Research has to be done to optimize the design set-up of the LVDT suspension in case shielding will be necessary. From the research of the multiple shields can be concluded that it does not matter how close the shields are to each other, so this will not give any limitations or restrictions, yet fabrication and suspension might be difficult.

### 3.2.4 Influence of an External RLVDT

In this section, planar simulations will be performed in FEMM to study the pick-up signal of the inner coil of an RLVDT (main) when the outer coils of a second RLVDT (side) are getting excited. Afterwards, a shield for both RLVDT's gets added to study if the influence can be suppressed. A second thing to be studied is the induced voltage when the side RLVDT is rotated over different angles.

#### Parallel RLVDT's

Figure 3.34 shows the configuration in FEMM where both RLVDT's have a shield, the induced voltage of the main RLVDT inner coil gets read out at vertical positions between -5 mm and 5 mm. The distance between the centers of the RLVDT's is 150 mm. To simulate the real experiment, all data is multiplied by the electronic gain factor $g = 69$ and the input current is $I = 0.0076$ A, this is equivalent to the experiment where a voltage of 2.38 V is given to the outer coils and where the inner coil has an impedance of $Z = 311.8\ \Omega$.
Figure 3.35 gives the induced voltage of the inner coil of the main RLVDT when the outer coils of a

secondary RLVDT are excited, with and without implementation of both shields. The outer coils of the main RLVDT are not excited yet. Figure 3.36 shows the induced voltage of the configuration with shield to gain a better visibility.

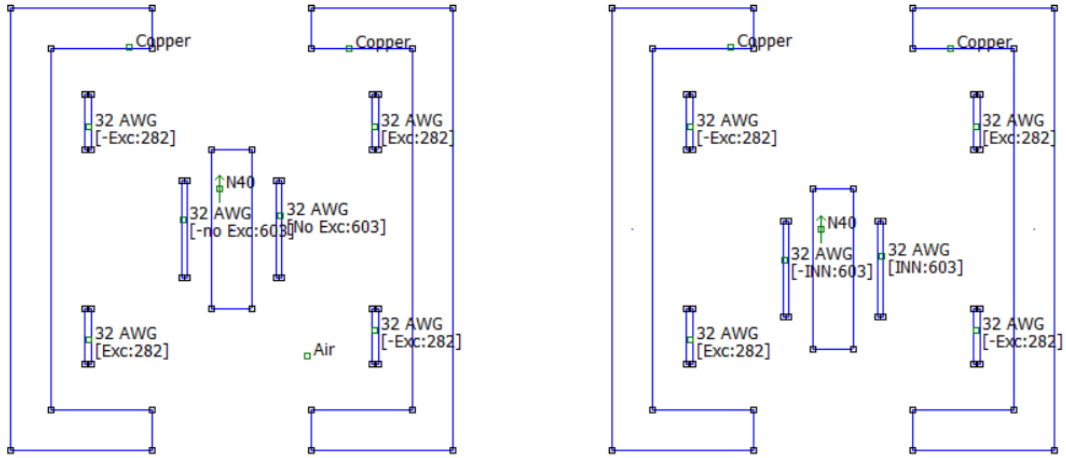


Figure 3.34: FEMM configuration of two RLVDT's, separated with a center-to-center distance of 150 mm with copper shields of 10 mm thickness [19]

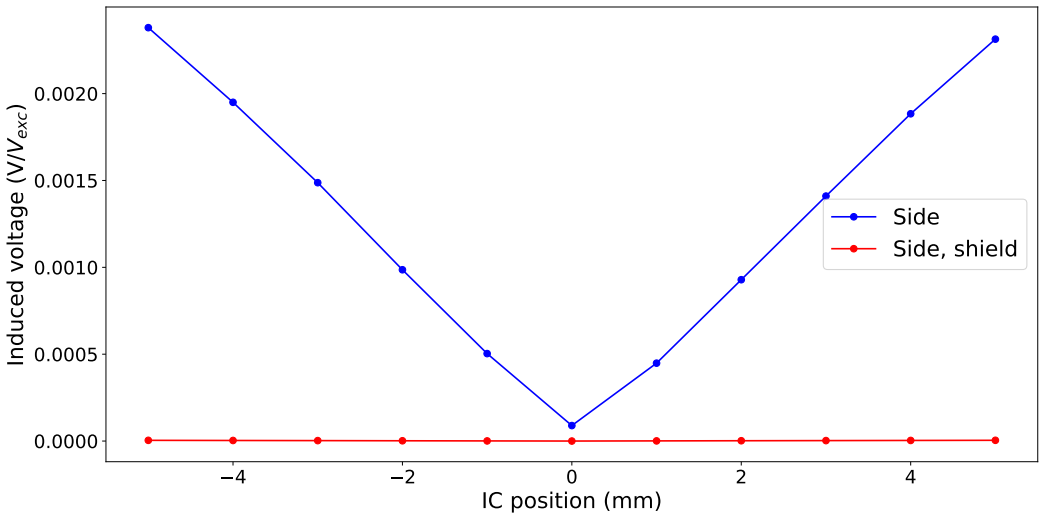


Figure 3.35: Induced voltage in the inner coil of the (not excited) main RLVDT when a side RLVDT has excited outer coils, with and without the presence of a shield. The center-to-center distance is 150 mm. The signal is normalized to excitation voltage [21].

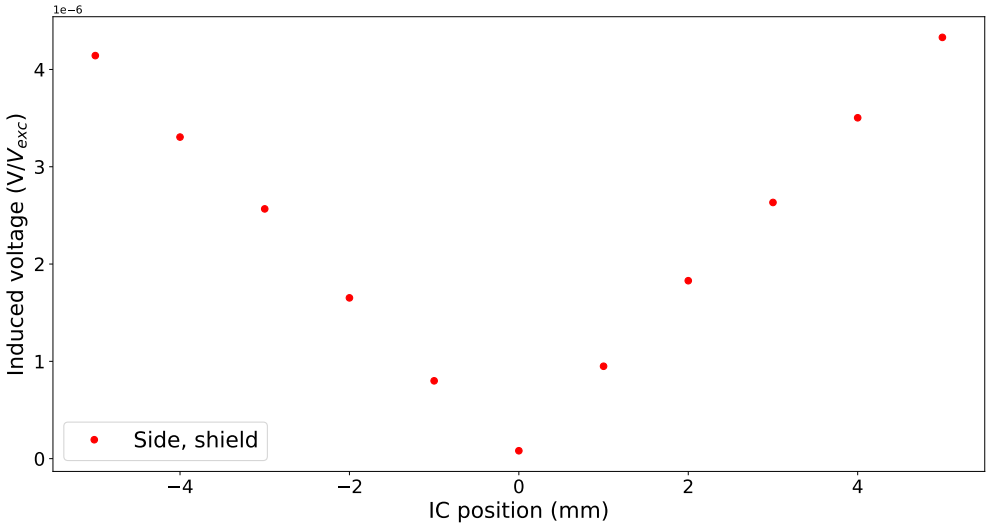


Figure 3.36: Induced voltage in the inner coil of the (not excited) main RLVDT when a side RLVDT has excited outer coils, with the presence of a shield. The center-to-center distance is 150 mm. The signal is normalized to excitation voltage [21].

As expected, since the RLVDT's are parallel, the response curve still has the same shape, the signal is just much smaller ($\approx 95\%$ smaller). We do see that the presence of copper shields reduce this signal even further with a factor $\approx 750$. Is this signal visible when we excite the outer coils of the main RLVDT? Figure 3.37 shows the induced voltage in the inner coil in four situations. The first situation is when only the main RLVDT is excited, this is the reference signal. The second situation has, again, only the main RLVDT excited but in this case there are shields present. As seen before, copper shields do influence the data, but, by how much, and is this influence greater than the influence a second RLVDT has? The third situation is the induced voltage when both the main and side RLVDT are excited, without shields. The fourth situation has both excited RLVDT's and where both RLVDT's have a shield. Figure 3.38 shows on the left the difference between the reference (only main RLVDT excited, without shield) and the other situations and on the right it shows the deviation percentage:

$$\text{deviation}(\%) = 100\% \cdot \frac{|\text{reference} - \text{situation}|}{\text{reference}}. \tag{3.10}$$

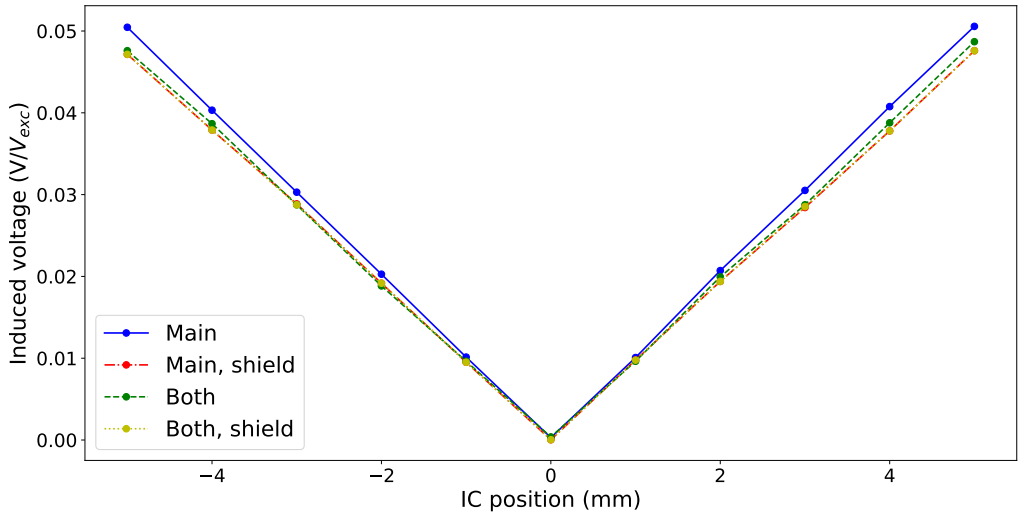


Figure 3.37: Induced voltage in the inner coil of the main RLVDT in the four situations. The center-to-center distance is 150 mm. The signal is normalized to excitation voltage.[21]

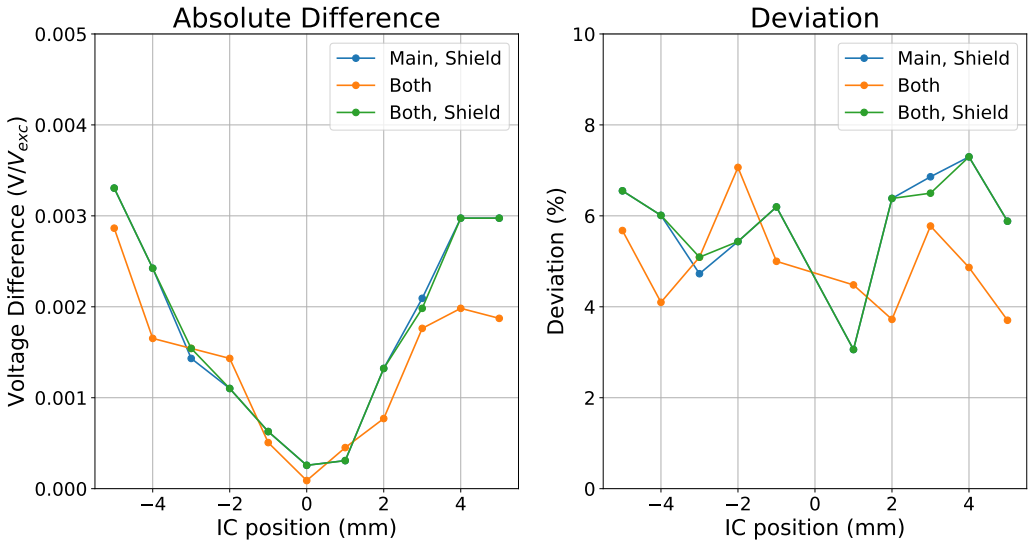


Figure 3.38: Left: Difference between reference and situation
Right: Deviation percentage of situation to reference [21]

When we compare the voltage induced by the excitation of the outer coils of the main RLVDT to the voltage induced by the excitation of the outer coils of the side RLVDT (Figure 3.35) we see that there is a difference of a factor $\approx 21$ when there are no shields.
Figure 3.37 and Figure 3.38 show that the excitation of the side RLVDT does influence the response of the main RLVDT (both). Implementing a shield gives protection from this second RLVDT, with only minimal differences between the 'Main, shield' and 'Both, shield' responses (max. 0.25%). However, the shields themselves have a bigger impact on the response than an unshielded, second RLVDT has (up to $> 2\%$), this is concluded by comparing 'Main, shield' and 'Both'. It can be seen that the orange curve is (in general) below the blue curve. The deviation is oscillating around an average deviation of 5%. The reason that the response curve of 'Both' is lower than 'Main' is because of the fact that the side

RLVDT is the exact same one as the main RLVDT, as a result, when the outer coil of the main RLVDT is coming outside of the screen, the outer coil of the side RLVDT is going in, therefore they have an opposing effect. Since the effect of the side RLVDT without shield is $\approx 5\%$ (see Figure 3.35), which is larger than the uncertainty on the measurement of the RLVDT slope ($\sim 1\%$), we can conclude that the influence for RLVDT's separated by 150 mm could be visible. The effect of the shielding can be calibrated, this would be harder for the effect of another RLVDT.

### Rotated RLVDT's

In this paragraph, we look at the voltage induced in the inner coil of the main RLVDT, where the outer coils are not excited, by the excited outer coils of a side RLVDT, which is rotated over 0°, 30°, 45°, 60° and 90° and where the center-to-center distance is 170 mm. This experiment is repeated for RLVDT's with a vertical position difference of 100 mm, and thus a center-to-center distance of 197.23 mm. Figure 3.39(a) and (b) shows the FEMM configuration of these two cases with the flux density and field lines. Figure 3.40 shows the induced voltages.

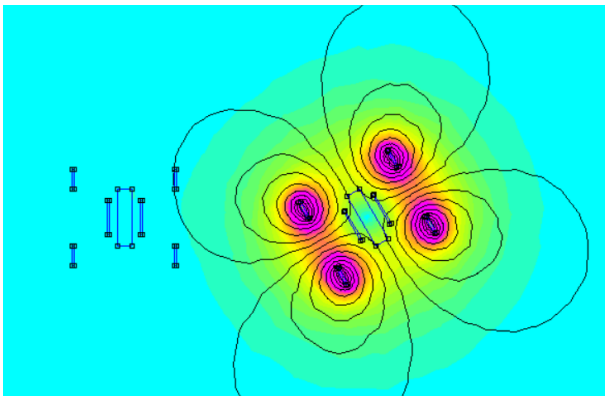

((a)) Flux density and field lines for an RLVDT rotated over 30°. Both RLVDT's have the same vertical position. The center-to-center distance is 170 mm [19].

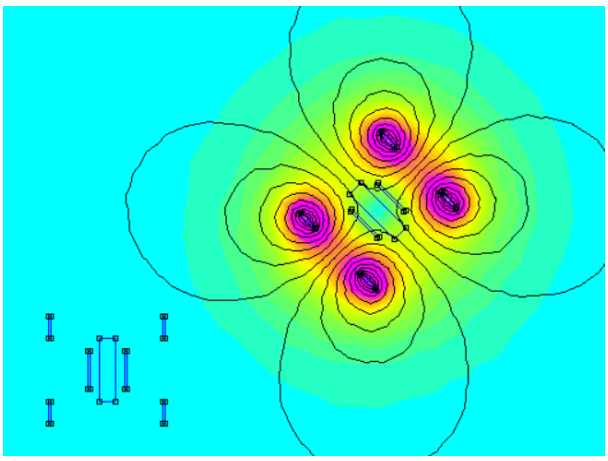

((b)) Flux density and field lines for an RLVDT rotated over 45°. RLVDT's have a different vertical position (100 mm). The center-to-center distance is 197.23 mm [19]

Figure 3.39: Configuration of the rotated RLVDT's

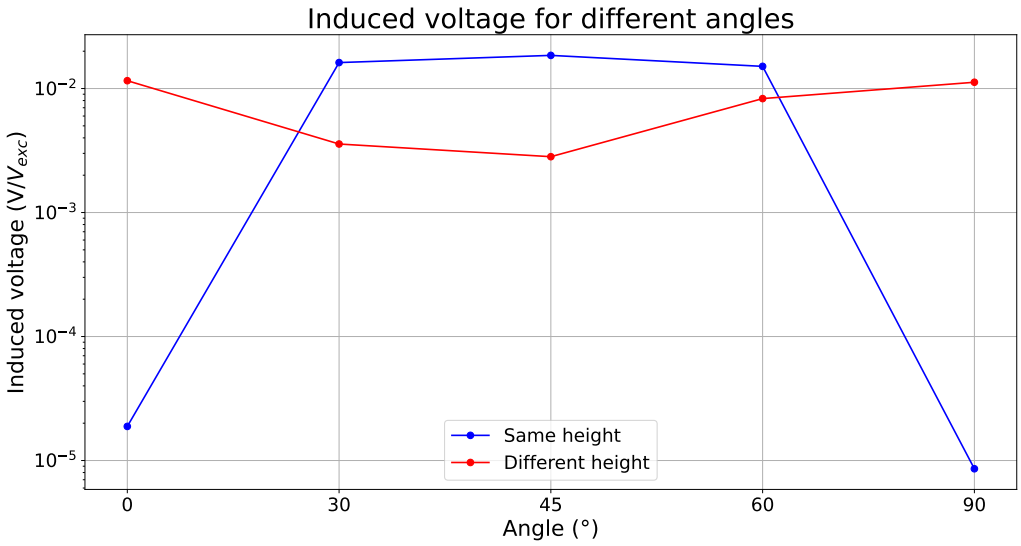


Figure 3.40: Voltage induced in the inner coil as a result of excited outer coils of a second RLVDT for different angles [21]

The extremely low voltages at 0° and 90° for the RLVDT's on the same height is due to symmetry. The inner coil of the main RLVDT is exactly in between the outer coils of the other RLVDT. This response got amplified by the gain-factor, making it seem higher than it actually is. Studying the field lines learns that the B-field is the weakest exactly in the middle, rotating the RLVDT means that this specific symmetry falls away. When the RLVDT's are on a different vertical position, this symmetry also falls away, but there is a new symmetry axis. In this specific configuration the new symmetry axis is around 45°, since this angle gives the minimum value. The overall lower induced voltage for the different height case is due to the fact that the distance between both RLVDT's is larger (197 mm compared to 170 mm). The conclusion that can be drawn is that a rotated RLVDT has a different impact, and that the minimal induction is on the symmetry axes of the RLVDT. However, this changes when the inner coil is not exactly at the center. This plot indicates that nearby RLVDT's, can really give a wrong idea. When the inner coil of one RLVDT is exactly in the middle, we expect 0 V, indicating that the mirror (or other components) are exactly in the right place. However, when a second RLVDT gets added, which is not parallel, at a distance of 197 mm, the inner coil registers 3 mV (for the 45° angle). This gives the idea that the inner coil of the main RLVDT, that is perfectly in the middle, has moved over 0.3 mm = 300 $\mu$m. This is an indication how important shielding will be.

# 4 Experimental Measurements

> **"The establishment of a law, moreover, does not take place when the first thought of it takes form, or even when its significance is recognized, but only when it has been confirmed by the results of the experiment."**
> ***Dmitri Mendeleev***

After simulating and theoretical research, it is necessary to verify the results of previous paragraph experimentally. We look at the influence one RLVDT has on another. This research exists out of two major parts, same frequency excitation and different frequency excitation (this is not possible in FEMM). In the first case we look how much influence the excited outer coils of an external RLVDT have on the inner coil of the main RLVDT. This will be done for two parallel RLVDT's, a height difference and an angle difference. For the two parallel RLVDT's the influence of adding an aluminum sheet of 4 mm thickness in between them will be studied to see if there is a similar shielding effect as we saw before. All data has a gain factor of $g = 69$.

## 4.1 Same Frequency Excitation

The induced voltage in the inner coil was measured for six different situations:

- 'Main': Only the outer coils of the main RLVDT are excited.
- 'Main, shield': Only the outer coils of the main RLVDT are excited, aluminum sheet is present.
- 'Side': Only the outer coils of the side RLVDT are excited.
- 'Side, shield': Only the outer coils of the side RLVDT are excited, aluminum sheet is present.
- 'Both': Outer coils of both main and side RLVDT are excited.
- 'Both, shield': Outer coils of both main and side RLVDT are excited, aluminum sheet is present

The center-to-center distance is 210 $\pm$10 mm and they are parallel ($\pm$1 mm).
The response is shown in Figure 4.1.

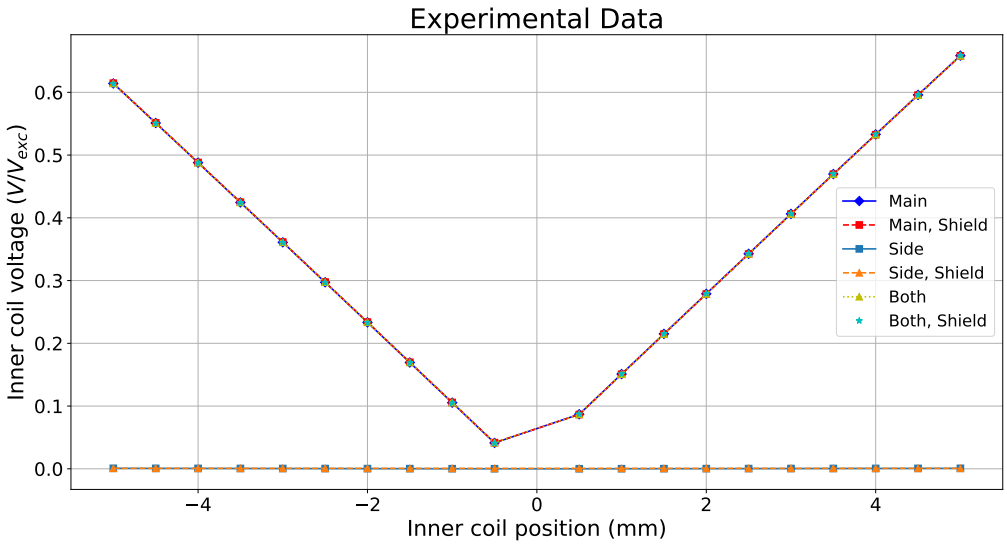


Figure 4.1: Voltage induced in the inner coil for the six described situations. [21]

The one thing we can learn from this figure is that the response from the side RLVDT, in both the shielded and unshielded case is many times smaller than the other responses. But more detailed figures are necessary to get a grasp on what is happening here. Figure 4.2 shows the response curve for the side RLVDT alone.

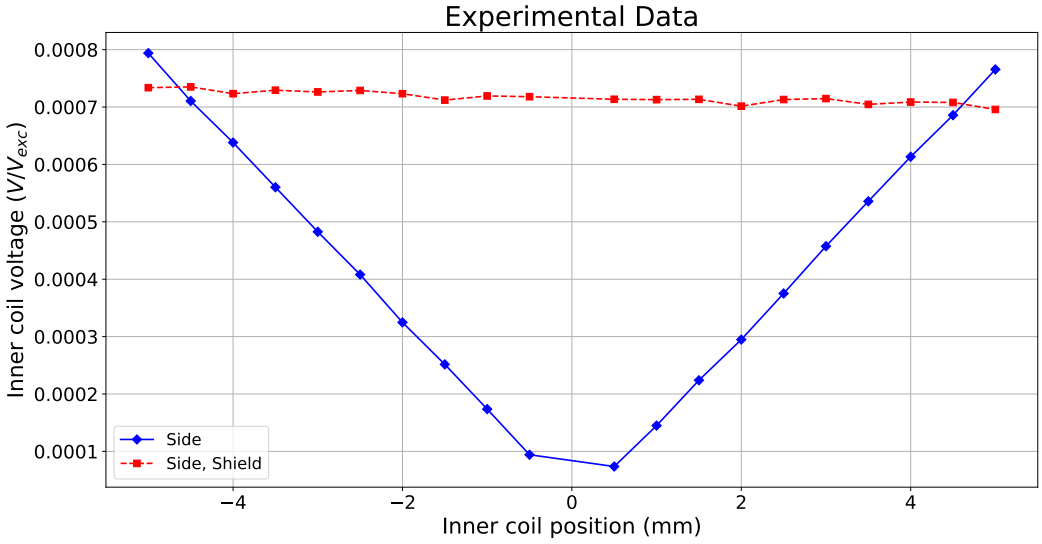


Figure 4.2: Voltage induced in the inner coil as a result of the excitation of the outer coils of the side RLVDT, main RLVDT is not excited [21].

Like in the simulations, we see that there is significant shielding effect. The induced voltage due to the side RLVDT is more than a factor $\approx 800$ times smaller than the response of the main RLVDT, but it is measurable! The presence of the shield does not reduce the signal but keeps it at an approximately steady value, this can be compensated by simple subtraction of a constant value.
Figure 4.3 shows the difference and deviation (Equation 3.10) of the situations 'Main, shield', 'Both' and 'Both, shield' with respect to 'Main'.

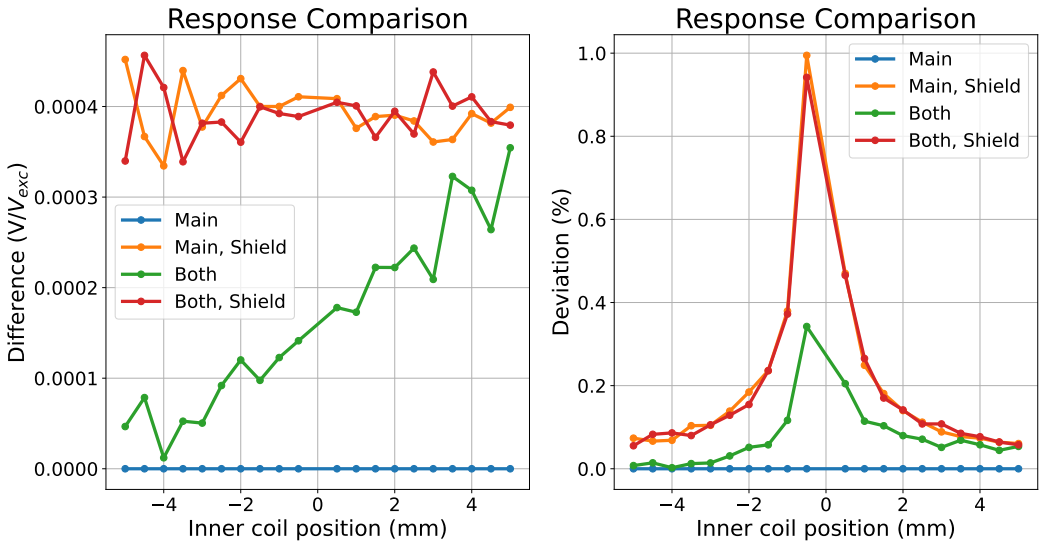


Figure 4.3: Left: Absolute Difference with respect to 'Main'
Right: Deviation with respect to 'Main' [21]

Like in the simulations, having a shield has more impact on the data than having an unshielded excited second RLVDT. In this real experiment, it is even more clear than it was from the simulations. We also see that having a shield gives a constant charge of $\sim 1$ mV. This is up to 1% relative change between $\pm 1$ mm. Looking at the green curve ('Both') we see that the effect of the side RLVDT at distance 210 $\pm 10$ mm on the main RLVDT within $\pm 1$ mm. Another big difference between the real experiment and the simulations is that in the simulations the 'Main, shield' and 'Both, shield' curves were overlapping, while the real experiment gives more distinct curves. One explanation could be noise, perhaps if this experiment would be repeated a large number of times, there would be a better overlap since the magnitude is similar. The peak in the deviation curves means that there is a bigger relative contribution for small values.
The side RLVDT was put into the angle holder of 50° (Figure 2.12), both for a vertical position equal to the main RLVDT, but also for a vertical position that was 12 cm lower. Figure 4.4 shows the response curve from the rotated RLVDT at both positions, and the response curve from the parallel side RLVDT with and without shield to have an estimate how the rotated RLVDT's compare to the parallel RLVDT. Figure 4.5 shows the same curves but without 'Side, Angle' to increase visibility of the other curves.

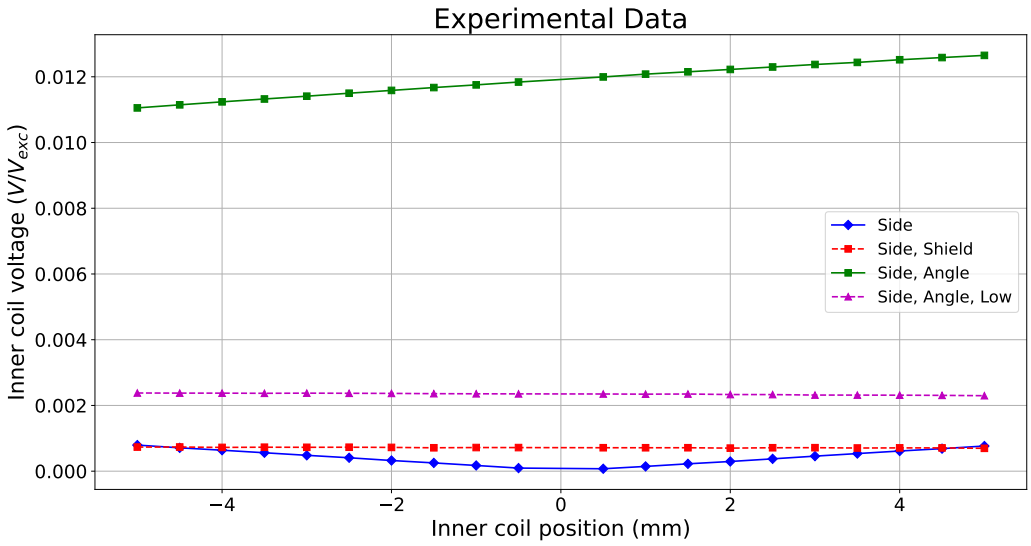


Figure 4.4: Induced voltage in the inner coil as a consequence of excited outer coils of a parallel side RLVDT ('Side'), a shielded parallel RLVDT ('Side, Shield'), a rotated RLVDT ('Side, Angle') and a rotated RLVDT on a lower suspension ('Side, Angle, Low') [21]

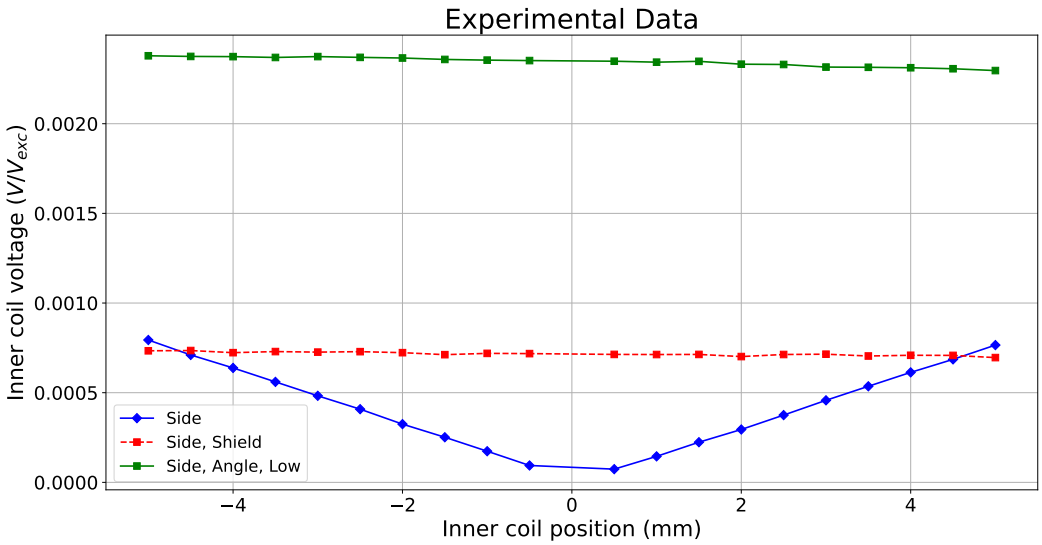


Figure 4.5: Induced voltage in the inner coil as a consequence of excited outer coils of a parallel side RLVDT ('Side'), a shielded parallel RLVDT ('Side, Shield') and a rotated RLVDT on a lower suspension ('Side, Angle, Low') [21]

The curve 'Side, Angle' is 15 times higher than the curve for the parallel situation ('side'). This was also seen in the simulations and can be understood by the same explanation as before; the pick-up coil is not on the symmetry axis of the rotated RLVDT anymore. The V-shape is gone, implying that the inner coil of the main RLVDT was not centered between the two outer coils of the side RLVDT, which makes sense for a 50° rotated RLVDT. The curve 'Side, Angle, Low' is $\approx 4$ times lower than the 'Side, Angle' curve for the sole reason that the distance between the RLVDT's was larger. The absence of V-shape can be explained the same way as before. This experiment verifies the claim made in the simulation angle study. The presence of a nearby rotated RLVDT will give a wrong idea about the position of the inner

coil of the main RLVDT. The curve 'Side, Angle' shows that there is an average measured voltage of 12 mV for an inner coil exactly in the middle. This will give the false indication that the inner coil moved over 100 $\mu$m.

## 4.2 Different Frequency Excitation

This paragraph will study the influence of an RLVDT that has an excitation frequency different than 10 kHz. The electronics are equipped with a frequency band filter around the 10 kHz that suppresses any signals that differ from it. This filter has a bandwidth so we had to choose the frequencies not too far from the 10 kHz. The chosen frequencies are 9500 Hz, 9700 Hz, 9900 Hz, 10100 Hz, 10300 Hz and 10500 Hz.
When working with the same frequency of 10 kHz, one can do a curve-fit of a sine function with a frequency of 10 kHz, via this curve-fit, the amplitude can be found. We have already seen that the response from a side RLVDT is quite small, $\approx$ 800 times smaller than the response of the main RLVDT. Because of this, the signal registered by the inner coil of the main RLVDT will be strongly dominated by the 10 kHz, making it impossible to do a curvefit of a different frequency on the signal. This requires doing a Fast Fourier Transform (FFT). FFT-analysis is a powerful tool that transforms the signal into frequency space, allowing us to see out of what frequencies the signal is made, and how big the weight of each frequency is. Using this, we can read out the amplitude of the picked up signal. Figure 4.6, 4.7 and 4.8 show the Fourier spectrum of the detected signal when the main RLVDT is excited with 10 000 Hz and the side RLVDT with 9 500 Hz with respectively a logarithmic, a linear x-axis and a zoomed version of the linear x-axis. The logarithmic x-axis is used to get a good overview of the different components of the signal (mainly used to study noise), while the linear x-axis makes it easier to identify which frequency belongs to the peaks.

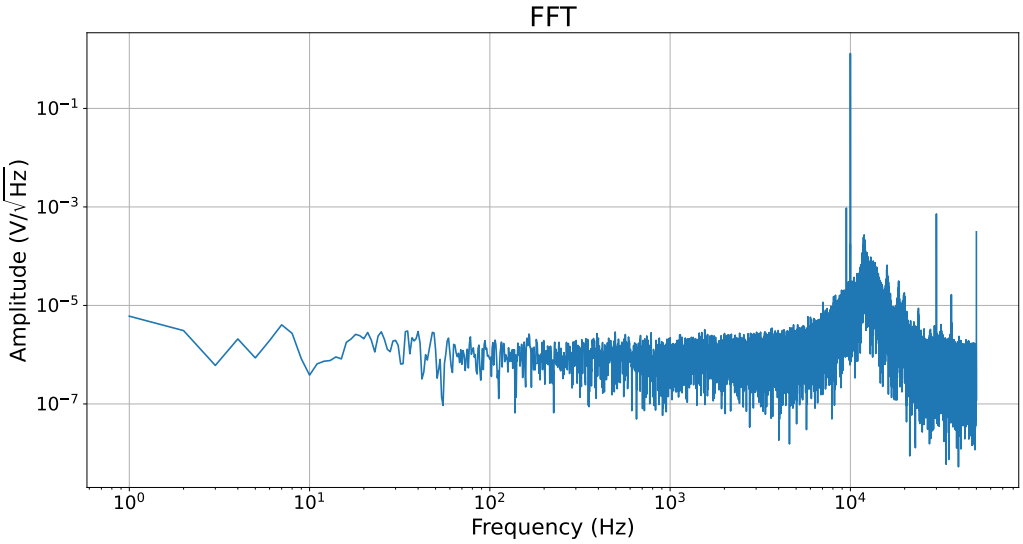


Figure 4.6: Fourier spectrum of the signal when the main RLVDT is excited with 10 kHz and the side RLVDT with 9500 Hz. Inner coil is at +5 mm. (Logarithmic x-axis) [21]

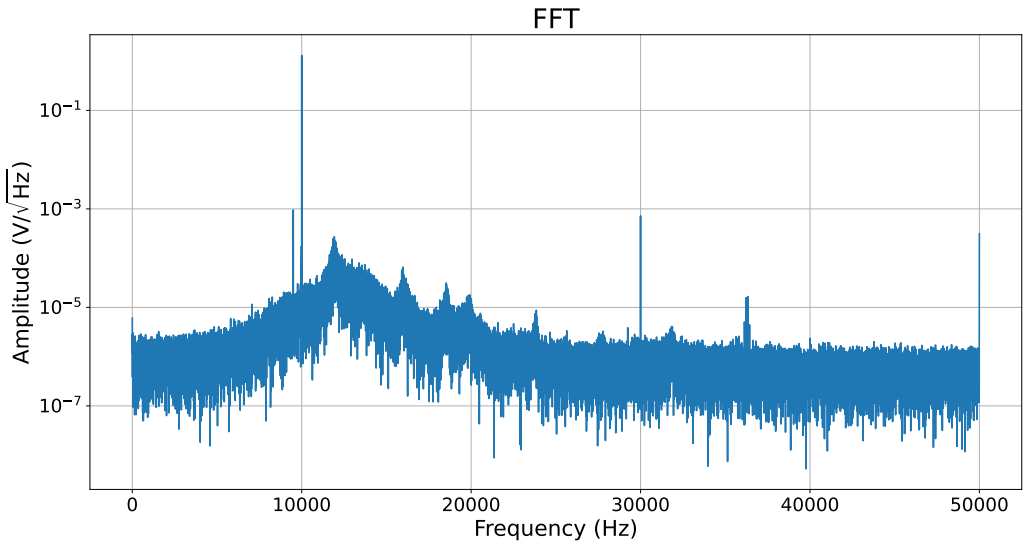


Figure 4.7: Fourier spectrum of the signal when the main RLVDT is excited with 10 kHz and the side RLVDT with 9500 Hz. Inner coil is at +5 mm. (Linear x-axis) [21]

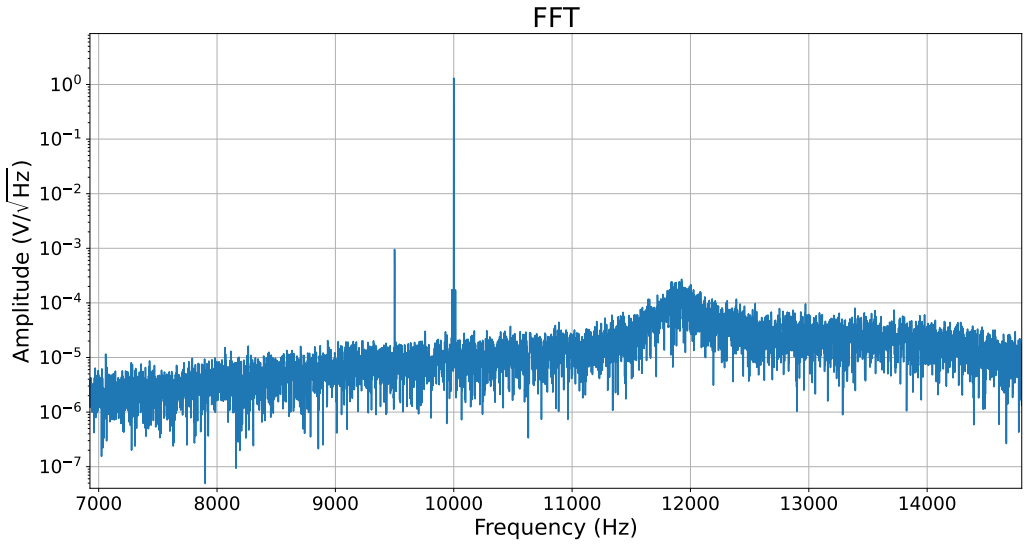


Figure 4.8: Fourier spectrum of the signal when the main RLVDT is excited with 10 kHz and the side RLVDT with 9500 Hz. Inner coil is at +5 mm. (Linear x-axis, zoom) [21]

The high peak is clearly the 10 kHz signal, the smaller peak close to the left of this peak is the 9500 Hz component. The height of these peaks give the amplitude, which is what is plotted in the response curves (induced voltage). The bandwidth of the frequency filter is clearly visible, suppressing all other frequencies. Figure 4.9 shows the amplitudes acquired by the FFT-analysis for the different frequencies.

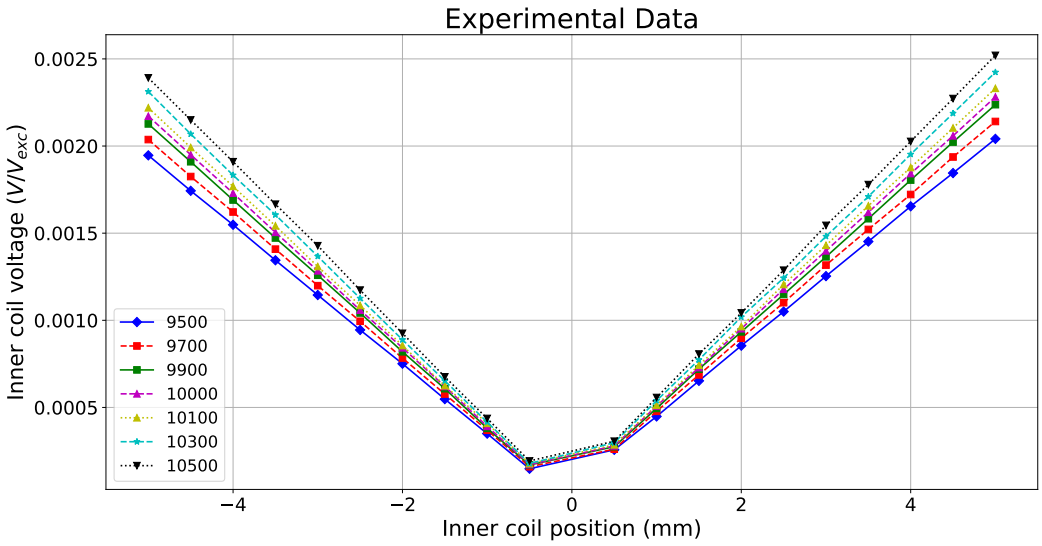


Figure 4.9: Response curves of the different frequencies of the side RLVDT, datapoints acquired by FFT-analysis [21]

This figure validates the simulated results from section 3.1.1, where we concluded that a higher excitation frequency induces more voltage. The question is if these signals have an impact on the 10 kHz peak. Figure 4.10 Shows the response curve for the different frequencies where the FFT amplitude at 10 kHz is taken,.Figure 4.11 shows the absolute difference on the left and the deviation percentage (Equation 3.10) on the right.

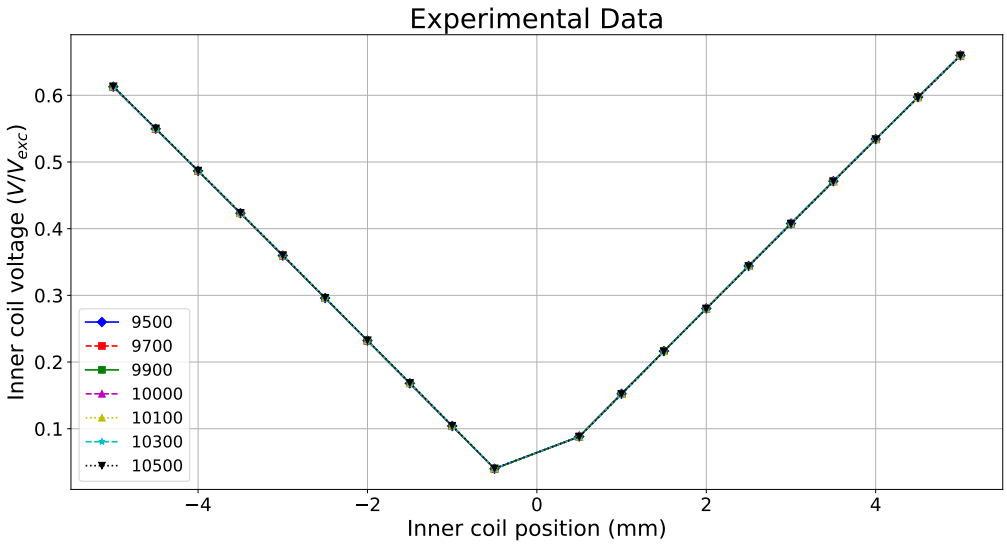


Figure 4.10: Response curves of amplitudes taken at 10 kHz [21]

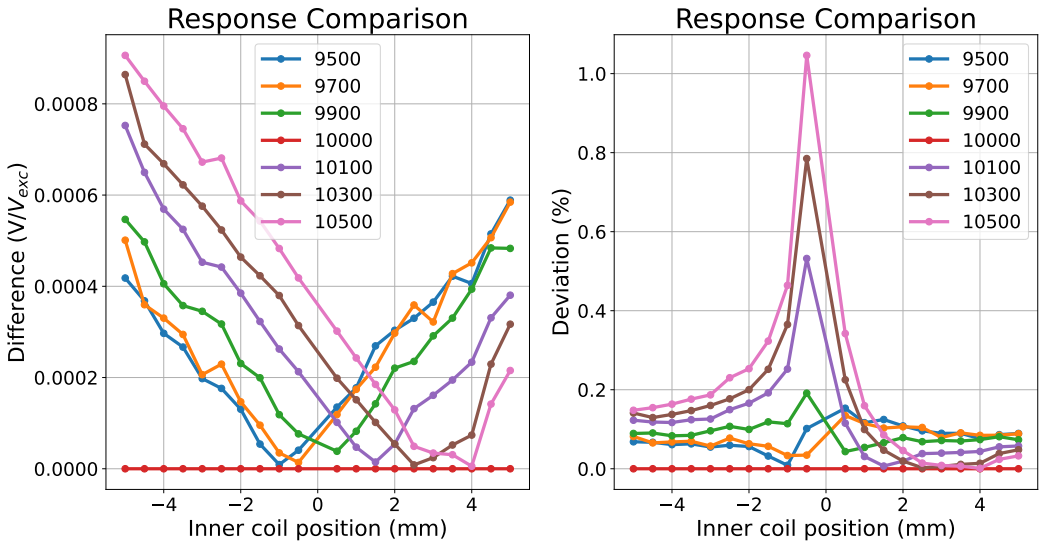


Figure 4.11: Left: Absolute difference with respect to when only the main RLVDT is excited at 10 kHz Right: Deviation percentage with respect to when only the main RLVDT is excited at 10 kHz [21]

The curves on Figure 4.10 all overlap, indicating that the impact is not too big, as expected from a 10 kHz FFT analysis. To quantify the impact Figure 4.11 gives a better idea. The maximal difference measured over a range of 10 mm is $\sim 0.00021\ V/V_{exc}$, this is a factor $\approx 700$ lower than the signal of the main RLVDT. The peak on the deviation plot is again an indication that the relative contribution is bigger for small values. The main idea of this research was to see if the RLVDT interference could be solved by exciting neighboring RLVDT's with another frequency. When this influence is compared to the case where the side RLVDT is also excited at 10 kHz, it is seen that the deviation and difference is of the same order.
However, the research was done within the bandpass filter, so we should see an effect. A better method would have been to integrate the signals in the bandpass to see the effect of the different frequencies more accurately, or to directly look at the demodulated signal. Following research could also experiment with frequencies outside of the bandpass filter.

# 5 Conclusion

> **"I am turned into a sort of machine for observing facts and grinding out conclusions."**
> ***Charles Darwin***

The field of gravitational wave detection has entered a new era of precision science, with future observatories like the Einstein Telescope aiming to explore the early universe and detect low frequency gravitational waves. Achieving these goals requires a careful approach to system sensitivity and noise reduction. This thesis has focused on one small but crucial component of these detection systems: the RLVDT, a sensor used to monitor the precise position of mirrors and other critical optical components. By studying RLVDT shielding and the background sensitivity and understanding the trade-offs between sensitivity, linearity, and electromagnetic field suppression, this work contributes to the broader effort of improving next-generation gravitational wave detectors.

The study was structured around two core methodologies: numerical simulations using the FEMM software and experimental validation. Through these complementary approaches, a variety of material and geometric configurations were tested and evaluated.

In high-frequency AC environments, as encountered in RLVDT operation ($\approx$ 10 kHz), traditional ferromagnetic shielding materials like iron and mu-metal show less effectiveness. This is primarily due to the collapse of magnetic permeability at higher frequencies. The frequency-dependent susceptibility and damping effects cause materials like mu-metal, which perform well at DC or low frequencies, to lose their shielding efficiency. Contrarily, highly conductive non-ferromagnetic materials like copper and aluminum perform surprisingly well at these frequencies due to their ability to support strong eddy currents. These induced currents generate opposing magnetic fields that cancel out the unwanted field.

The results from FEMM simulations confirm this: copper and aluminum provide significantly better suppression of high-frequency magnetic fields, while for DC magnetic field suppression, permeability dominates. Here, mu-metal and iron outperform copper and aluminum by redirecting field lines through the material. The duality of these findings implies that no single material is universally optimal.

This research was performed to examine the potential use of the RLVDT. While RLVDT's offer electronic advantages such as simplifying the actuation and readout electronics, they are more sensitive to noise due to the lack of differential signal cancellation and need to be shielded. Moreover, the shielding design must ensure that the internal magnetic fields remain undisturbed, keeping the linear response and sensitivity of the sensor, since they form the performance backbone of RLVDT-based position sensing. Introducing shields, while beneficial for reducing interference, risks altering the magnetic flux around the inner coil, changing the linearity or reducing the sensitivity of the sensor. This was confirmed in the response curve analyses, where sensitivity dropped when non-ferromagnetic shielding was used. For example, aluminum and copper shields reduced sensitivity up to a factor of 2.5 in some configurations, although linearity remained within acceptable limits. Iron and mu-metal improved the sensitivity but the linearity was lost. Stainless steel slightly improved linearity and increased the sensitivity but did not perform as well in the shielding study. This lead to the idea of using multilayered shields, to ensure shielding efficiency over a wide spectrum of frequencies but also maintaining, or even improving, the sensitivity and linearity.

Beyond material study, the thesis also explored the geometrical effects of shielding and the presence of apertures or holes required for mechanical suspension. Simulations showed that holes introduce measurable leakage, compromising shielding effectiveness.

Using simulations we discovered that increasing the radial and longitudinal distance of the non-ferromagnetic shields relative to the coil can restore the sensitivity and linearity.
Experimental measurements verified the results from the simulations. There is a measurable inductance from a neighboring RLVDT. This influence can be suppressed by an aluminum plate, but this brings forth other signal corruptions. We hypothesize that these shielding influences can be taken care of by calibration. Rotating the RLVDT's with respect to each other will also influence the data, but in a different way than a parallel set-up.
When two neighboring RLVDT's are excited at different frequencies, an FFT-analysis had to be performed. We could see here that higher excitation frequencies induce more voltage.
Finally, we explored the mechanical response of the RLVDT under high-frequency excitation. A theoretical approach of the oscillation amplitude showed that at typical excitation frequencies (10 kHz) and mirror masses ($\sim$1 kg or more), induced oscillations are of the order of picometers, well below the detection thresholds and within error tolerances of the system. This supports the usage of RLVDT's in environments like ETpathfinder, when optimized shielding is implemented.
Taken together, the findings of this thesis offer insights for the design and usage of RLVDT's in gravitational wave detectors. Shielding must be designed not only to suppress external noise but also to preserve the intrinsic response of the sensor. The results can be used when designing compact suspensions (HRTS) with RLVDT sensors very close to each other.
Future work could extend these findings by developing hybrid shield systems combining layers of ferromagnetic and conductive materials to achieve broad-spectrum shielding.

# Bibliography


[1] *(PDF) Analytical and Numerical Analysis of Magnetic Propulsion Force of a Cylindrical Micro-robot Considering the Characteristics of Magnetic Material*. URL: https://www.researchgate.net/publication/229010899_Analytical_and_Numerical_Analysis_of_Magnetic_Propulsion_Force_of_a_Cylindrical_Micro-robot_Considering_the_Characteristics_of_Magnetic_Material.

[2] *(PDF) ETpathfinder: a cryogenic testbed for interferometric gravitational-wave detectors*. URL: https://www.researchgate.net/publication/363321204_ETpathfinder_a_cryogenic_testbed_for_interferometric_gravitational-wave_detectors/figures?lo=1&utm_source=google&utm_medium=organic.

[3] *(PDF) The gravitational wave detector VIRGO*. URL: https://www.researchgate.net/publication/29596374_The_gravitational_wave_detector_VIRGO.

[4] B. P. Abbott, R. Abbott, et al. "Observation of Gravitational Waves from a Binary Black Hole Merger." In: *Physical Review Letters* 116.6 (Feb. 11, 2016). DOI: 10.1103/physrevlett.116.061102. URL: https://doi.org/10.1103/physrevlett.116.061102.

[5] Kumar Akhil. *Reverse LVDT*. Aug. 29, 2024.

[6] Mireia Alenyà Sistané. *Permeability characterization of ferrites in the radio frequency range*. June 2016. URL: https://diposit.ub.edu/dspace/bitstream/2445/102746/1/TFG_FIS_Alenya_Sistane_Mireia.pdf.

[7] Emanuele Berti. *The First Sounds of Merging Black Holes*. Feb. 11, 2016. URL: https://physics.aps.org/articles/v9/17.

[8] Nigel T. Bishop and Luciano Rezzolla. "Extraction of gravitational waves in numerical relativity." In: *Deleted Journal* 19.1 (Oct. 4, 2016). DOI: 10.1007/s41114-016-0001-9. URL: https://doi.org/10.1007/s41114-016-0001-9.

[9] Yann Bouffanais. "Bayesian inference for compact binary sources of gravitational waves." English. NNT: 2017USPCC197. Ph.D. Thesis. Université Sorbonne Paris Cité, 2017.

[10] Sean M. Carroll. *Spacetime and Geometry: An Introduction to General Relativity*. Jan. 1, 2003. URL: http://www.gbv.de/dms/goettingen/359467237.pdf.

[11] Emily Conover. "Naked singularity might evade cosmic censor." In: (Aug. 8, 2019). URL: https://www.sciencenews.org/article/naked-singularity-might-evade-cosmic-censor.

[12] Wikipedia contributors. *Mu-metal*. Apr. 2025. URL: https://en.wikipedia.org/wiki/Mu-metal.

[13] ET Science Team. *Einstein gravitational wave Telescope. Conceptual Design Study*. ET-0106C-10. June 28, 2011. (Visited on 05/01/2025).

[14] ET Steering Committee Editorial Team and ET Editorial Team. *Design Report Update 2020 for the Einstein Telescope*. 2020.

[15] ETpathfinder Team. *ETPathfinder Design Report*. Jan. 24, 2020. URL: https://www.etpathfinder.eu/wp-content/uploads/2020/03/ETpathfinder-Design-Report.pdf.

[16] Tobin Fricke and Max-Planck-Institut für Gravitationphysik. *The AEI 10m Prototype Facility*. Aug. 25, 2014. URL: https://dcc.ligo.org/public/0115/G1400991/001/10mLSC2014.pdf.

[17] *Gallery – ETPathfinder*. URL: https://www.etpathfinder.eu/gallery/.

[18] *How LVDTs Work — The LVDT Operating Principle*. Mar. 23, 2021. URL: https://lvdt.co.uk/lvdt-info/how-lvdts-work/.

[19] Jonas Jacobs. "FEMM image." Image created by the author. 2025.

[20] Jonas Jacobs. "Picture." Image created by the author. 2025.

[21] Jonas Jacobs. "Python figure (matplotlib)." Image created by the author. 2025.

[22] Jonas Jacobs. "Schematic representation." Image created by the author. 2025.

[23] Lodovico. *Michelson 8211; Morley Interferometer*. May 24, 2020. URL: https://physicsopenlab.org/2020/05/16/michelson-morley-interferometer/.

[24] Yuta Michimura. *KIW5 and KAGRA-Virgo-3G Workshop Report*. Feb. 22, 2018. URL: https://granite.phys.s.u-tokyo.ac.jp/michimura/presentation/labseminar_LIMMA2019KIW5.pdf.

[25] T. Nakamura, T. Tsutaoka, and K. Hatakeyama. "Frequency dispersion of permeability in ferrite composite materials." In: *Journal of Magnetism and Magnetic Materials* 138.3 (Dec. 1, 1994), pp. 319–328. DOI: 10.1016/0304-8853(94)90054-x. URL: https://www.sciencedirect.com/science/article/pii/030488539490054X?via%3Dihub.

[26] NIKHEF. "Preliminary NIKHEF design dimensions." Internal Document. 2022.

[27] Ümit Özgür, Yahya Alivov, and Hadis Morkoç. "Microwave ferrites, part 1: fundamental properties." In: *Journal of Materials Science Materials in Electronics* 20.9 (June 24, 2009), pp. 789–834. DOI: 10.1007/s10854-009-9923-2. URL: https://link.springer.com/article/10.1007/s10854-009-9923-2.

[28] Physics Ninja. *Magnetic Field from a Helmholtz Coil*. Apr. 13, 2020. URL: https://www.youtube.com/watch?v=_6bKJrGCuJk.

[29] *pyFEMM – A Python Interface to FEMM:Finite Element Method Magnetics*. URL: https://www.femm.info/wiki/pyfemm.

[30] Elizabeth Quill. "Einstein's theory of general relativity unveiled a dynamic and bizarre cosmos." In: (Oct. 31, 2022). URL: https://www.sciencenews.org/article/einstein-theory-general-relativity-gravity-black-holes-cosmos.

[31] Fred Schimmel. *Optimization and extension of the VIRGO LVDT-design for ordinary and dedicated applications*. Tech. rep. Sept. 2020.

[32] *Snoek's limit in High-Frequency permeability of polycrystalline Ni–Zn, Mg–Zn, and Ni–Zn–Cu spinel ferrites*. https://www.researchgate.net/publication/234885252_Snoek's_Limit_in_High-Frequency_Permeability_of_Polycrystalline_Ni-Zn_Mg-Zn_and_Ni-Zn-Cu_Spinel_Ferrites. Accessed via ResearchGate. n.d.

[33] *Spacetime curvature*. URL: https://www.esa.int/ESA_Multimedia/Images/2015/09/Spacetime_curvature.

[34] Enzo Tapia. *KAGRA Lecture 2 for students 09.08.2018*. 2018. URL: https://gwdoc.icrr.u-tokyo.ac.jp/DocDB/0086/G1808697/001/KAGRA_Lecture2_GAS_filter_and_LVDT.pdf.

[35] Hareem Tariq et al. “The linear variable differential transformer (LVDT) position sensor for gravitational wave interferometer low-frequency controls.” In: *Nuclear Instruments and Methods in Physics Research Section A Accelerators Spectrometers Detectors and Associated Equipment* 489.1-3 (Aug. 1, 2002), pp. 570–576. DOI: 10.1016/s0168-9002(02)00802-1. URL: https://doi.org/10.1016/s0168-9002(02)00802-1.

[36] Marco Tavora PhD. “Einstein’s gravity, the bending of light and how he became the world’s most famous scientist.” In: (Dec. 14, 2021). URL: https://medium.com/data-science/einsteins-gravity-theory-and-the-bending-of-light-by-the-sun-1e796626dc19.

[37] Alexandre Le Tiec and Jérôme Novak. *Theory of gravitational waves*. Feb. 17, 2017, pp. 1–41. DOI: 10.1142/9789813141766_0001. URL: https://arxiv.org/abs/1607.04202.

[38] Unknown. *CAD representation*. Accessed from private cloud storage; not publicly available. 2025.

[39] Unknown. *Picture*. Accessed from private cloud storage; not publicly available. 2025.

[40] Van Haevermaet. *ETpathfinder LVDT overview*. Internal Document. June 13, 2022.

[41] Van Haevermaet. *Zwaartekrachtsgolven deel 1*. Internal Document. Nov. 2023.

[42] Van Haevermaet. *Zwaartekrachtsgolven deel 2*. Internal Document. Nov. 2023.

[43] Verbeeck. *Algemene Fysica III: Elektromagnetisme*. Internal Document. Sept. 2022.

[44] *What are Eddy Currents?* Apr. 30, 2015. URL: https://www.magcraft.com/blog/what-are-eddy-currents.

[45] Wikipedia contributors. *Ampère’s circuital law*. May 2, 2025. URL: https://en.wikipedia.org/wiki/Amp%C3%A8re%27s_circuital_law.

[46] Wikipedia contributors. *Apsidal precession*. Mar. 29, 2025. URL: https://en.wikipedia.org/wiki/Apsidal_precession.

[47] Wikipedia contributors. *Cavendish experiment*. Apr. 29, 2025. URL: https://en.wikipedia.org/wiki/Cavendish_experiment.

[48] Wikipedia contributors. *Eddy current*. May 7, 2025. URL: https://en.wikipedia.org/wiki/Eddy_current.

[49] Wikipedia contributors. *Finite element method*. May 23, 2025. URL: https://en.wikipedia.org/wiki/Finite_element_method.

[50] Wikipedia contributors. *First observation of gravitational waves*. May 6, 2025. URL: https://en.wikipedia.org/wiki/First_observation_of_gravitational_waves.

[51] Wikipedia contributors. *Gravitational lens*. Apr. 28, 2025. URL: https://en.wikipedia.org/wiki/Gravitational_lens.

[52] Wikipedia contributors. *Gravitational wave*. Apr. 10, 2025. URL: https://en.wikipedia.org/wiki/Gravitational_wave.

[53] Wikipedia contributors. *Gravitational-wave observatory*. May 10, 2025. URL: https://en.wikipedia.org/wiki/Gravitational-wave_observatory#Laser_interferometers.

[54] Wikipedia contributors. *KAGRA*. Apr. 4, 2025. URL: https://en.wikipedia.org/wiki/KAGRA.

[55] Wikipedia contributors. *LIGO*. Apr. 10, 2025. URL: https://en.wikipedia.org/wiki/LIGO.

[56] Wikipedia contributors. *Linear variable differential transformer*. Jan. 12, 2025. URL: https://en.wikipedia.org/wiki/Linear_variable_differential_transformer.

[57] Wikipedia contributors. *Maxwell coil*. Sept. 22, 2024. URL: https://en.wikipedia.org/wiki/Maxwell_coil.

[58] Wikipedia contributors. *Newton's law of universal gravitation*. Apr. 23, 2025. URL: https://en.wikipedia.org/wiki/Newton%27s_law_of_universal_gravitation.

[59] Wikipedia contributors. *Skin effect*. Apr. 26, 2025. URL: https://en.wikipedia.org/wiki/Skin_effect.

[60] Wikipedia contributors. *Virgo interferometer*. May 22, 2025. URL: https://en.wikipedia.org/wiki/Virgo_interferometer.

[61] Wikipedia contributors. *Voice coil*. Nov. 20, 2024. URL: https://en.wikipedia.org/wiki/Voice_coil.

[62] Wolfram Research, Inc. *Einstein, Albert (1879-1955) – from Eric Weisstein's World of Scientific Biography*. URL: https://scienceworld.wolfram.com/biography/Einstein.html.

[63] *Zwaartekrachtsgolven - Einstein Telescope*. July 17, 2023. URL: https://www.einsteintelescope-emr.eu/zwaartekrachtsgolven-als-sterren-botsen-trilt-de-ruimte-na/.